*Solar RRL*

REVIEW OPEN ACCESS

# Bifacial Chalcogenide Thin-Film Solar Cells: Concepts, Challenges, and Opportunities

Amanat Ali[1,2] | Bashiru Kadiri-English[1,2] | Dae-Ho Son[1] | Jaebaek Lee[1] | Jin-Kyu Kang[1] | Dae-Kue Hwang[1] | Shi-Joon Sung[2] | Kee-Jeong Yang[1] | Dae-Hwan Kim[1,2]

[1]Division of Energy & Environmental Technology, Daegu–Gyeongbuk Institute of Science and Technology (DGIST), Daegu, Republic of Korea | [2]Department of Interdisciplinary Engineering, Daegu–Gyeongbuk Institute of Science and Technology (DGIST), Daegu, Republic of Korea

**Correspondence:** Kee-Jeong Yang (kjyang@dgist.ac.kr) | Dae-Hwan Kim (monolith@dgist.ac.kr)

**Received:** 31 August 2025 | **Revised:** 14 October 2025 | **Accepted:** 30 October 2025

**Keywords:** bandgap tuning | bifacial photovoltaics | chalcogenides | transparent back contact

## ABSTRACT

Bifacial solar cells effectively increase photovoltaic energy generation by harnessing light from both the front and rear surfaces. In the realm of thin-film technology, inorganic chalcogenides specifically (Cu (In, Ga)$Se_2$, S), CdTe, $Cu_2ZnSn$ (S, Se)$_4$, and $Sb_2$(S, Se)$_3$ exhibit significant potential owing to their adjustable band gaps, robust absorption characteristics, and scalable manufacturing processes. This review emphasizes current advancements in chalcogenide-based bifacial photovoltaics, concentrating on device principles, absorber appropriateness, and performance limitations. Numerical and experimental investigations demonstrate that bifacial illumination not only alleviates interfacial band bending under specific conditions but also produces power outputs that surpass the cumulative contributions of single-side illumination, while exhibiting resilience to diffuse rear illumination. Nevertheless, actual albedo levels indicate that reductions in front-side efficiency cannot be entirely compensated for rear-side improvements, highlighting the necessity for clear low-recombination contacts, efficient light management, and robust device interfaces. We end with an overview of strategies spanning back contact engineering to outdoor durability that are crucial for advancing bifacial chalcogenide photovoltaics from laboratory demonstrations to initial commercialization. Bifacial solar cell configurations are particularly advantageous for tandem applications. This offers a promising pathway to further enhance overall device efficiency.

## 1 | Introduction

The rising worldwide energy demand, along with the pressing need to decarbonize power generation, has placed renewable energy technologies at the forefront of the energy transition [1]. Solar photovoltaics (PVs) have become a fundamental technology, providing scalability, sustainability, and the direct conversion of sunlight into electricity with negligible environmental impact [2]. Their deployment is essential for satisfying the escalating energy requirements of contemporary society and is vital for attaining global climate objectives, such as generating net-zero greenhouse gas emissions by 2050 [3, 4]. As a clean, plentiful, and adaptable energy source, photovoltaics is crucial in diminishing reliance on fossil fuels and facilitating the shift toward a low-carbon global economy [5–7].

In recent decades, substantial progress has been made in single-junction solar cell technologies, notably crystalline silicon (Si), cadmium telluride (CdTe), and copper indium gallium selenide (CIGSe). These technologies prevail in the global photovoltaic market owing to their maturity, cost-efficiency, and elevated power conversion efficiencies (PCEs) [8–10]. Ongoing advancements in light management, passivation techniques, and manufacturing methods have elevated device performance. Nonetheless, despite their market success, these monofacial structures are limited by

Amanat Ali and Bashiru Kadiri-English contributed equally to this study.

the Shockley–Queisser efficiency threshold, which establishes a basic maximum of ≈33.7% for an absorber with an ideal bandgap of 1.34 eV. Exceeding this inherent limitation necessitates new methodologies and innovative device architectures that can harness a wider range of solar radiation [11].

Bifacial photovoltaic cells have emerged as an innovation capable of outperforming conventional monofacial layouts. Bifacial devices attain superior energy yields by capturing photons on both the front and rear surfaces, particularly in high albedo or diffuse scattering settings [12–14]. Their multifunctionality renders them exceptionally appropriate for building-integrated photovoltaics (BIPV), agrivoltaics, and advanced transparent or semitransparent photovoltaic applications in cars and infrastructure [15, 16]. Bifacial modules, in contrast to monofacial devices, provide enhanced land-use efficiency, more adaptability to real-world situations, and considerable promise for lowering the levelized cost of electricity (LCOE) [8, 17]. Bifacial silicon devices are currently available on the market, although bifacial thin-film technologies, such as chalcogenide-based photovoltaic devices, are progressing swiftly [18]. Bifacial modules are expected to account for over 73% of the worldwide photovoltaic market by 2034, signifying not just a minor enhancement but a transformative change aimed at surpassing the Shockley–Queisser limit and facilitating ultra-efficient, scalable solar energy systems [19, 20].

This review systematically examines the current advancements in chalcogenide solar cells, focusing on fabrication strategies, bandgap engineering, doping methods, interface passivation, and the development of transparent back contacts. These elements are essential for facilitating bifacial operation with improved power conversion efficiency and long-term stability. Attention is directed towards Cu (In, Ga) (S, $Se_2$) (CIGSe), CdTe, $Cu_2ZnSn$ (S, $Se)_4$ (CZTSSe), and antimony-based absorbers, emphasizing their inherent optoelectronic characteristics and the potential for modification via both extrinsic and intrinsic doping. The controlled incorporation of alkali metals (Na, K, Rb, Cs) is examined for its role in defect passivation and enhancement of grain growth. Additionally, strategies involving cation/anion substitution, such as Ga/In, S/Se alloying, and Cl/Br doping, are analyzed for their effectiveness in bandgap tuning, improving charge-carrier lifetimes, and mitigating harmful recombination pathways. We analyze recent advancements and ongoing challenges in attaining stable performance under dual-sided illumination, focusing on carrier transport limitations, back-interface recombination, and uneven rear-side irradiance. Doping-enabled bandgap grading, carrier-selective junctions, and defect suppression are identified as critical factors for enhancing bifacial performance. We present a forward-looking perspective on emerging opportunities, including advanced transparent conductive oxides, tandem integration, and novel doping strategies, which are anticipated to facilitate the transition of chalcogenide-based bifacial solar cells from laboratory prototypes to early commercialization.

## 2 | Results and Discussion

### 2.1 | CIGS Solar Cells

CIGS solar cells have emerged as a highly promising thin-film photovoltaic technology owing to their distinctive attributes of elevated efficiency, adjustable bandgap, and flexibility. CIGS devices, in contrast to traditional crystalline silicon solar cells, demonstrate a superior absorption coefficient and may be manufactured on both rigid glass and flexible substrates, including polyimide, metal foils, and ultrathin glass. CIGS solar cells on glass-based monofacial substrates have achieved record efficiencies above 23.6%, ranking them among the top-performing thin-film chalcogenide devices [21]. Simultaneously, flexible CIGS cells have attained efficiencies over 20%, far outpacing other flexible solar technologies such as organic photovoltaics or amorphous silicon, while maintaining mechanical durability and long-term stability [22]. These developments have been facilitated by technologies such as gallium grading, alkali post-deposition treatments, and interface engineering, which enhance the absorber layer and device architecture. The Shockley–Queisser limit theoretically establishes the maximum efficiency of a single-junction solar cell at around 33% [23]. CIGS possesses an adjustable direct bandgap range of 1.0–1.7 eV, strategically situated near the optimal bandgap (about 1.34 eV) to attain this threshold [11]. The amalgamation of high efficiencies, compatibility with both rigid and flexible platforms, elucidates why CIGS solar cells remain a pre-eminent technology for applications including building-integrated photovoltaics, rooftop installations, portable devices, aerospace, and next-generation flexible electronics [24].

Bifacial configurations of CIGS solar cells have recently garnered considerable attention due to their ability to capture sunlight from both the front and rear surfaces, thereby significantly improving photocurrent generation compared to traditional monofacial devices. By including transparent conductive oxide (TCOs) back contacts, such as indium tin oxide (ITO) [25] fluorine-doped Tin Oxide (FTO) [4], aluminum-doped zinc oxide (AZO) [26], or ultrathin metallic interlayers (Ag, $MoO_X$/ITO stacks) enable bifacial CIGS devices to mitigate the optical losses associated with opaque Mo back electrodes [27]. Figure 1a illustrates the CIGS device structure incorporating various TCO back contact materials, while Figure 1b presents the flexible device configuration employing different flexible substrates. This arrangement enables the cells to capture direct sunlight from the front and to harness diffuse and reflected light from the back, thus enhancing energy output in practical outdoor circumstances. Bifacial CIGS cells have exhibited efficiencies beyond 19%–20% on rigid glass substrates and over 15%–16% on flexible substrates, establishing them as the most efficient bifacial among chalcogenide thin-film technologies to date. Bifacial CIGS devices not only achieve superior power output but also retain the intrinsic benefits of the CIGS material system, such as bandgap tunability, defect tolerance, and exceptional performance under low-light or high-temperature conditions. Bifacial CIGS architectures present a viable strategy to achieving the Shockley–Queisser (SQ) limit of ≈33% for single-junction devices from a basic standpoint [11]. Given that CIGS has a configurable direct bandgap range around the ideal 1.34 eV, optimizing photon absorption from both sides is a rational approach to minimize thermalization and transmission losses that limit traditional monofacial designs [19]. Transparent or semitransparent back contacts provide enhanced photocurrent collection without markedly diminishing voltage, hence advancing the practical efficiency threshold nearer to the theoretical limit. This is especially appealing for applications in building-integrated photovoltaics (BIPV), agrivoltaics, and advanced transparent or semi-transparent modules for windows, roofs, and vehicle-integrated photovoltaics,

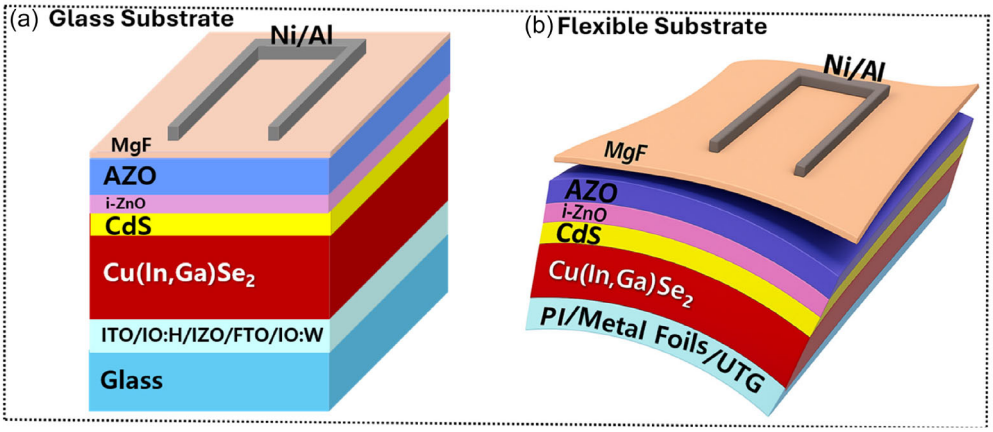


**FIGURE 1** | (a) Device schematic of a Bifacial CIGS solar cell with different TCO back contact. (b) Device schematic of a flexible Bifacial CIGS solar cell with different back contact.

where light can be received from various angles [28]. Bifacial CIGS enhances the performance capabilities of thin-film solar technology and broadens its applicability in diverse, high-value applications requiring both efficiency and aesthetics. From now on, CIGS will be classified into three categories according to Ga content and the corresponding bandgap. This categorization allows precise optimization of material properties, enabling their use in a wide range of applications, including BIPV, portable electronic devices, and high-efficiency tandem solar cells.

### 2.1.1 | CIGS Standard Bandgap

Standard-bandgap CIGS absorbers, possessing an optimal bandgap of ≈1.1–1.2 eV, constitute the most developed and effective configuration within the CIGS material family. Certified single-junction devices have attained record efficiencies surpassing 23.6%, ranking them among the most efficient among the inorganic thin-film solar technologies [21]. This bandgap range is advantageous as it aligns closely with the Shockley–Queisser limit for single-junction solar cells under AM1.5G light, facilitating an optimal balance between open-circuit voltage ($V_{OC}$) and short-circuit current density ($J_{SC}$). The direct bandgap, along with absorption coefficients above $10^5\,cm^{-1}$, facilitates the utilization of thin absorbers (≈1.5–2.5 μm) while preserving superior light-harvesting efficiency. This not only diminishes raw material usage but also enables the production of flexible and lightweight electronics on polymer or metal foils, hence expanding the application range beyond rigid glass modules.

In bifacial structures, standard-gap CIGS has demonstrated notable potential owing to its spectrum compatibility with light from both the front and back sides. When combined with transparent or semitransparent back contacts (e.g., ITO, $In_2O_3$: W, or ultrathin Mo/Ag layers), CIGS maintains its high absorption and stability, enabling rear-side photons, either reflected from ground albedo or transmitted through bifacial module designs to enhance photocurrent generation. This dual-sided harvesting feature increases the energy output per unit area, particularly in high-albedo settings like snow, desert sand, or reflecting rooftops. The ≈1.1–1.2 eV bandgap of CIGS renders it exceptionally appropriate as a bottom cell in bifacial tandem structures, especially when combined with wide-bandgap perovskites or chalcogenides, facilitating sophisticated 2- and 4-terminal arrangements. These characteristics establish standard-gap CIGS as the reference absorber for both monofacial and flexible devices, as well as for developing bifacial and tandem solar technologies.

**2.1.1.1 | Strategies for Enhancement Performance of Bifacial CIGS SCs.** Recent advancements in bifacial CIGS photovoltaics have been significantly influenced by the incorporation of TCO layers as back contacts. Yang et al. present a silver-assisted, low-temperature co-evaporation method that facilitates the direct deposition of CIGS absorbers onto ITO without the conventional development of a highly resistive $GaO_X$ interface layer [29]. This is accomplished by integrating around 4%–5% Ag throughout growth, together with regulated NaF and RbF post-deposition treatments. These alterations preserve the optical transparency and electrical conductivity of ITO while facilitating the development of micrometer-thick absorbers with pronounced Ga back-grading, crucial for efficient carrier collection. The group attained certified bifacial devices on glass substrates, exhibiting a front-side efficiency of 19.77% and a rear-side efficiency of 10.89% under standard 1-sun illumination, marking a substantial advancement over previous bifacial CIGS efforts that often-compromised rear performance for front-side efficiency [30]. Furthermore, when incorporated into a four-terminal tandem configuration with perovskites, the bifacial devices achieved power outputs of $28\,mW\,cm^{-2}$ under simultaneous front and albedo illumination, underscoring the significant potential of TCO-based bifacial CIGS in tandem architectures.

Suppression of $GaO_X$ and Interface Transport: The enhancement in device performance is principally due to the suppression of $GaO_X$ at the CIGS/ITO interface, which usually forms at elevated substrate temperatures and presents a reverse-junction-like barrier to hole transport. By employing optimal low-temperature growth at ≈353°C, the interface is maintained in a pristine condition, facilitating efficient hole extraction at the p-CIGS/$n^+$-ITO junction. Structural investigation utilizing STEM and EDS indicates no $GaO_X$ formation and shows that the absorbers retain substantial grain sizes with organized dislocation patterns, implying quasi-epitaxial development. This morphological enhancement diminishes non-radiative recombination routes and, in conjunction with a pronounced Ga back-gradient,

mitigates carrier losses in the rear area. The outcome is elevated fill factors and consistent open-circuit voltages, even with a TCO back electrode, which has traditionally presented considerable difficulties due to resistive losses [30].

Rear-Side Limitations and Optical Losses: Despite good front-side performance, parasitic optical and recombination losses limit bifacial CIGS devices' rear-side response. ITO transparency decreases as growth temperatures rise, reducing optical absorption. Carriers formed near the CIGS/ITO border tend to recombine at the rear interface before contributing to the photocurrent, which is a major constraint. Ga back-grading restricts minority carriers from the back surface, partially alleviating this issue. However, the optimization of the TCO is still crucial. The authors propose that alternative transparent conductive oxides, such as hydrogen-doped indium oxide (IO:H) or indium zinc oxide (IZO), may provide enhanced transparency while maintaining similar sheet resistances. Consequently, these materials are considered promising candidates for next-generation bifacial configurations, where rear-side spectral harvesting is essential [31].

Flexible Substrates and Industrial Relevance: The adaptation of bifacial CIGS technology to flexible substrates is crucial for lightweight, portable, and building-integrated applications. Yang et al. also made a flexible device directly on polyimide (PI) substrates, thereby eliminating the need for expensive substrate lift-off processes. The flexible bifacial devices produced front and rear efficiencies of 15.36% and 6.61%, respectively. Although these values are inferior to those of glass-based alternatives, they indicate the viability of scalable roll-to-roll manufacturing. The main limitations in flexible devices arise from parasitic near-infrared absorption in the polyimide substrate and increased recombination loss resulting from shunt formation during the initial device definition. They mentioned that the implementation of thinner, colorless polyimide foils or other transparent polymers may reduce these losses, facilitating increased rear-side efficiencies [30].

Comparison with Previous TCO Back-Contact Studies: Historically, CIGS devices utilizing TCO back contacts have faced challenges in surpassing an efficiency of ≈16%, mainly attributed to $GaO_X$-induced resistive barriers and increased back-interface recombination. Previous bifacial strategies often relied on reducing the absorber layer's thickness to enhance rear-side transparency; however, this approach led to diminished absorption and compromised front-side performance. Yang et al. address longstanding trade-offs by concurrently achieving $GaO_X$-free interfaces, robust Ga back-grading, and thick absorbers with high crystalline quality [30]. In contrast to traditional molybdenum-based back contacts, which are opaque and hinder bifacial operation, transparent conductive oxides such as ITO and IO:H provide the advantages of optical transparency alongside adequate conductivity. Among the available TCOs, indium oxide:hydrogen (IO:H) is notably advantageous for bifacial designs due to its high near-infrared (NIR) transparency. In contrast, indium zinc oxide (IZO) offers a balance between optical performance and deposition stability. IO:H is acknowledged as the premier choice for next-generation bifacial CIGS back contacts, contingent upon maintaining compatibility with low-temperature CIGS growth [32, 33].

Doping and Interface Engineering Strategies for Further Efficiency Gains: Several strategies are identified to enhance the performance of bifacial CIGS in the future [29]. The incorporation of controlled Ag (4%–5% atomic content) is critical for expanding the process window and facilitating large-grain growth at lower temperatures. Adjusting the Ga back-gradient in terms of both magnitude and spatial distribution is an effective strategy for reducing rear-side recombination while maintaining a high $V_{OC}$. Optimization of alkali post-deposition treatments using NaF and RbF is necessary to achieve a balance between enhanced carrier concentration and trap-assisted tunneling at the TCO interface, while minimizing the creation of unwanted defects [30]. Optimizing sputtering conditions to reduce the parasitic absorption of ITO or substituting it with IO:H or IZO is essential for enhancing rear $J_{SC}$ from a materials standpoint. Further interface passivation methods, including the incorporation of ultrathin tunneling layers (e.g., $Al_2O_3$ or $MgF_2$), could mitigate recombination at the CIGS/TCO interface while maintaining effective carrier extraction. Device-level refinements, including optimized laser scribing, metallization, and flexible substrate engineering, are essential for converting laboratory-scale efficiencies into commercially viable bifacial CIGS modules.

### 2.1.2 | CIGS Narrow Bandgap

Narrow-bandgap CIGS, generally around ≈1.0 eV range through increased indium content or reduced gallium fraction, has achieved certified efficiencies of ≈20.26% [34]. While this is slightly below the record values of standard-gap CIGS (≈23.6% at 1.1–1.2 eV) with monofacial configuration, narrow-bandgap compositions offer distinct advantages in optoelectronic design, especially in multijunction and bifacial applications, as the comparison mentioned in Table 1. Their extended absorption in the near-infrared region (up to ≈1250–1300 nm) enables the capture of photons that standard-gap or wide-gap absorbers cannot, thus enhancing photocurrent generation in tandem stacks or bifacial configurations where supplementary light is accessible from rear-side reflection or transmission.

Narrow-gap CIGS functions effectively as a bottom absorber in tandem solar cells when combined with wide-bandgap perovskites, CdTe, or chalcogenides, applicable in both 2-terminal and 4-terminal configurations [36–38]. The spectral complementarity facilitates the absorption of high-energy photons by the top cell, while the narrow-gap CIGS captures sub-bandgap photons, thus improving current matching and overall device efficiency. Narrow-gap CIGS in bifacial configurations provides additional advantages by harnessing longer-wavelength rear-side photons, which are scattered or reflected from high-albedo surfaces, thereby enhancing energy yield compared with front-only operation. Bifacial narrow-gap CIGS devices, when integrated with transparent back contacts like ITO, or ultrathin metal/oxide composites, demonstrate effective carrier collection with reduced optical loss. Despite ongoing challenges, such as non-radiative recombination, $V_{OC}$ deficits, and stability issues, the strategic importance of narrow-gap CIGS in facilitating bifacial tandem architectures for the bottom cell renders it essential for next-generation photovoltaic systems that seek to exceed the single-junction Shockley–Queisser limit.

#### 2.1.2.1 | Strategies & Advances in Bifacial Narrow-Bandgap CIGS SCs.

Ali et al. provide a thorough demonstration of narrow-bandgap low-Ga doped $CuInSe_2$ (CISe) (only 5 min of

**TABLE 1** | Summary of the photovoltaic parameters for the highest-efficiency CIGS solar cell obtained from a monofacial configuration.

| CIGS bandgap category | Composition and substrate | Record efficiency (%) | Key benefits | Main challenges |
|---|---|---|---|---|
| Narrow [34] | Ga-graded/MoCuInSe$_2$-rich (low Ga) | 20.26 | Extends absorption into NIR (≈1300 nm); essential for bottom cells in tandems | Lower $V_{OC}$, higher recombination, reduced stability vs. standard-gap |
| Standard [21] | Glass substrate/Mo Balanced In/Ga (≈Cu(In, Ga)Se$_2$) | 23.6 | High efficiency; good trade-off between $V_{OC}$ and $J_{SC}$ | Material supply (In, Ga); efficiency ceiling approaching SQ limit |
| Wide [35] | Mo/ZnSnO buffer, Cd-free Ga-rich CIGS | 15.7 | High $V_{OC}$; suitable as top cell in tandems; reduces thermalization losses | Lower $J_{SC}$ due to reduced NIR absorption; phase segregation risks |

Gallium deposition during first stage) bifacial solar cells utilizing ITO back contacts, as clearly demonstrated by the schematic diagram Figure 2a; the schematic also explains the bifacial mechanism, how light can come simultaneously from both sides, and helps to enhance overall efficiency [39]. The introduction of a thin Ag interfacial layer (≈5 nm), in conjunction with low-temperature co-evaporation (420°C–390°C actual substrate temperatures), effectively suppresses the formation of the resistive $GaO_X$ interlayer and stabilizes the growth of large-grained CISe. Their optimal devices achieved a front-side efficiency of 15.3% at 420°C and a rear-side efficiency of 8.44% at 390°C, resulting in a bifacial power generation density (BPGD) of 23.1 mW cm$^{-2}$ under 2.0 suns (front + rear) as shown in JV curve Figure 2b [39]. This indicates the peak performance recorded for narrow-bandgap CISe devices featuring transparent back contacts, establishing them as viable options for bifacial tandems and lightweight or semi-transparent solar modules [40].

Mechanisms Behind Performance Improvements: The research demonstrates that Ag alloying reduces crystallization temperature, enhances grain size, and refines band edges, concurrently inhibiting $GaO_X$ formation at the low Ga-doped CISe/ITO interface. Figure 3a–f Illustrated STEM-EDS line scans and elemental mapping demonstrate the influence of deposition temperature on $GaO_X$ production at the ACISe/ITO interface. At 460°C, a significant buildup of Ga with an overlapping O signal suggests a $GaO_X$ layer of ≈3–4 nm, which diminishes to about 1–2 nm at 420°C and practically disappears (<1 nm) at 390°C. The EDS mapping and HAADF images validate that decreasing the growing temperature significantly inhibits interfacial $GaO_X$ production, consequently diminishing recombination and contact resistance [39]. This underscores the significance of low-temperature processing in enhancing back-interface quality in bifacial CISe devices, preserving an efficient back surface field enabled by Ga back-grading. This combination accounts for the high fill factors (>70%) and exceptional rear-side collection observed in their devices.

Bifacial and Transparent Application Benefits: Narrow-bandgap CISe is advantageous for transparent and bifacial applications due to its ≈1.0 eV bandgap, facilitating absorption into the near-infrared spectrum. When combined with transparent TCO back contacts like ITO, IO:H, or IZO, the devices allow for substantial transmission of visible light, facilitating the development of semitransparent modules suitable for windows, skylights, and facades. Narrow-gap devices, in contrast to wide-gap or standard-gap absorbers, achieve a balance between reduced visible absorption and effective near-infrared (NIR) harvesting, thereby facilitating the generation of useful current under both front and rear illumination.

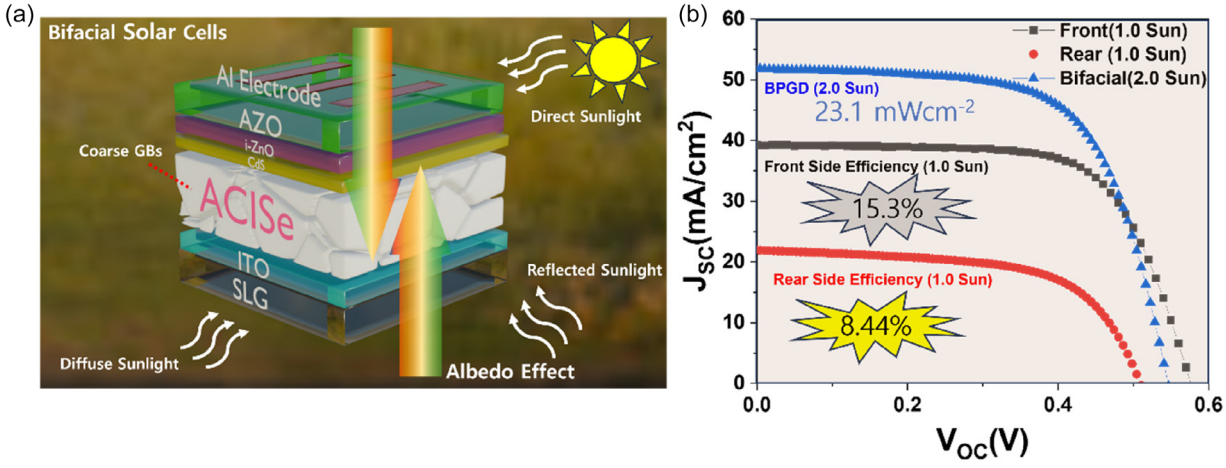


**FIGURE 2** | (a) Device schematic of a narrow bandgap bifacial ACISe solar cell with ITO back contact. (b) J–V curves the best cell of front, rear, and bifacial configurations. Reproduced with permission [39]. Copyright 2025, John Wiley and Sons.

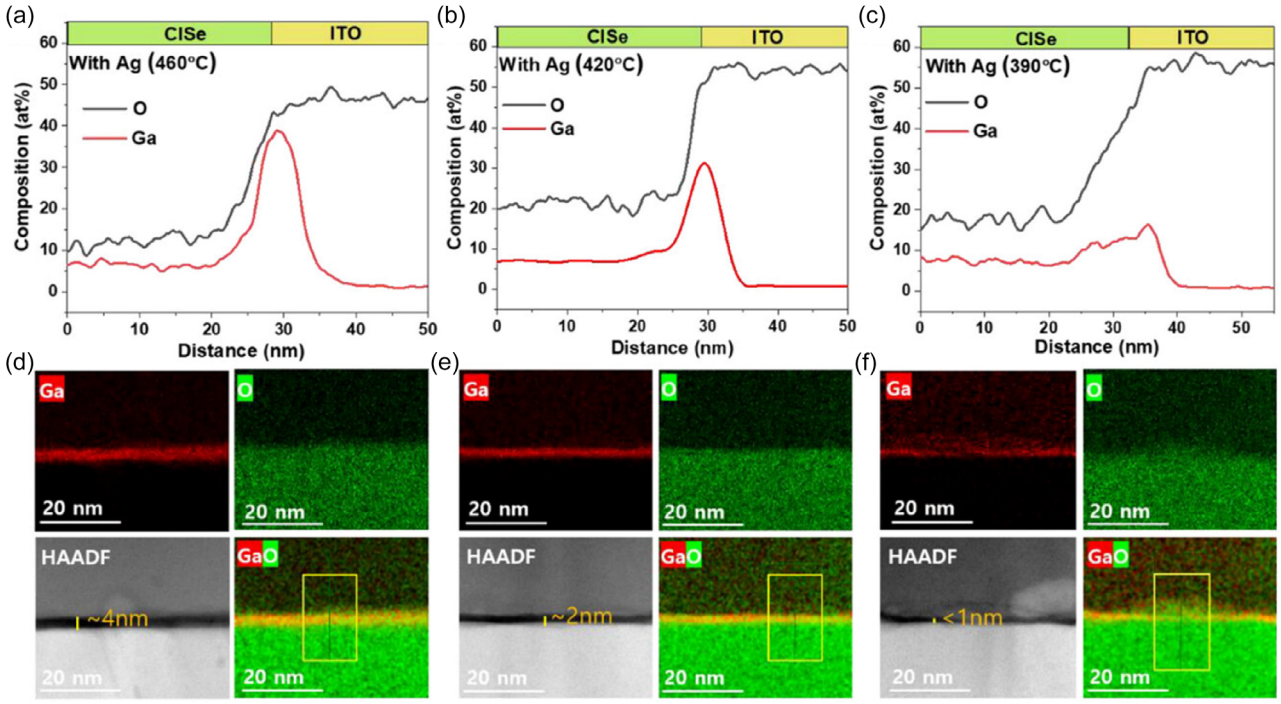


**FIGURE 3** | (a–c) TEM-EDS line scans of Ga and O across the ACISe/ITO interface for 460°C, 420°C, and 390°C. (d–f) EDS mapping images of Ga and O, as well as high-angle annular dark-field (HAADF) STEM images of the ACISe/ITO interface for the same temperature conditions. Reproduced with permission [32]. Copyright 2025, John Wiley and Sons.

Comparison with Prior Research on Bifacial Chalcopyrites: Previous studies on bifacial CIGS/CISe encountered challenges in achieving high efficiencies, primarily due to the use of very thin absorbers aimed at enhancing rear transparency or the significant formation of $GaO_X$ at the TCO interface. Keller et al. reported an efficiency of 16.1% utilizing IO:H as a back TCO; however, the rear-side performance was not comprehensively characterized, and parasitic absorption continued to pose a challenge [41]. Recent advancements in standard-bandgap bifacial CIGS, utilizing ITO back contacts, have reached efficiencies of 19.77% for the front and 10.89% for the rear, alongside a bifacial power generation density (BPGD) of ≈23.0 mW $cm^{-2}$ under 1.3 sun illumination (albedo). However, these devices were designed to operate within the conventional 1.1–1.2 eV bandgap range [30]. Ali et al. focused on narrow-bandgap CISe, crucial for bottom-cell functionality in tandem configurations with <1.65 eV bandgap perovskite or CdTe top cells [39]. This addresses a gap in the literature by establishing a benchmark for ≈1.0 eV absorbers that exhibit both bifacial and transparent characteristics.

Best TCO Choice for Bifacial Configurations: Among candidate back contacts, ITO is the most established material for bifacial CISe due to its favorable band alignment, sufficient conductivity, and recognized deposition techniques. Nonetheless, parasitic absorption in the near-infrared continues to restrict rear-side $J_{SC}$. IO:H (H-doped $In_2O_3$) demonstrates enhanced mobility and superior transparency, particularly at longer wavelengths, positioning it as a highly suitable choice for narrow-bandgap devices essential for infrared harvesting [42]. IZO (In–Zn–O) has been identified as a viable alternative, offering a balance between conductivity and transparency while ensuring enhanced processing stability. In contrast, AZO (Al:ZnO) and FTO ($SnO_2$:F) exhibit higher absorption or suboptimal valence band alignment, resulting in reduced efficiencies. Current evidence indicates that IO:H is the most promising back contact for bifacial transparent CISe, contingent upon controlled growth temperatures to prevent oxidation.

Doping and Interface Engineering for Future Gains: Future strategies may enhance the efficiency of bifacial narrow-bandgap CISe. Ag alloying (≈1–2a t%) has been demonstrated to increase grain size and reduce the optimal growth temperature, which is essential for inhibiting $GaO_X$ [29]. Ga back-grading can be optimized to minimize rear recombination while preserving a robust back-surface field. Alkali treatments (Na, Rb, K) enhance carrier concentration and decrease trap density; their profiles should be optimized for TCO back contacts instead of Mo-based references. Rear passivation layers, such as ultrathin $Al_2O_3$, $MgF_2$, or $MoO_X$, when combined with tunneling or dipole engineering, can effectively reduce recombination at the CISe/ITO interface without increasing series resistance. Switching to IO:H or IZO and optimizing sputtering to minimize near-IR absorption would directly improve rear-side $J_{SC}$ on the TCO side. Collectively, these methods can enhance bifacial narrow-bandgap CISe devices, positioning them as suitable options for bifacial tandem bottom-cell applications that benefit from the capture of both direct and reflected/diffuse light [39].

### 2.1.3 | CIGS Wide Bandgap

Wide-bandgap CIGS (Cu(In, Ga)(S, $Se)_2$) solar cells, characterized by band gaps of ≈1.4 to 1.6 eV, are increasingly recognized for their capacity to achieve elevated $V_{OC}$, enhanced thermal stability, diminished recombination losses, and significant compatibility with tandem configurations as top-cell absorbers [43]. Although wide-bandgap CIGS variants currently exhibit lower

absolute efficiency compared with narrow-bandgap counterparts, significant laboratory efficiencies have been achieved. For example, a wide-bandgap (≈1.6 eV) CIGS cell recorded a $V_{OC}$ of 971 mV and a calibrated PCE of 15.7%, indicating considerable potential for high-performance tandem applications [35, 44]. In contrast, the maximum laboratory efficiency for narrow-bandgap CIGS (≈1.0 eV) is 20.26% as mentioned in Table 1, attained through optimized gallium grading and post-deposition treatment. Simultaneously, the overall efficiency of standard CIGS, without particular emphasis on wide or narrow bandgap tuning, has achieved a maximum of 23.64%, as confirmed by independent assessments [30]. Consequently, while wide-bandgap CIGS presently falls short in terms of absolute efficiency, its elevated $V_{OC}$ and compatibility for tandem applications render it essential for the advancement of high-efficiency, multi-junction photovoltaics—where it frequently surpasses conventional or narrow-band-gap alternatives in integrated system performance.

**2.1.3.1 | Strategies and Advances in Wide-Bandgap Bifacial CIGS SCs.** Wide-bandgap CIGS (≈1.4–1.6 eV) has become the favored absorber for bifacial and semitransparent thin-film solar cells due to its ability to provide higher $V_{OC}$ and lower thermalization losses in comparison to standard-gap CIGS (≈1.1–1.2 eV) and narrow-gap alloys (≈1.0 eV). Narrow-gap CIGS exhibits elevated $J_{SC}$; however, it experiences significant $V_{OC}$ losses and lacks adequate transparency, rendering it inappropriate for bifacial applications. Wide-gap alloys, although exhibiting larger $V_{OC}$ deficits, can accommodate thinner absorber layers, which is crucial for light transmission through transparent back contacts (TBCs). Modeling and experimental studies demonstrate that bifacial energy yield in wide-gap devices can surpass that of monofacial standard-gap CIGS under realistic albedo conditions. Wide-bandgap CIGS solar cells are advantageous for tandem architecture due to their elevated bandgap, which facilitates effective absorption of visible photons and sustains high $V_{OC}$. This enables effective functioning as the top cell in conjunction with low-bandgap absorbers like CISe, standard-gap CIGS, or silicon, which capture the transmitted near-infrared photons. The tunable composition, strong thermal stability, and proven thin-film scalability of wide-gap CIGS make it attractive for both 2-terminal monolithic and 4-terminal mechanically stacked tandem devices, for the top cell. Additionally, the incorporation of transparent back contacts in wide-gap CIGS enables bifacial operation, which enhances photocurrent and overall tandem efficiency.

Device Configurations for Bifacial CIGS: Two primary configurations are prevalent in bifacial CIGS: (i) ultrathin semitransparent absorbers applied on transparent conductive substrates like ITO, IOH, FTO, or $In_2O_3$:W/H and (ii) locally contacted, passivated rear architectures that integrate transparency, reflection, and surface passivation. Results indicate that TBC-based bifacial devices attain front efficiencies within the 10%–14% range, accompanied by bifacial gains of 10%–20%. In contrast, rear-passivated designs demonstrate improved $V_{OC}$ retention, albeit with restricted optical transparency. In comparison to standard-gap devices utilizing opaque Mo back contacts, which achieve a record efficiency of 23.6%, bifacial wide-gap devices exhibit a reduction in efficiency. However, they facilitate additional current generation on the rear side, thereby enhancing their potential for higher energy yield over time.

Transparent Back Contacts and Experimental Milestones: A significant achievement was the demonstration of a 13.6% bifacial ACIGS cell utilizing $In_2O_3$:W/H as the TBC (Eg ≈ 1.44–1.52 eV), confirming that Ga/Ag-rich wide-gap absorbers can sustain $V_{OC}$ while facilitating rear-side collection as mentioned in Table 2 [45]. To further investigate the structural characteristics and interface quality of these devices, Figure 4 compares wide-gap ACIGS solar cells with 400 nm and 1 μm absorbers using $In_2O_3$:W (IOW) as a transparent back contact. SEM cross sections (Figure 4a,b) show the different absorber thicknesses, while STEM images (Figure 4c–e) reveal a very thin (≈1.5 nm) $GaO_x$ interlayer at the ACIGS/IOW interface. The EQE spectra Figure 4f–i demonstrate reduced carrier collection for rear illumination, with the rear $J_{SC}$ reaching ≈60%–62% of the front value. Normalized EQE/A plots, Figure 4g–j highlights stronger back contact recombination in the thinner absorber. JV curves in Figure 4h–k show front efficiencies of 8.3% (400 nm) and 14.0% (1 μm) with IOW, compared to Mo references, while rear illumination yields lower efficiencies (4.0% and 7.6%). Overall, the figure illustrates that thicker absorbers improve front and rear collection, but back contact recombination remains a limiting factor. Comparative studies indicate that IOH provides enhanced infrared transparency, which is advantageous for tandem designs [45]. In contrast, ITO exhibits lower resistivity and greater stability throughout the absorber deposition process. Initially, ITO/$MoO_3$ stacks emphasized the importance of appropriate band alignment, as inadequate conduction-band offsets resulted in blocking behavior. Standard-gap CIGS with opaque Mo consistently achieves efficiencies greater than 20%. In contrast, bifacial

**TABLE 2** | Summary of the photovoltaic parameters for the highest-efficiency CIGS solar cell obtained from a bifacial configuration.

| CIGS bandgap category | Typical composition | Substrate | Front efficiency (%) | Rear efficiency (%) |
|---|---|---|---|---|
| Narrow [39] | Ag-alloyed $CuInSe_2$ (CISe) on transparent substrate (AAC≈0.02) | ITO/Ag/CISe bifacial cell | 15.3 | 6.9 |
| | | | 13.3 | 8.44 |
| Standard [30] | CIGSe (typical Ga content) (AAC≈0.05) | Bifacial ITO/CIGS with transparent rear electrode | 19.8 | 10.9 |
| Wide [45] | Wide-gap (Ag, Cu)(In, Ga)$Se_2$ (ACIGS) (AAC≈0.8) | $In_2O_3$:W transparent rear electrode; bifacial | 13.6 | 8.7 |

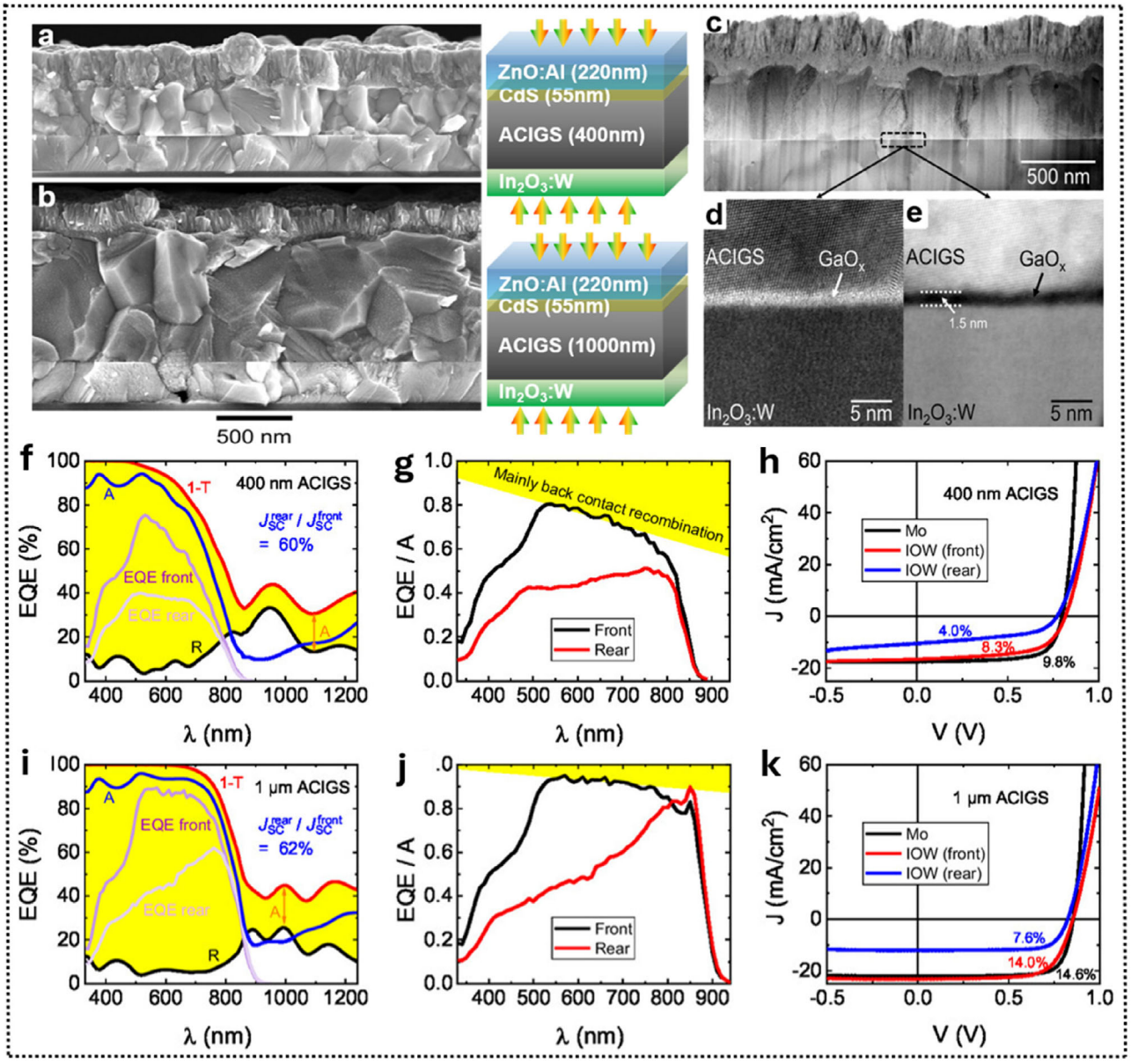


**FIGURE 4** | (a and b) Cross-sectional SEM and schematics of ACIGS devices with 400 nm and 1 μm absorbers. (c–e) STEM bright-/dark-field images of the 400 nm device and back-contact region. (f and g) EQE, R/T/A, and normalized EQE spectra. (h) JV curves of the best IOW TBC device vs. Mo reference. (i–k) Corresponding results for the 1 μm absorber device. Reproduced with permission [45]. Copyright 2024, John willey and sons.

wide-gap prototypes demonstrate their effectiveness in tandem and energy-yield-optimized systems.

Interface Engineering in Wide-Gap Bifacial CIGS: Substituting CdS with Zn (O, S) buffers has demonstrated significant advantages for wide-gap absorbers, enhancing blue response and conduction-band alignment when the O/S ratio is meticulously regulated. $Al_2O_3$ passivation at the rear, utilizing nanoscale local contacts, diminishes surface recombination and preserves $V_{OC}$ in ultrathin absorbers ranging from 500 to 800 nm [45]. The enhancements enable bifacial wide-gap devices to partially recover their $V_{OC}$ deficit in comparison to standard-gap CIGS, where CdS/Mo contacts continue to be effective but are less suited for semitransparent operation. Narrow-gap CIGS derives limited advantages from interface strategies due to their $V_{OC}$ being inherently constrained by band-gap limitations.

Doping and Defect Engineering Strategies: Doping and defect management are critical factors in enhancing the performance of wide-gap bifacial CIGS. Post-deposition treatments with alkali fluorides (KF, RbF, CsF) reduce defects and improve grain-boundary passivation, with RbF-PDT demonstrating the most consistent enhancements in $V_{OC}$ for wide-gap absorbers [46]. Alloying with Ag (ACIGS) diminishes band-tail states and decreases recombination losses, which is especially important in materials with high Ga content where defects typically prevail [47]. Experimental comparisons indicate that wide-gap ACIGS with alkali-PDTs achieves ≈15%–16% efficiency, which remains below the standard-gap CIGS records of around 23.6%, yet is considerably higher than untreated wide-gap devices, which exhibit efficiencies of about 10%–12% [47].

Comparison and Outlook for Wide-Gap Bifacial CIGS: Compared with standard-gap CIGS, wide-gap bifacial devices currently deliver lower absolute efficiencies but excel in system-level performance due to higher $V_{OC}$, bifacial gains, and tandem compatibility. Narrow-gap CIGS, while strong in current generation, cannot compete in bifacial or semitransparent configurations due to its low $V_{OC}$ and poor transparency. Today's wide-gap bifacial prototypes (≈13%–16%) have matured significantly from early TCO/$MoO_3$ concepts and show clear design-optimized TBCs, rear passivation, Zn(O, S) buffers, and alkali/Ag defect control. Remaining challenges include high-resistivity TBCs, rear-interface recombination, and maintaining favorable band offsets at higher Ga/Ag ratios. If these are solved, wide-gap bifacial CIGS could bridge the gap to 18%–20% efficiency and become essential for tandem photovoltaics [48, 49]. A detailed comparison of high reported efficiencies of CIGS solar cells in monofacial and bifacial topologies is presented in Tables 1 and 2, including narrow, wide, and standard-bandgap devices. The topic emphasizes absorber compositions and critical parameters affecting device performance, such as bandgap engineering, alloying techniques, interface passivation, and back-contact optimization.

### 2.1.4 | Challenges in CIGS Bifacial Devices

Standard, narrow-bandgap, and wide-bandgap CIGS solar cells encounter specific scientific and technical challenges that restrict enhancements in efficiency. The standard bandgap of CIGS shows potential due to its high efficiency and appropriate bandgap for tandem applications; however, efforts must be directed toward minimizing the $V_{OC}$ deficit. The deficit around 0.4–0.5 V is primarily attributed to nonradiative recombination at the CdS/CIGS interface and the existence of deep defect states within the absorber. Uniform gallium grading across large-area absorbers presents challenges, resulting in bandgap fluctuations and inhomogeneity in carrier collection [50]. Narrow bandgap CIGS (≈1.0 eV), although suitable for bottom cells, experiences low open-circuit voltage ($V_{OC} < 0.6$ V) because of its reduced bandgap, which increases bulk and interface recombination. Wide bandgap CIGS (>1.4 eV) encounter significant challenges related to band tailing and Cu-poor phase segregation. These issues result in a broadened absorption edge and an increased Urbach energy (≥20 meV), ultimately diminishing both $V_{OC}$ and FF [51]. Moreover, attaining elevated carrier mobility and precise control of Cu/Ga stoichiometry presents significant technical challenges, frequently resulting in suboptimal collection efficiency.

The TBC represents the primary limitation for bifacial CIGS devices. Substituting Mo with TCOs like ITO, AZO, or ZnO:Ga presents challenges. Although these materials provide transparency exceeding 80% in the visible spectrum, their sheet resistances of 10–15 Ω/sq are higher than that of Mo, which restricts current extraction. These oxides degrade under thermal stress (>200°C), which affects module reliability. Trade-offs between optical and electrical properties occur; excessively thin TCO leads to increased resistance, whereas thicker layers diminish rear-side transparency and bifacial gain [52]. In tandem bifacial devices, achieving precise current matching between wide (1.6–1.7 eV) and narrow (1.0–1.15 eV) absorbers is challenging due to spectral imbalance and parasitic absorption in intermediate layers, including recombination junctions and tunnel oxides. Additionally, multi-junction stacks are required to endure thermal cycling, interdiffusion of alkali metals (Na, K), and lattice mismatch, factors that can compromise long-term stability. Scaling to the module level necessitates low-temperature sputtering (below 150°C) for transparent conductive oxides on flexible substrates, ensuring adhesion, transparency, and minimal light scattering are maintained. Resolution of these integrated scientific and engineering challenges is essential for bifacial CIGS tandems to achieve their anticipated efficiency exceeding 30% [53].

### 2.1.5 | Future Aspects of CIGS Bifacial Devices

The future of CIGS solar cells involves utilizing the complete bandgap tunability of the material to address various applications and to mitigate existing limitations. Standard bandgap CIGS (≈1.1–1.2 eV) will continue to serve as the primary technology for stable, high-efficiency single-junction modules, particularly as advancements in alkali postdeposition treatments, defect passivation, and cost-effective flexible processing progress. Narrow bandgap CIGS (≈0.9–1.0 eV) is poised to be essential as the bottom absorber in tandem configurations due to its superior infrared response and compatibility with wide bandgap materials. Currently, wide bandgap CIGS (≈1.6–1.7 eV) is under development for implementation as top absorbers in tandem configurations and for applications necessitating partial transparency, including BIPV and transparent energy-harvesting windows. Challenges, including band tailing, phase segregation, and voltage deficits in wide bandgap absorbers, alongside recombination losses in narrow bandgap devices, necessitate solutions through enhanced interface engineering, compositional grading, and sophisticated passivation strategies.

Bifacial and tandem CIGS architectures are poised to surpass the efficiency limits of single-junction devices, thereby creating new deployment opportunities. Bifacial CIGS modules improve energy yield by harnessing reflected and diffuse light, making them appropriate for agrivoltaics, building-integrated photovoltaics (BIPV), and installations on high-albedo surfaces. However, their effectiveness is contingent upon the advancement of durable, transparent, and conductive back contacts. The integration of narrow–wide bandgap CIGS tandems, especially in bifacial configurations, presents a viable pathway to achieve maximum power generation density exceeding 30 mW/cm$^2$. Narrow-bandgap CIGS solar cells are well-suited as bottom cells, while wide-bandgap CIGS devices are advantageous for use as top cells, making both configurations highly compatible with tandem architecture in both 2T and 4T designs, as shown in Figure 5. This approach utilizes high-energy photon absorption in the wide-bandgap top cell, while the narrow-bandgap bottom cell captures near-infrared photons. Future implementation will focus on the development of transparent front and rear electrodes, precise current matching, scalable deposition of multijunction stacks, and ensuring long-term stability under thermal and light-induced stress. Addressing these challenges may enable tandem and bifacial CIGS devices to compete directly with perovskite/silicon tandems, providing a scalable, stable, and efficient thin-film solution for the next generation of photovoltaics.

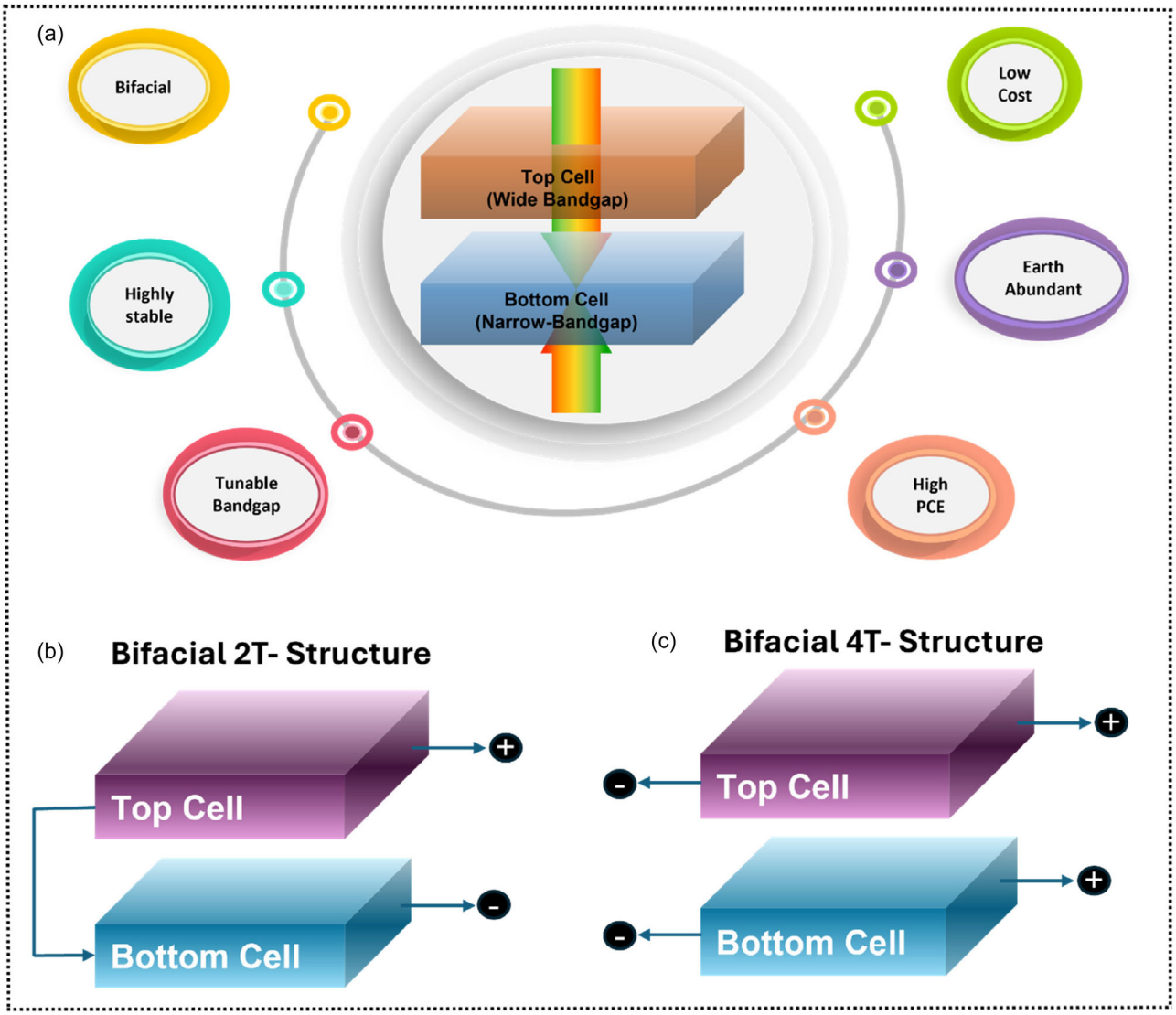


**FIGURE 5** | (a) Schematic illustration of Tandem SCs featuring a chalcogenide-based wide bandgap absorber layer as the upper cell and a narrow bandgap lower cell. (b and c) Schematic diagram of the connection in 2T and 4T chalcogenide top and bottom cell device structures.

## 2.2 | CdTe Solar Cells

Cadmium telluride (CdTe) solar cells are widely used for thin film photovoltaics due to their near-ideal direct bandgap (≈1.45–1.5 eV), high absorption coefficient ($>10^{-4}$ $cm^{-1}$), and chemical stability, which together provide efficient solar energy conversion at low production costs [54]. CdTe crystallizes in the zinc blende cubic structure [55]. Additionally, two configurations support CdTe: substrate and superstrate (Figure 6a,b). In the superstrate configuration, where light enters through a transparent glass and passes sequentially through layers of TCO, CdS, and CdTe before reaching the back contact, it boasts the highest efficiencies reported for CdTe solar cells thus far. This approach benefits from excellent chemical durability and is ideal for large-scale commercial modules, but its rigidity limits use in lightweight and flexible applications. In contrast, the substrate configuration, where the cell is fabricated on a metallic substrate, with light incident through TCO and absorber layers down to the back contact, allows for lighter, as well as mechanically flexible devices suitable for portable or building-integrated applications. In the fabrication of CdTe solar cells, a $CdCl_2$ activation step is carried out at temperatures ranging from 350°C to 450°C and has been shown to drastically improve the performance of CdTe solar cells [57]. High efficiency has been achieved in superstrate conditions due to many factors. First, in the substrate configuration, the $CdCl_2$ treatment can be applied to CdS alone or to both CdS and CdTe. The former leads to poor CdTe crystallinity, while the latter improves the crystallinity of CdTe but can drive impurities toward the preformed ohmic contact and alter it [58]. In both cases, the diffusion of impurities is difficult to control. However, in the superstrate configuration, the diffusion of impurities toward the back contact is limited because the back contact is formed after all the high-temperature deposition processes are carried out. Additionally, substrate configuration exhibits more pronounced back barrier heights, increased carrier recombination, and greater interface defects due to inherent challenges in back contact formation and interface management, factors that are better controlled in superstrate configurations [58]. In this section, we provide a review of the recent advances in bifacial CdTe solar cells, providing insights into the developments of transparent back

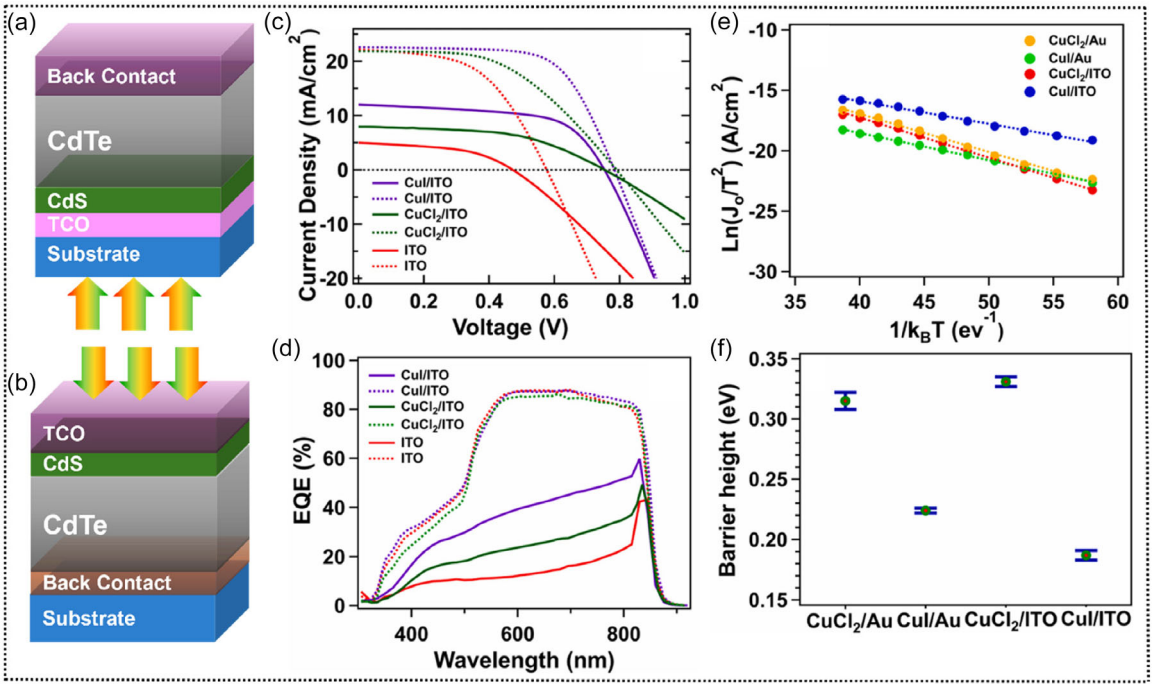


**FIGURE 6** | (a) Substrate and (b) superstrate configurations (c) J–V and (d) EQE curves of champion bifacial CdTe with $CuCl_2$ interfacial layer (e and f) back-barrier height estimation based on the thermionic model. Reproduced with permission [56]. Copyright 2021, Elsevier.

contacts, materials engineering, and device architectures that have improved rear-side illumination efficiency.

Bifacial CdTe solar cells have been developed in both superstrate and substrate configurations, with the superstrate design enabling high efficiencies. One of the earliest reports on bifacial CdTe technology was presented by Romeo et al. [59], who compared devices with transparent ITO and standard Cu/Au back contacts in a superstrate configuration (glass/FTO/CdS/CdTe). ITO, sputtered and annealed at 350°C with light soaking, improved efficiency from 1% to 2% to 5%, while Cu/Au with post-deposition treatment reached ≈10%. The improvements were linked to the reduced recombination at the CdTe/ITO interface. Introducing small amounts of Cu into ITO helped balance transparency and stability. Devices with 3 nm Cu degraded but stabilized after ≈4 years, while <0.5 nm Cu devices improved over time. Rear-side efficiency started at ≈0.5% and rose to 2.1% after light soaking. The reduced rear-side efficiency compared to the front was explained by the generation of electron–hole pairs deep in the absorber, far from the p–n junction, leading to significant carrier recombination before collection. Reducing absorber thickness from 2.5 to 1 µm and Cu to <0.3 nm increased rear efficiency to 3.2%, though front efficiency fell from 10.3% to 8%. This work highlighted the critical role of annealing, light soaking, and careful incorporation for stabilizing ITO-based transparent back contacts. While front-side efficiencies were modest compared to Cu/Au contacts, the study was foundational in demonstrating bifacial operation and long-term stability trade-offs.

Marsillac et al. [60] advanced this with a transparent ZnTe:N/ITO back contact in ultra-thin (≈0.68 µm) CdTe, eliminating Cu. Efficiencies were 5.7% (front) and 5.0% (rear), showing that reduced thickness narrowed the front-rear gap but limited overall performance, compared with standard Cu/Au contacts (11.2%). Dark J–V analysis revealed that ITO devices suffered lower $V_{OC}$ (≈0.54 V vs 0.75 V), higher J0 ($1.3 \times 10^{-5}$ mA/cm$^2$), higher Rs, and lower $J_{SC}$ due to loss of Cu doping and the absence of back reflection from the metallic contacts. Building on this, Zhang et al. [61] replaced ITO with a tungsten-doped Indium Oxide (IWO) layer, forming a ZnTe: N/IWO composite transparent back electrode in thin (≈1 µm) CdTe bifacial solar cells. By optimizing the optical and electrical properties of the back contact stack through annealing of ZnTe:N, they achieved a 7.1% rear-illumination efficiency, the highest reported rear-side efficiency for CdTe absorbers <1 µm thick, though this came with a reduction in front-side efficiency to ≈5.7%. Dark J–V measurements revealed that direct contact between CdTe and IWO generated a barrier height of over 1 eV from their previous report. The insertion of the ZnTe: N layer reduced the potential barrier to ≈0.206 eV. The higher barrier height obtained from the IWO back contact alone was attributed to the formation of a Schottky barrier at the rear interface, which was reduced following the incorporation of the ZnTe:N layer. Further thinning of the absorber improved rear-side efficiency, resulting in additional front-side losses, highlighting the trade-off between optical and electrical optimization in bifacial CdTe devices.

These studies established two critical themes for subsequent bifacial CdTe research: i) The back contact must balance optical transparency with electronic quality. ii) The absorber thickness involves a trade-off, improving rear-side efficiency while potentially reducing front-side output.

### 2.2.1 | Strategies for Performance Enhancement in Bifacial CdTe Solar Cells

Back-Contact Engineering in Thicker CdTe Absorbers for enhancing Both Front and Rear-Side Efficiencies: Previous

studies on ultra-thin CdTe absorbers have shown that thinning the absorber can improve rear-side efficiency, but often at the cost of front-side performance. In contrast, thicker absorbers generally enhance front-side efficiency, yet the rear interface can limit overall bifacial performance. To address this, several reports have explored interface engineering at the back contact with thicker absorbers to optimize carrier collection and reduce recombination. In this section, we review those approaches, highlighting how careful back-contact engineering in thicker absorbers enables simultaneous improvements in both the front and rear-side efficiencies, providing a more balanced and high-performing bifacial device design. CdTe generally has a high electron affinity, and it tends to form a Schottky junction with the electrode. To reduce or overcome this Schottky barrier, high-work-function electrodes are required. However, most metal electrodes do not have the required high work function to overcome this barrier [62]. Inserting a back buffer layer between CdTe and the electrode can help improve performance by reducing recombination losses through optimal band alignment as well as passivation of defects, thereby improving $V_{OC}$ and FF. Copper doping is essential to the high performance of CdTe solar cells. Copper acts as an acceptor dopant in CdTe, increasing hole concentration, thereby promoting p-type conductivity of CdTe. Additionally, Copper facilitates the formation of a low-resistance back contact to CdTe, helping reduce contact losses and enabling efficient charge extraction. Similarly, in bifacial architectures, direct contact between the back contact and CdTe will lead to a high potential energy barrier that hinders the collection of charges. As such, by doping with copper, this potential barrier can be reduced, and an Ohmic back contact can be achieved. In bifacial architecture, all the materials used as back buffer materials are required to be transparent within the absorber's wavelength regions to ensure efficient light harvesting in the absorber. Before we delve into back contact interface engineering strategies, we would first like to establish some useful terms:

**Band bending**: Most back contacts do not have high work functions relative to the Valence band maximum (VBM) of CdTe. CdTe has a VBM of 5.8 eV below the vacuum level [63]. In bifacial architecture, transparent back contacts are used, such as ITO which has a work function between 4.4–4.7 eV, lower than the VBM of CdTe. When CdTe and ITO contact, it generally forms a Schottky barrier. Due to this, the energy bands tend to bend downward to achieve equilibrium. This downward band bending creates a barrier to holes and promotes electron accumulation at the interface, increasing recombination at the interface [64]. On the contrary, upward band bending means that the band edges curve upwards near the interface. This creates a barrier that repels minority electrons away from the interface, facilitating hole collection [65]. Thus, to reduce recombination rates, upward band bending or reduced downward band bending needs to be achieved.

**Initial Fermi Level Offset (IFLO)**: In back contact engineering strategies, the Fermi level offset is crucial to understanding the band bending. This is the difference in energy between the Fermi level of the absorber (CdTe) and the back buffer (HTL) at their interface. If the back buffer's Fermi level is deeper or lower than CdTe's, thus **Ef (absorber) - Ef (back buffer)** generates a positive value (+ve), the CdTe conduction and valence band both bend upward near the back buffer interface. This creates an energy barrier for electrons at the interface, suppressing interface recombination, thus improving $V_{OC}$. This is termed as positive initial Fermi level offset. Conversely, if the back buffer's Fermi level is higher than CdTe's, thus **Ef (absorber) – Ef (back buffer)** is negative (-ve), the energy bands of CdTe bend downward near the back buffer interface. This is known as negative initial Fermi level offset. This downward band bending generates a barrier for holes, causing hole accumulation at the back contact, increasing recombination, hence limiting $V_{OC}$. A positive IFLO results in upward band bending and the formation of an Ohmic contact, beneficial for hole collection at the back contact. Additionally, the IFLO is dependent on the hole concentration in CdTe. As the hole concentration increases, its Fermi level draws closer to the valence band. Thus, higher doping of the CdTe absorber results in a more positive IFLO relative to the back buffer [66].

**Back Surface Recombination Velocity (BSRV)**: This is a parameter that quantifies how quickly charge carriers recombine at the back surface of a solar cell. This is measured in cm/s. A high BSRV means carriers recombine more rapidly at the back contact, which reduces the number of carriers being collected, thus lowering the efficiency of the device. Thus, a lower BSRV is required. The BSRV, however, becomes less important as the Positive IFLO increases, because reducing or repelling the number of electrons at the back contact generally reduces recombination at the back surface [66].

Pokhrel et al. [56] addressed this challenge by introducing solution-processed copper iodide (CuI) nanoparticles as a hole transport layer (HTL) in a thick (3.5 μm) absorber. CuI combines high optical transparency in the visible range (≈3.1 eV), a deep work function (≈5.4 eV) for improved band alignment, and high hole mobility with substantial p-type conductivity. They first studied its effect on the standard monofacial Cu/Au back contact design. The efficiency increased from 14% to 14.8% relative to the Au electrode without CuI HTL, demonstrating its ability to form a lower resistance, more Ohmic back contact. More significantly, in bifacial devices (Glass/FTO/CdS/CdTe/CuI/ITO), CuI yielded balanced performance improvements on both sides: The rear-side efficiency reached 5.5% and the front-side, 11.1%, compared with 1.1%/7.0% and 3.2%/8.6% for the bifacial CdTe/ITO and CdTe/$CuCl_2$/ITO back contact designs respectively. The origin of the improved performance was probed via dark J–V-T analysis (190-300K) using the thermionic emission model: $J_0 \propto T^2 \cdot \exp\left[\frac{-q\cdot\varphi_b}{k_B T}\right]$, where $\varphi_b$ represents the back barrier height, $J_0$, saturation current, $q$ is an electronic charge, $T$ represents temperature, and $k_B$ is the Boltzmann constant. By plotting ln ($J_0/T^2$) against $1/k_BT$, they extracted the back barrier heights. Extracted barrier heights dropped from 331 meV ($CuCl_2$/ITO) to 187 meV (CuI/ITO) (Figure 6e,f), confirming that CuI significantly reduced downward band bending at the CdTe/ITO interface. This barrier reduction not only enhanced hole transport, improving $J_{SC}$, $V_{OC}$, and FF, but also mitigated electron recombination.

In another study, Subedi et al. [67] developed bifacial CdTe devices using $CuAl_XO_Y$ as a back buffer to improve rear-side efficiency. Different absorber thicknesses were tested: 3.3, 2.0, and 1.0 μm, with a device structure of Glass/FTO/CdS/CdTe/ITO. For the 1 μm absorber, the front-side and rear-side

efficiencies were 11.5% and 6.1% respectively (Figure 7a). When the thickness increased to 2 μm, the front and rear-side efficiencies also improved to 13.5% and 6.7% respectively (Figure 7b). At the highest thickness (≈3 μm), the front and rear-side efficiencies decreased to 12.5% and 5.6% respectively (Figure 7c). The rear-side FF remained consistently high (≈64%) across all thicknesses, indicating the rear interface was not a limiting factor. A lower FF would indicate downward band bending, which increases recombination. However, this was not the case. Additionally, the $J_{SC}$ remained nearly independent across the absorber thicknesses with very little change, suggesting a stable energy band profile at the rear interface. Time-resolved photoluminescence (TRPL) confirmed that incorporating the $CuAl_XO_Y$ buffer significantly improved carrier lifetimes on both the front and the rear-sides, reflecting reduced recombination at the rear interface (Figure 7d,e). Quantum efficiency (QE) analysis showed high collection of carriers generated by long-wavelength light at the front junction, but only about 50% collection efficiency for short-wavelength carriers near the back, indicating some recombination persists at the rear interface (Figure 7f). Despite this, the near independence of $J_{SC}$ and FF on thickness supports the claim that the rear interface was not a limiting factor. SCAPS modeling revealed a positive IFLO (≈0.07 eV) consistent with upward band bending, which helps repel electrons and reduce recombination (Figure 7g–j). However, the modeling also identified a relatively high BSRV value ($4 \times 10^{-6}$ cm/s), limiting the rear-side's $J_{SC}$. To further improve device performance, the authors applied an $MgF_2$ antireflection coating and an additional Ag metal grid, increasing the rear-side efficiency of the ≈3 μm CdTe absorber from 5.5% to 7.1%.

Building on the CuI nanoparticle back-contact engineering approach, Pokhrel et al. [68] introduced copper chromium oxide ($CuCrO_X$) as a back buffer in bifacial CdTe devices, motivated by its higher work function (5.1–5.25 eV), improved conductivity, and mobility of charge carriers. The buffer was spin-coated onto a ≈3.5 μm CdTe absorber and annealed at 200°C, with 8 min defined as the optimum annealing time. In monofacial devices with standard Au back contacts, efficiency improved from ≈13.9% ($CuCl_2$-treated reference) to 14.4% $CuCrO_x$ owing to enhanced minority-carrier lifetimes and interface quality. Most importantly, the $CuCrO_x$ back buffer was used in a bifacial stack, Glass/FTO/CdS/CdTe/$CuCrO_x$/ITO and compared to the standard Glass/FTO/CdS/CdTe ($CuCl_2$ treated)/ITO. The ITO-only device had a front and rear-side efficiency of 8.6%/3% which improved to 12.5%/7.6% for the $CuCrO_x$ back buffer device, marking the highest rear-side efficiency reported for bifacial CdTe with thick absorbers in the absence of anti-reflection coatings or metal grids. PL and TRPL were used to assess recombination rates and carrier lifetimes. The PL intensity for the

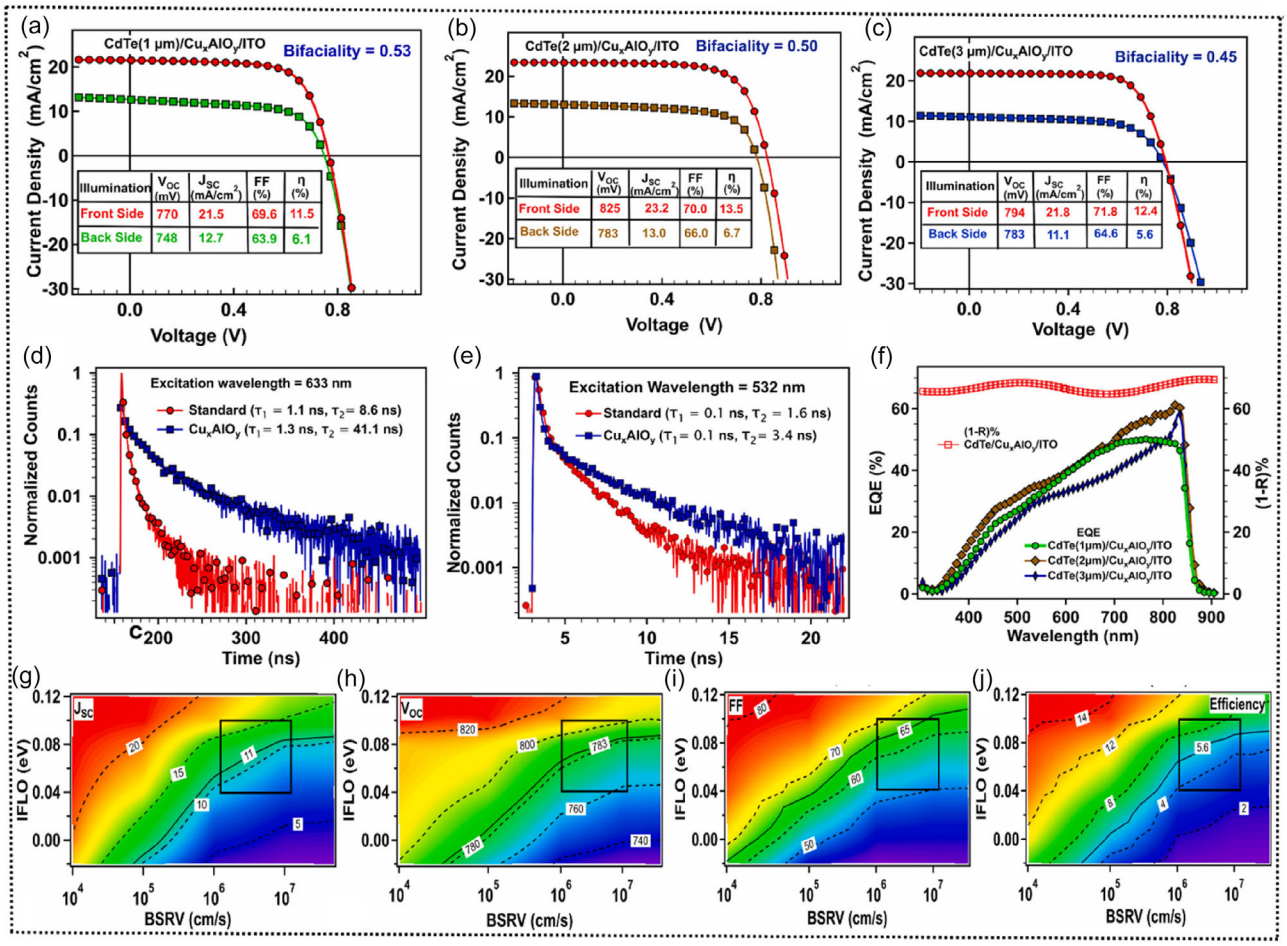


**FIGURE 7** | (a) 1 μm, (b) 2 μm, and (c) 3 μm CdTe absorber. TRPL response of 3 μm CdTe absorber with and without $Cu_XClO_Y$ illuminated from the (d) front-side and (e) rear-side of the device. (f) EQE response and reflection (1-R). SCAPS modeling highlighting BSRV and IFLO of the 3μm CdTe device on (g) $J_{SC}$, (h) $V_{OC}$, (i) FF, and (j) efficiency. Reproduced with permission [67]. Copyright 2021, Elsevier.

$CuCrO_X$ back buffer was higher than that of the reference sample with $CuCl_2$ treatment, indicating suppressed nonradiative recombination (Figure 8d,e). Additionally, there was an improvement in carrier lifetimes both at the front-side and rear-side following insertion of $CuCrO_x$ as the back buffer. Light-intensity independent $V_{OC}$ further supported this conclusion, with the $CuCrO_x$ device showing $\alpha$ values closer to the ideal of 1 (1.03 vs. 1.11 for $CuCl_2$-treated CdTe), indicating efficient charge transport (Figure 8h).

Muzillo et al. [69] advanced bifacial CdTe photovoltaics by integrating a $CuGaO_x$ rear buffer layer with cracked film lithography (CFL)-patterned Au micro-grids. This dual strategy directly targeted the three persistent bottlenecks of bifacial CdTe: (i) the difficulty of forming low-resistance ohmic contacts due to CdTe's high work function (≈5.7 eV) and its negative IFLO with TCOs, (ii) high lateral sheet resistance, and (iii) severe rear surface recombination. Positioned at the CdTe/rear interface, $CuGaO_x$ provided multiple benefits; its relatively high work function (≈5.38 eV) improved band alignment, while controlled Cu incorporation enhanced p-type conductivity and simultaneously passivated defects. In monofacial devices, this increased power density (18.0 to 19.8 mW/cm$^2$), $V_{OC}$ (0.829 to 0.844 V), and FF to 76.2% compared with the samples without the interfacial layer. For bifacial operation, $CuGaO_x$ with AZO back contacts showed performance loss: thick AZO (360 nm) yielded $V_{OC} = 0.817$ V, FF = 66.8%, and 16.8 mW/cm$^2$, while thin AZO (120 nm) further reduced FF to 60.3% due to contact resistance and Schottky barriers.

To overcome this, the authors used CFL, a low-cost solution-based lithographic process where a nanoparticle/polymer film cracks during drying to form a grid template (Figure 9a). Initial attempts to use CFL-patterned Au grids on $CuCl_2$-doped CdTe underperformed FF (60.4%) and $V_{OC}$ (0.812 V) due to contaminants and insufficient grid spacing. Replacing $CuCl_2$ with $CuGaO_x$ CFL-patterned Au grids restored beneficial doping and passivation, improving FF (63%) and $V_{OC}$ (0.829 V). To further reduce semiconductor resistance, a solvent cycling method was developed that increased crack density and grid connectivity, effectively narrowing the grid wire spacing. Sheet resistance measurements showed 17 Ω/sq for 360 nm AZO, 47 Ω/sq for the CFL grids without solvent cycling, and a significant improvement to 8.3 Ω/sq after solvent cycling, with only a slight reduction in transmittance. The CFL approach yielded uniform Au grids that balanced high optical transparency with good conductivity.

The resulting $CuGaO_x$/CFL grid back contacts balanced passivation, transparency, and conductivity, achieving a record FF of

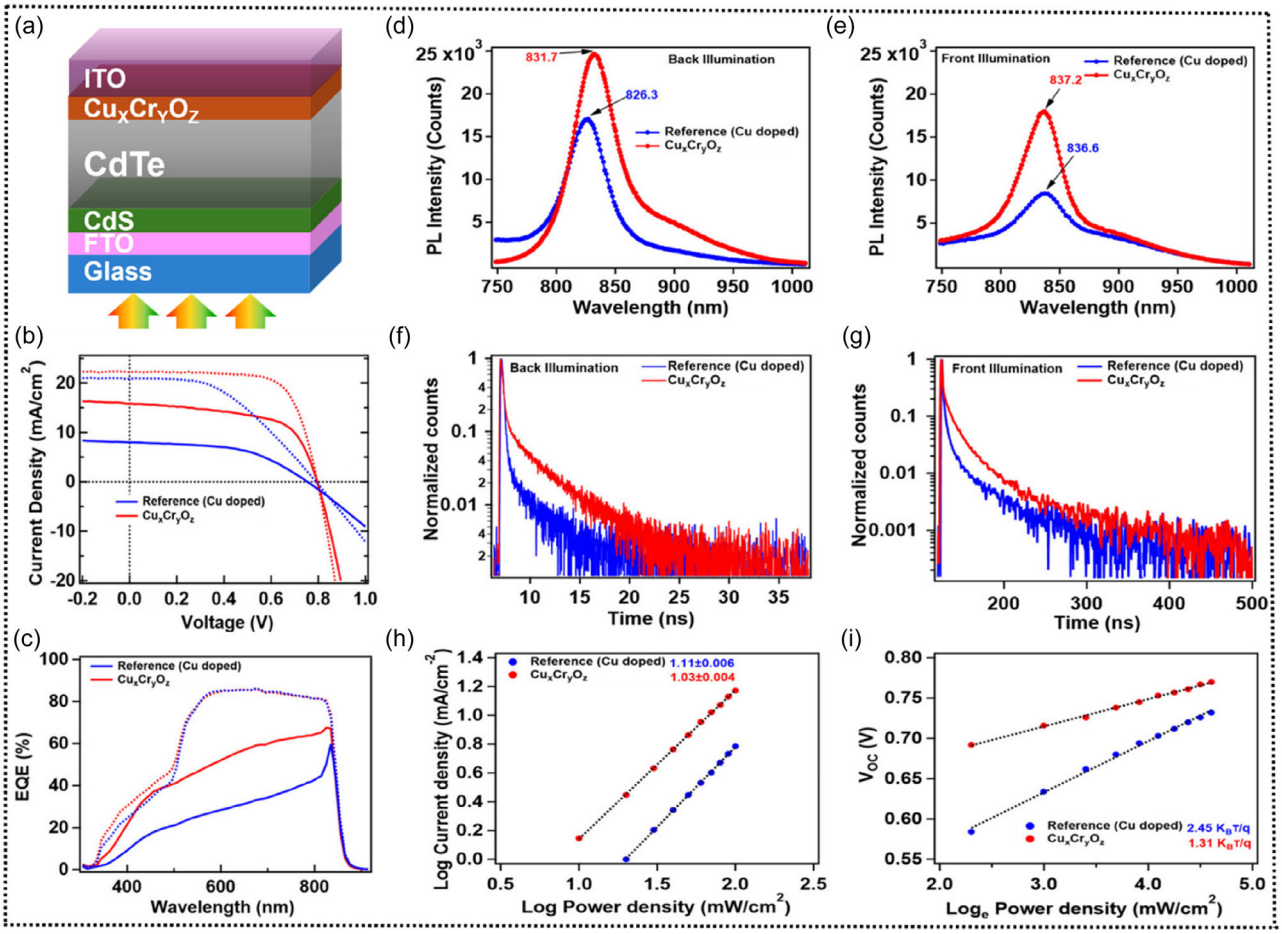


**FIGURE 8** | (a) Device structure, (b) J–V, and (c) EQE curves of champion devices (solid and dotted lines correspond to rear and front illumination, respectively). (d and e) PL and (f and g) TRPL responses of rear and front-side illumination of champion devices. (h) light intensity $J_{SC}$ and (i) $V_{OC}$ for rear illuminated devices. Reproduced with permission [68]. Copyright 2022, John willey and sons.

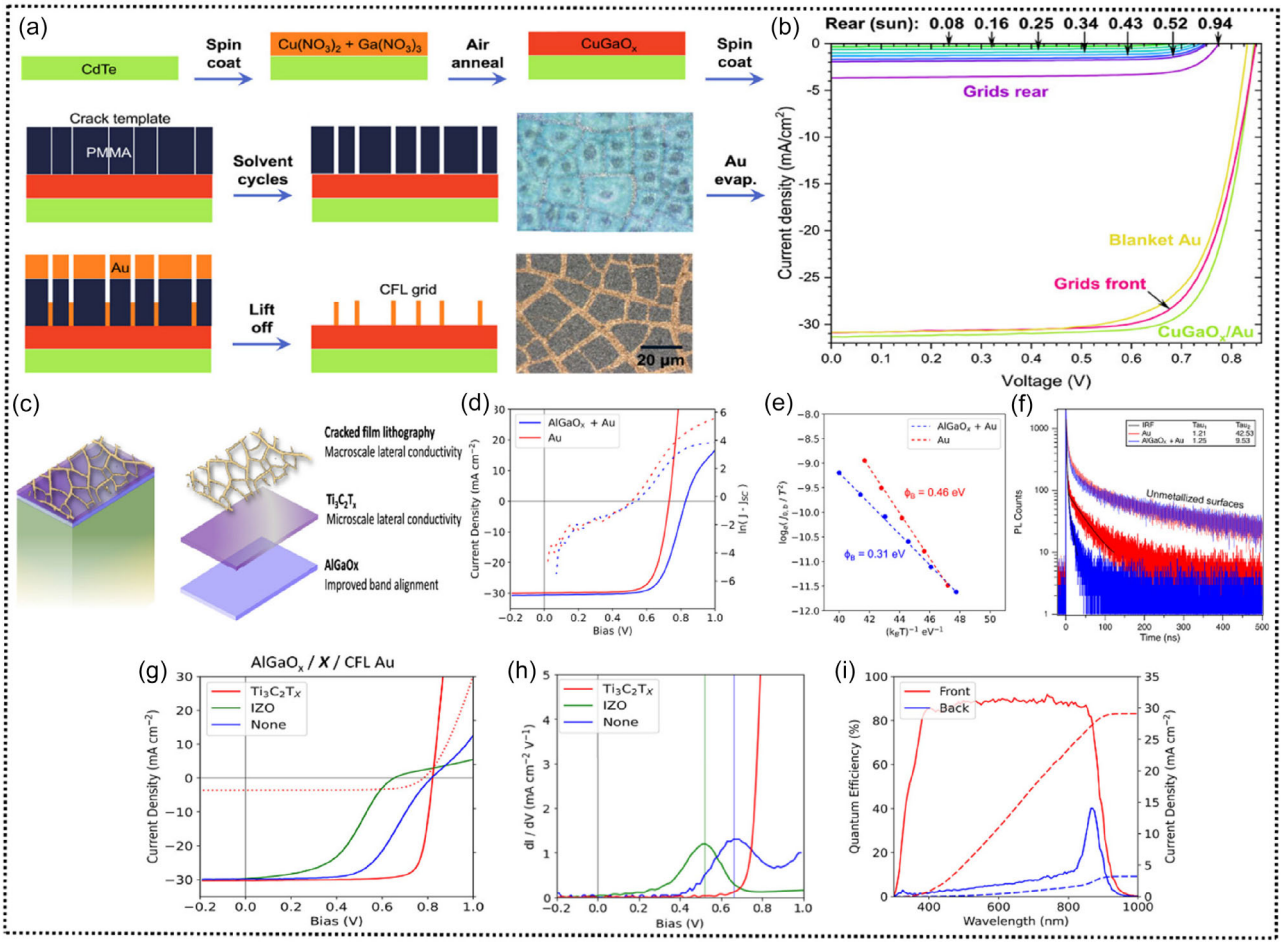


**FIGURE 9** | (a) Schematic of crack-template assisted fabrication of Au contact grid on CdTe/$CuGaO_x$ [69]. (b) J–V curves of CdTe solar cells with various rear contact configurations under increasing rear illumination (c) graphical representation of the hierarchical back contact (d) J–V, (e) barrier height, and (f) TRPL characteristics with a Au back contact and $AlGaO_x$ back contact. (g) J–V curves where X ($Ti_3C_2T_x$, IZO, and none). (h) Derivative of J–V indicating the onset of kink in a curve attributed to roll over due to the presence of a back barrier. (e) EQE curves for front and rear-side illumination of Hierarchical structure. (a and b) are reproduced with permission [69]. Copyrights 2023, John Wiley and Sons and (c–i) are reproduced with permission [70]. Copyright 2024, American Chemical Society.

73.3% under 1 sun front illumination, surpassing earlier bifacial CdTe reports. Under bifacial operation, they reached 20 mW/$cm^2$ at 1 sun front and 0.52 sun rear, a 25% improvement over the prior record, with measurable gains even at modest albedo (≈0.08 sun) (Figure 9b), though rear $J_{SC}$ remained limited, indicating further need for passivation and resistance reduction. These improvements will pave the way for even higher bifacial gains and commercial viability of CdTe photovoltaics.

Back contact engineering strategies represent one of the effective ways to enhance both front and rear-side efficiency in thicker CdTe bifacial devices. By doping with copper, the p-type conductivity of CdTe can be improved while recombination can be simultaneously suppressed. However, achieving a very high positive IFLO to induce upward band bending remains difficult due to inherent challenges associated with copper doping. As we have already stated, a more positive IFLO can be achieved by raising the p-type conductivity of CdTe, thus increasing the Cu doping amount. However, Cu presents significant issues that limit this approach. Copper is a highly mobile dopant in CdTe [71] and can diffuse throughout the absorber, leading to instability and degradation of device performance over time. Excessive Cu can also create deep-level defects that act as recombination centers, counteracting its benefits by increasing nonradiative recombination [72]. Additionally, the solubility of Cu in bulk CdTe is limited, and much of the dopant tends to segregate at grain boundaries rather than uniformly doping the absorber [71, 73]. This segregation can create localized defect states and further promote recombination losses. Together, these challenges restrict the ability to optimize Cu doping to achieve the ideal band bending and stability necessary for high-performance in bifacial CdTe cells. Given these constraints, Cu-free CdTe bifacial devices have attracted increasing attention. We will look at some of these approaches in the next section.

Cu-free CdTe bifacial devices: While $CuGaO_x$/CGL grids demonstrated efficient bifacial performance, the reliance on copper remains problematic due to its high diffusivity, instability, and potential to form deep-level recombination centers. To address these limitations, Sartor et al. [70] presented an innovative hierarchical back contact design for Cu-free bifacial CdTe solar cells aimed at addressing critical challenges in band alignment, series resistance, and optical transparency. The absorber was based on Se-alloyed CdTe (CdSeTe), which narrows the bandgap

from ≈1.5 eV to below 1.4 eV. This enables absorption of longer-wavelength light while passivating grain boundaries and reducing mid-gap states, thereby extending carrier lifetimes. In addition, the authors employed arsenic (As) as a stable p-type dopant. Unlike Cu, which diffuses readily and induces instability, As provides higher and more uniform hole concentrations, promoting a stronger positive IFLO and upward band bending essential for bifacial operation [74].

The back contact was constructed as a hierarchical multilayer stack (Figure 9c).

$AlGaO_X$ passivating buffer: This reduced the barrier height at the CdSeTe interface (from 0.46–0.31 eV) (Figure 9e), improving $V_{OC}$ from 735 to 826 mV. However, the low conductivity of $AlGaO_X$ increased series resistance, reducing FF (75% to 70%).

$Ti_3C_2T_X$ MXene Interlayer: a high work-function (≈5.3 eV), highly conductive 2D material inserted between $AlGaO_X$ and Au back contact. This layer formed a transparent ohmic junction with $AlGaO_X$, restoring lateral conductivity and suppressing contact rollover (Figure 9g,h).

CFL-patterned Au nanogrids: deposited on top of the MXene interlayer to provide additional conducting pathways while maintaining transparency, building directly on the strategy pioneered by Muzillo et al. [69].

This modular architecture successfully combines the advantages of each component including $AlGaO_X$ for passivation and band alignment, MXene for low-resistance conduction, and CFL grids for optical/electrical balance. Under bifacial operation, the result was a front-side champion efficiency of 19.5% with FF = 81.5%, a rear-side efficiency of 2.9%, and a combined power density exceeding 200 $W/m^2$ under 10% rear illumination. The introduction of $Ti_3C_2T_X$ eliminated typical back-contact barriers as evidenced by the absence of rollover in J–V curves (Figure 9g). Nevertheless, EQE measurements revealed limited rear-side collection due to unpassivated defects, suggesting that back interface recombination persists (Figure 9i). Still, the hierarchical approach marks a significant step forward, as it not only avoids Cu-related instability issues but also demonstrates that transparent, low-resistance, and passivating back contacts can be engineered through a layered, modular structure.

Substrate Configuration CdTe Bifacial Devices: Despite the successes achieved in the superstrate configuration, it faces one significant limit. As technology increasingly moves toward flexible and wearable devices, the reliance of the superstrate configuration on rigid, transparent substrates become a significant drawback. This intrinsic requirement prevents its adaptation to flexible applications, limiting its relevance in next-generation electronics. In contrast, substrate configuration offers significant advantages where flexibility is desired, as it allows the use of lightweight polyimide or metal foils that are compatible with roll-to-roll processing [62]. Given the inherently rapid deposition of CdTe through deposition techniques such as closed-space sublimation (CSS), such an approach is expected to greatly enhance manufacturing throughput while simultaneously reducing production costs [75]. Additionally, the $CdCl_2$ treatment can be applied before CdS deposition, allowing the CdTe absorber to be exposed to higher annealing temperatures without risking intermixing or consumption of the CdS layer. High annealing temperatures promote grain growth, reduce grain boundary-to-bulk ratio, and improve junction quality. This provides greater control over heterojunction formation and interface properties compared with the superstrate configuration [76]. However, the reported efficiencies of substrate configurations CdTe fall short of those reported in superstrate configurations. Due to the high work function of CdTe, it tends to form a Schottky barrier with metal electrodes, as most metal electrodes do not have the high work function required to overcome this barrier; thus, buffer layers are often inserted [76]. A common issue observed in both superstrate and substrate configurations is the diffusion of Cu. This is even more severe in substrate configuration. In substrate configurations, Cu is typically introduced through the back contact, either via direct metallic Cu layers or Cu-containing buffers such as $CuCl_2$. While this approach enables convenient doping of CdTe, the high mobility of Cu makes it prone to excessive diffusion during subsequent high-temperature processing, such as $CdCl_2$ treatment. This uncontrolled diffusion can introduce deep-level defects, compromise adjacent layers, and ultimately lead to severe device degradation. Despite this, substrate configuration offers more potential for future applications.

Khanal et al. [77] demonstrated bifacial Cu-free CdTe solar cells in substrate configuration to address Schottky barrier issues in the back contact. A TEC-coated glass substrate (made up of an intrinsic $SnO_2$ layer and an F-doped $SnO_2$ layer (FTO)) was used with transparent single-wall carbon nanotube (SWCNT) incorporated as a back buffer between CdTe and back contact (TEC). This allowed front-side illumination (through CdS), and rear-side illumination (through SWCNT). CdTe (≈4.5 μm) and CdS (≈200 nm) were deposited by vapor transport deposition (VTD) at 570°C, followed by sputtered i-ZnO/AZO as the front TCO. Comparative analysis revealed a dramatic efficiency improvement from ≈1% for devices without SWCNT to ≈6.5% with the SWCNT interlayer in monofacial devices. Despite the performance improvement, barriers in the intrinsic $SnO_2$ layer of the TEC substrate still limited performance, showing significant band bending. To probe bifacial operation, the devices were illuminated from the rear-side through the TEC/SWCNT back-contact using CdS layers prepared by VTD and (CBD). The efficiencies were 0.78% and 1.76% for VTD and CBD CdS, respectively. The slight improvement in efficiency was attributed to reduced parasitic absorption by the CBD CdS layer and better conformality. Overall, the devices with SWCNT yielded a bifacial maximum power output of 5.9 $mW/cm^2$ with front and rear side efficiencies of ≈6.5% and ≈0.7%, respectively. Khanal et al.'s results reinforce the persistent challenges in substrate bifacial CdTe devices, while also highlighting the promise of innovative Cu-free designs for applications in flexible and tandem photovoltaics. A detailed comparison of the world record efficiencies of CdTe solar cells in monofacial and bifacial devices is presented in Table 3, including strategies.

### 2.2.2 | Challenges in CdTe Bifacial Devices

CdTe bifacial devices face persistent challenges at the back contact, which strongly influence rear-side performance. Achieving high-quality ohmic contact requires careful band alignment, but most transparent back contacts (e.g., ITO, IWO, TEC substrates)

**TABLE 3** | Summary of record efficiencies of monofacial and bifacial CdTe solar cells with respect to rear-side illumination.

| Device type | Back contact | Strategy | Efficiency (%) | $J_{SC}$ (mA/cm$^2$) | FF (%) | $V_{OC}$ (V) | Bifaciality factor ($\eta$) |
|---|---|---|---|---|---|---|---|
| Monofacial [78] | – | – | 23.1 | 31.66 | 80.6 | 0.9048 | – |
| Bifacial [68] | ITO | Interface engineering to enhance rear-side performance | Front: 12.5 | 22.2 | 70.8 | 0.796 | 0.60 |
| | | | Rear: 7.6 | 15.8 | 60.9 | 0.796 | |
| Bifacial [70] | CFL Au template | Hierarchical multilayer stack to improve front-side performance | Front:19.5 | 29.1 | 81.5 | 0.821 | 0.13 |
| | | | Rear: 2.6 | 4 | 79 | 0.797 | |

form barriers to hole collection due to insufficient work function relative to CdTe. These barriers increase recombination at the back interface, limiting rear-side current and overall bifacial efficiency. In several studies, this manifested as reduced fill factor, originally observed as J–V rollover. The key insight is that the back interface quality governs carrier extraction. Copper doping has traditionally been used to improve the p-type conductivity in CdTe and to also result in favorable band bending. However, a positive IFLO requires high Cu doping which creates a significant challenges, due to the high mobility of copper. Cu is known to diffuse during processing and can create deep-level defects, causing long-term instability. Another challenge arises in absorber thickness. Thinning the CdTe absorber improves rear-side absorption, while thicker absorbers benefit front illumination at the expense of rear-side efficiency. Substrate configurations, which are attractive for flexibility, add further complications, as they rely on transparent or conductive buffer layers that often introduce barriers or excessive recombination, and Cu diffusion is even harder to control during high-temperature treatments. Together, these factors have limited bifacial CdTe devices compared to their monofacial counterparts.

#### 2.2.3 | Future Aspects of CdTe Bifacial Devices

Future progress in bifacial CdTe photovoltaics will rely heavily on advanced back-contact engineering and Cu-free architecture. Hierarchical and multilayer back contact designs combining passivation layers, conductive interlayers, and patterned nanogrids represent a modular strategy to balance transparency, conductivity, and defect suppression. At the absorber level, alloying CdTe with Se (CdSeTe) and using stable dopants such as As offer pathways to achieve higher hole concentrations without Cu-induced instability, enabling more favorable band bending and long-term device reliability. Flexible substrate configurations are another exciting direction, as they open prospects for lightweight, roll-to-roll processed CdTe modules suited for building-integrated and portable photovoltaics, though efficiency gaps must still be closed. Finally, bifacial CdTe holds strong potential for tandem integration. To enhance the efficiency of tandem architectures, alloying CdTe with elements such as Se reduces its bandgap, making it suitable as a bottom cell when paired with wide-bandgap cells such as perovskite or CIGS. Leveraging CdTe in a bifacial configuration allows the device to absorb light not only from the front but also from the rear, enabling additional photocurrent generation from reflected or scattered light. This dual-side harvesting can further improve the power output and overall energy yield of tandem devices, providing a pathway for highly efficient bifacial tandem architectures in practical deployment scenarios (Figure 5).

### 2.3 | CZTS (S, Se) Solar Cells

Chalcogenide thin-film materials such as CIGS (Cu(In, Ga)$Se_2$) and CdTe have demonstrated significant progress in recent years, achieving Power Conversion Efficiencies (PCEs) exceeding 20% [79]. However, their scalability remains constrained by certain limitations, notably the scarcity of Indium and gallium in CIGS and the toxicity of cadmium in CdTe. To address these concerns, CZTS (S, Se) chalcogenides have emerged as potential replacements owing to the earth's abundance and nontoxicity of their constituent elements [80]. The amount of Cu, Zn, Sn, and S in Earth's crust is 68, 79, 2, and 420 ppm, respectively, significantly higher than those of indium (0.16 ppm) and cadmium (0.15 ppm) [81].

CZTS (S, Se) crystallizes in two primary crystalline structures, namely kesterite and stannite, with the former being thermodynamically favored [81, 82]. These materials exhibit favorable optoelectronic properties, including a high absorption coefficient ($>10^{-4}\,cm^{-1}$) and intrinsic p-type conductivity. Pure CZTS has a bandgap of ≈1.5 eV, which can be tuned by substituting S with Se to ≈1.0 eV [83]. Its alloy CZTSSe offers a tunable bandgap ranging from 1.0 to 1.5 eV, depending on the S/Se ratio [53]. Despite their favorable optoelectronic and material properties, the highest reported efficiencies of monofacial, single-junction CZTSSe (15.8%) [78], CZTSe (12.5%) [84], and CZTS (13.2%) [85] still fall short of those achieved by CIGS (>20%) and remain well below their SQ limits [86]. This efficiency limitation has been attributed to the severe $V_{OC}$ deficit [85], which arises from a range of factors,

including structural defects caused by large grain boundaries, bandgap tailing emanating from charge defects, as well as the formation of secondary phases. While strategies such as cation substitution, band grading, and deposition optimization have shown great promise [85], they are insufficient to fully overcome the intrinsic limitations of CZTS devices. Bifacial architecture, by contrast, offers a critical pathway toward closing this gap. By harvesting light from both the front and rear, bifacial CZTSSe devices can substantially increase photocurrent and overall maximum power without altering the absorber material itself. In thin-film bifacial solar cell applications, technologies today rely on CIGS and CdTe as best bifacial CIGS devices report front/rear efficiencies of ≈19.8%/10.9% [30], while bifacial CZTS on traditional TCO substrates still fall behind the CIGS counterparts. In this review, we explore the progress, challenges, and engineering strategies employed in CZTS-based bifacial devices, with emphasis on TCO selection, interfacial modifications, secondary phases, stability under real-world conditions, as well as potential for indoor light harvesting.

### 2.3.1 | Strategies for Performance Enhancement in Bifacial CZTS(S, Se) Solar Cells

Transparent conducting oxides (TCOs) serve as the front and rear electrodes in bifacial devices. Among these, ITO offers excellent conductivity and transparency. The very first report on bifacial Kesterite CZTS solar cells dates to 2014, when Ge et al. [87] introduced indium (In) substitution into the CZTS absorber (CZTIS) to mitigate Sn-related deep level defects. As described already, the efficiency of kesterite CZTS chalcogenides is constrained by the severe $V_{OC}$ deficit. A major contributing factor is defects related to Sn. These defects present deep transition levels with high capture-cross sections for electrons and holes, effectively acting as recombination centers, limiting $V_{OC}$ [88, 89]. Substitution of Sn with cations has proven to effectively reduce the deep levels, increasing minority carrier lifetime and improving device efficiency. Their device featured a bifacial architecture on ITO glass substrates, enabling illumination from both sides with a layer stack comprising Glass/ITO/CZTIS/CdS/i-ZnO/AZO (Figure 11a). Precursors were deposited by electroplating and sulfurized in a mixed Ar and $H_2S$ atmosphere at 520°C, producing Cu-poor, Zn, and Sn-slightly rich precursors (Cu/Zn = 1.8, Zn/Sn = 1.0, and S/metals = 0.2). SEM imaging revealed a bilayer absorber structure, with the upper layer consisting of well-defined grains and a bottom layer made up of particulates. Crucially, sulfurization at temperatures higher than 500°C induced an interfacial reaction degrading the ITO back contact via Indium out-diffusion into the absorber, reducing ITO conductivity and forming CZTIS. XRD revealed peak shifts from lattice expansion by In incorporation consistent with In partially substituting Sn (due to their similar atomic radii), along with the appearance of $SnS_2$ secondary phases and the disappearance of ITO peaks, indicating substrate degradation (Figure 11b). These compositional inhomogeneities, together with In interdiffusion, hindered Ohmic contact formation and severely reduced ITO conductivity.

Although In substitution stabilized the lattice against Sn multivalency, photoluminescence (PL) spectra revealed broad emissions centered at 1.10–1.13 eV with large band tails, reflecting persistent recombination. The fabricated devices showed a bifacial PCE of 3.4%, with front and rear-side efficiencies of 2.9% and 1.3%, respectively (Figure 11c). However, a high $V_{OC}$ deficit (≈1 V), large series resistance, and low fill factors were observed. The main bottleneck was the non-Ohmic back contact from ITO degradation during high-temperature sulfurization, outweighing the benefits of In substitution. To address these limitations, Ge et al. [91] explored sulfurization of Cu—Zn—Sn—S electroplated precursors in a tube furnace under sulfur vapor instead of $H_2S$. The milder environment preserved the ITO conductivity while enabling In diffusion into the CZTS lattice. Devices sulfurized at 540°C for 45 min and showed a front-side PCE of 5.8%, with $V_{OC}$ (0.555 V), $J_{SC}$ (16.7 mA/cm$^2$), and FF > 60%. Ge et al. further extended this strategy to CZTSSe devices on ITO [92] using selenium vapor as the chalcogen source. Selenization between 500°C and 550°C produced a typical bilayer and enhanced In diffusion into the upper layer. EDX and XRD confirmed partial substitution of Sn by In, while Sn segregated at the rear interface as $SnO_2$, particularly at higher temperatures. Unlike $H_2S$ sulfurization [87], the ITO substrate remained stable in Se vapor up to 550°C, consistent with the measured band gap (≈1.10 eV). The J–V curves showed a steady increase in bifacial performance with rising selenization temperature. Sn-related defects can be mitigated under Sn-poor conditions; thus, In substitution suppresses deep-level traps from multivalent Sn, reducing nonradiative recombination and enhancing p-type conductivity, thereby improving $V_{OC}$.

Achieving high-quality CZTS absorbers generally requires sulfurization/selenization at elevated temperatures, yet $H_2S$ atmospheres tend to degrade ITO substrates above 500°C due to their strongly reducing nature. These findings highlight that the sulfurization/selenization atmosphere is a critical parameter in bifacial CZTS (S, Se) device fabrication on ITO substrates. Reactive atmospheres like $H_2S$ can degrade ITO even at moderate temperatures via reduction and elemental interdiffusion, compromising rear contact quality. In contrast, selenium or sulfur vapor atmospheres allow for higher temperature processing with reduced ITO degradation, enabling Ohmic contact formation and improved $V_{OC}$. Therefore, optimizing both the selenization/sulfurization atmosphere and thermal profile is essential for achieving high-quality absorber layers while protecting the electrical properties of ITO.

Despite the widespread use of ITO due to its high conductivity, it presents significant challenges in bifacial CZTS devices, primarily because high-temperature sulfurization or selenization facilitates indium out-diffusion and deteriorates the substrate's conductivity [93] [94], while this Indium diffusion can enhance the p-type conductivity of the kesterite absorber itself [87, 95]. The loss of conductivity in ITO impairs device efficiency and overall stability in bifacial configurations where dual-side electrical and optical performance is critical. Given these drawbacks, alternative TCOs such as FTO have been explored. Although FTO generally exhibits lower conductivity than ITO, it is less expensive and offers superior thermal stability under elevated processing temperatures necessary for CZTS sulfurization or selenization [96]. Kim et al. compared CZTSe absorbers on FTO and ITO using sputtered Cu-Sn-Zn precursors and a two-step selenization in a bifacial (glass /FTO(ITO) /CZTSe /CdS /i-ZnO /AZO / Al-grid) configuration [97]. SEM imaging showed uniform films on FTO, but voids on ITO. On ITO, In diffused into the absorber, while Sn migrated to the interface, forming a $SnO_2$ layer that

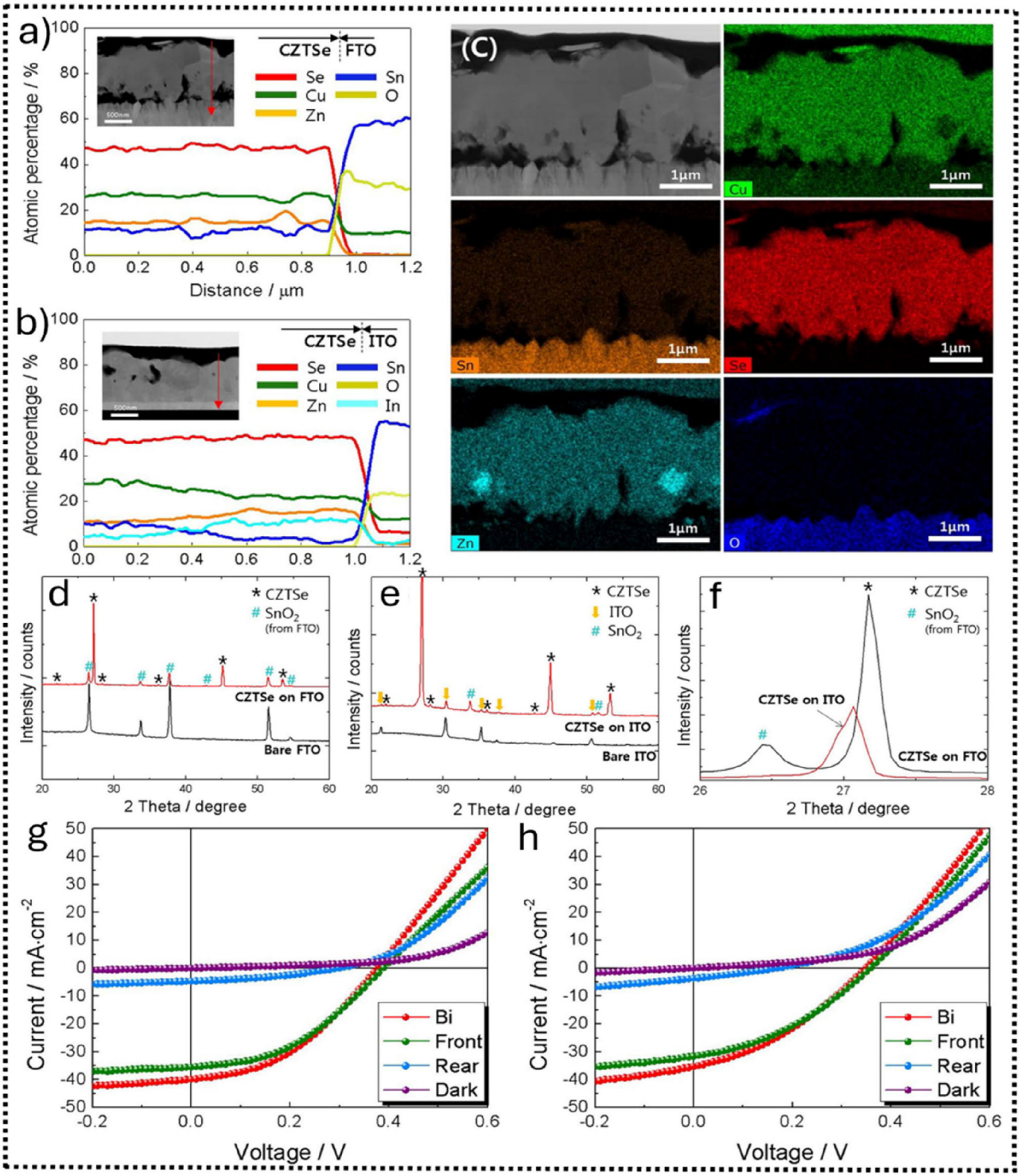


**FIGURE 10** | (a and b) STEM-EDS line scans of CZTSe on FTO and ITO, respectively. (c) STEM-EDS mapping of CZTSe on FTO. (d and e) XRD patterns of CZTSe on FTO and ITO. (f) magnified XRD peaks highlighting $SnO_2$ formation on FTO and ITO. (g and h) J–V curves of bifacial CZTSe on FTO and ITO. Reproduced with permission [97]. Copyright 2016, AIP Publishing.

improved adhesion but reduced conductivity (Figure 10a–c). On FTO, no In diffusion occurred, though $SnO_2$ was still detected by XRD and STEM-EDS (Figure 10d–f). Under bifacial illumination, FTO-based devices achieved higher PCE (6.05%; front, 5.72%; rear, 0.51%) than ITO-based devices (4.72%; front, 4.12%; rear, 0.51%) (Figure 10g,h). The reduced efficiency on ITO was linked to Sn–In interdiffusion and TCO degradation, emphasizing the need to control elemental diffusion and suppress $SnO_2$ formation at the absorber/TCO interface.

Interface Engineering of Bifacial Kesterite on ITO/FTO substrates: In bifacial CZTS (S, Se) solar cells fabricated on ITO or FTO substrates, a key challenge lies in controlling elemental interdiffusion at the absorber/TCO interface during high-

temperature chalcogenization. Diffusion of species such as Sn and In can affect TCO conductivity, often leading to non-Ohmic contacts and severe $V_{OC}$ losses. Unlike Mo-based electrodes that form beneficial Mo(S, $Se_2$) interfacial layers, realizing ohmic contact is challenging to achieve on TCO-based substrates. As such, interfacial engineering plays a key role in not only suppressing elemental interdiffusion but also enhancing ohmic contact at the rear interface. Kim et al. introduced a metallic molybdenum (Mo) interlayer between ITO and CZTSe absorber [90]. By inserting a 20 nm Mo layer, bifacial power output improved markedly from 0.7 to 5.71 mW/$cm^2$ (front, 1.0 sun; rear, 0.3 sun) (Figure 11h). The Mo interlayer, after selenization, formed a MoSe phase whose thickness increased with Mo layer. This interlayer effectively suppressed Sn-In diffusion; notably, no indium was detectable in absorbers coated with 80 nm Mo (Figure 11g). However, thicker Mo layers caused overgrowth of the MoSe layer, which negatively affected ohmic contact and reduced efficiency in those samples. While the Mo interlayer suppressed Sn–In diffusion and helped form a MoSe contact layer, the overall rear-side efficiency remained limited, which led to reduced bifacial power output relative to state-of-the-art CZTSe solar cells.

Another significant challenge arises in FTO substrates for kesterite absorbers: the inhibition of sodium (Na) diffusion due to FTO's dense film structure. The diffusion of Na into the kesterite absorber is particularly important to the crystal growth of kesterite absorbers. Na can increase the grain Ag doping has been employed size of absorbers, leading to a reduction in grain boundary recombination, which is a dominant nonradiative recombination mechanism limiting device performance [98–100]. The impeded Na diffusion affects absorber crystallinity and grain size optimization, necessitating meticulous interface engineering. Recently, Sawa et al. [101] incorporated Sodium via NaF deposition on FTO substrates, enhancing grain growth and CZTS crystallinity, while a tungsten (W) interlayer improved back contact by forming conductive $WS_2$. GIXRD of the absorber deposited on only FTO revealed the presence of $SnS_2$ secondary phase (Figure 12e). The $SnS_2$ secondary phase is highly detrimental to the performance of kesterite devices. However, in the

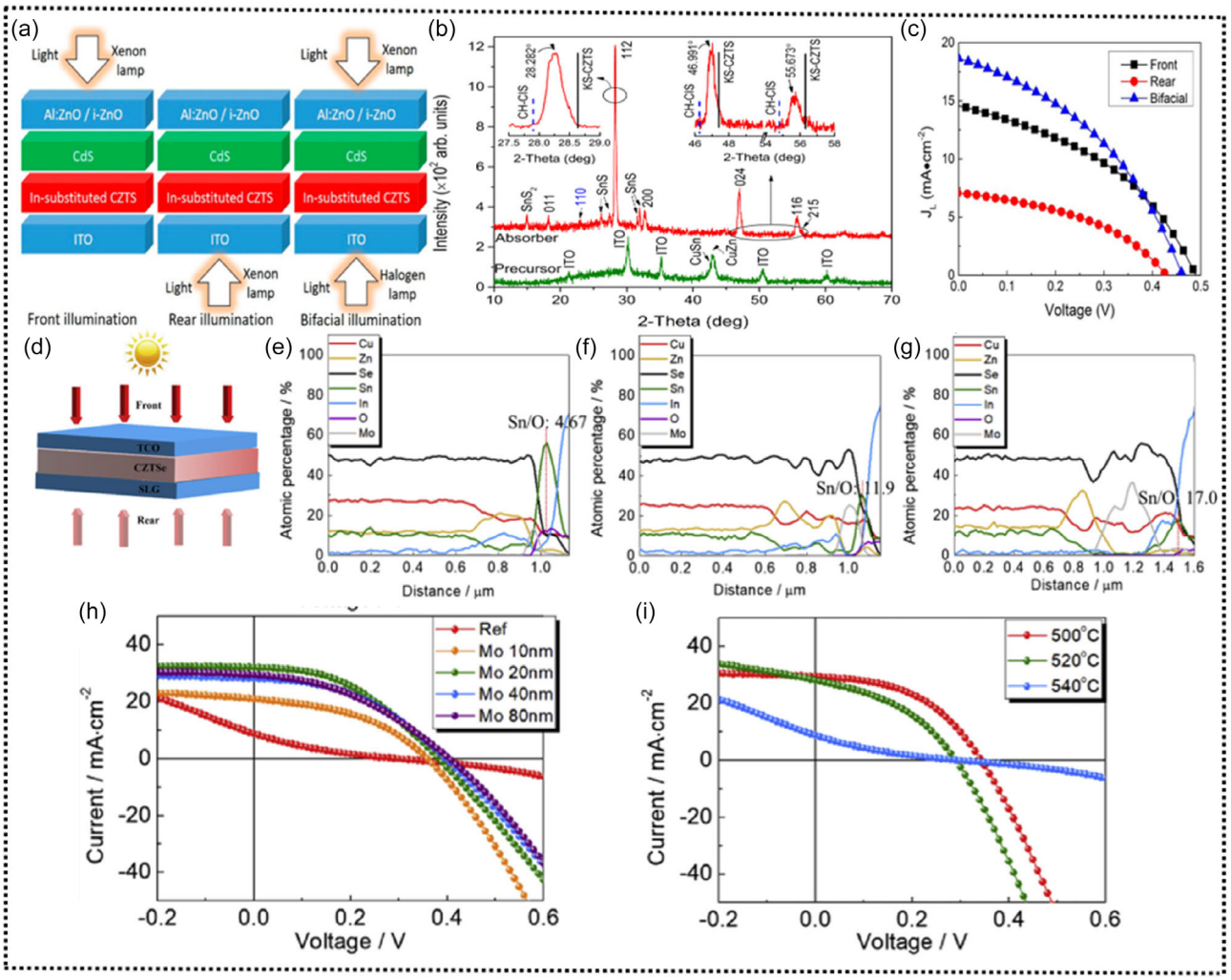


**FIGURE 11** | (a) Schematic illustration of front, rear and bifacial illumination. (b) J–V curves under different illumination conditions. (c) XRD patterns highlighting $SnS_2$ secondary phase formation from partial In substitution: Insets show lattice expansion from In incorporation. (d) Conceptual representation of bifacial CZTSe architecture. (e–g) STEM-EDS line scans for Mo interlayers with thickness of 10, 20, and 80 nm, respectively. (h) J–V curves as a function of different Mo interlayer thickness (f) J–V curves as a function of selenization temperature. (a–c) are reproduced with permission [87] copyright 2014, American chemical society (d–i) are reproduced with permission [90] copyright 2018, Elsevier.

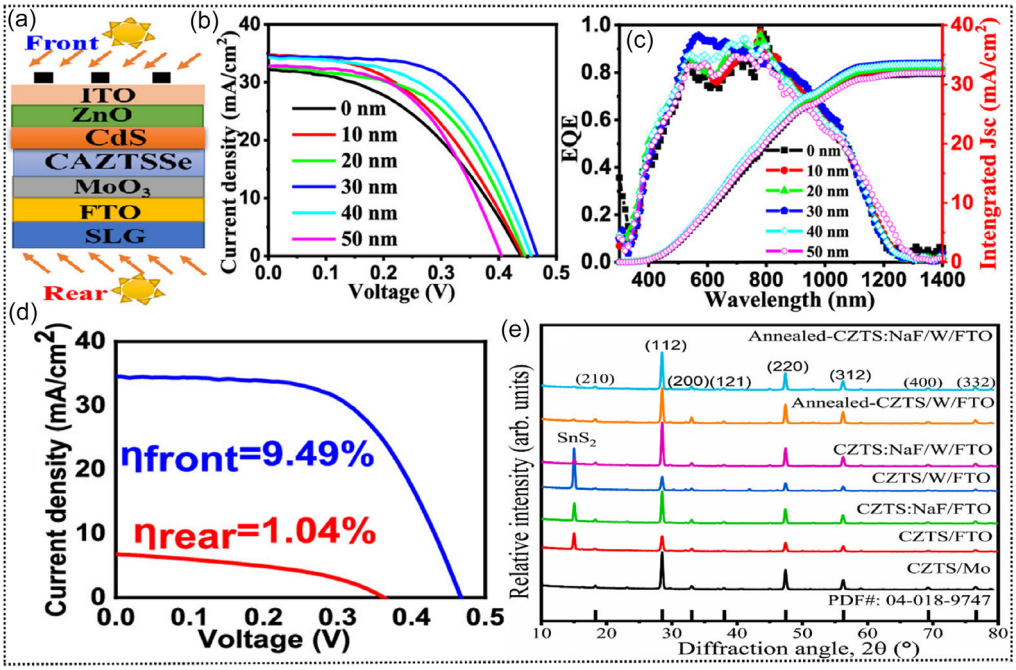


**FIGURE 12** | (a) Schematics of bifacial CAZTSSe. (b) J–V and (c) EQE curves of 0–50 nm Mo interlayers. (d) J–V curve of champion CAZTSSe device with 30 nm Mo interlayer. (e) GIXRD spectra of CZTS absorbers with and without Na incorporation on different substrate configurations. (a–d) are reproduced with permission [102], Copyright 2024, American Chemical Society, and (e) is reproduced with permission [101] Copyright 2024, Elsevier.

air annealed samples with the W interlayer and Na incorporation, the $SnS_2$ phase was suppressed (Figure 12e). Furthermore, the W interlayer improved FTO's Ohmic contact with the absorber, a major bottleneck in bifacial kesterite solar cells. The optimized architecture ($FTO/WS_2 + Na + air$-anneal) achieved a front side PCE of 5.2% ($J_{SC} = 15.4\ mA/cm^2$, $V_{OC} = 0.7$ V, FF = 47.7%), significantly outperforming the Mo reference (2.7% PCE).

Building on interface engineering, Chen et al. spin-coated $MoO_3$ interfacial layer onto FTO-coated glass substrates [102]. By optimizing the thickness of the $MoO_3$ layer, significant enhancements in device performance were achieved. In this study, CAZTSSe absorbers were used. The utilization of Ag can be beneficial to both the optoelectronic properties as well as the quality of the absorber layer. Ag doping has been employed to suppress the formation of secondary phases and harmful defect clusters, thereby decreasing bulk recombination [103], which was confirmed by XRD. Without the $MoO_3$ layer, the front-side efficiency was 6.17%. As $MoO_3$ was introduced with varying thicknesses between 10 and 50 nm, the efficiency increased up to a 30 nm $MoO_3$ layer, which decreased at higher thicknesses (Figure 12b). For the optimum condition (30 nm), efficiency reached 9.49% with a $J_{SC}$ of 34.51 $mA/cm^2$, $V_{OC}$ of 0.467 V, and a FF of 58.53% (Figure 12d). This efficiency improvement was attributed to the better CAZTSSe/FTO interface with the $MoO_3$ interfacial layer, as well as improved photoelectric response. The rear side efficiency was only 1%, limited by the inefficient current generation within the particulates/fine-grained bottom layer. IVT analysis was used to investigate the activation energy to understand the recombination mechanism of the champion device (30 nm $MoO_3$). Since the $E_a$ (0.9 eV) was close to the $E_g$ (1.06 eV), the interface recombination [104, 105] at the CAZTSSe/FTO interface was passivated by the introduction of $MoO_3$, corroborated by the improvements in $V_{OC}$ and FF. The front side efficiency of 9.49% represents the highest reported in kesterite bifacial devices (Figure 12d).

Rear-Side Illumination Challenges and the Role of Kesterite/TCO Interface: Rear-side efficiency in bifacial kesterite solar cells is notably lower than the front side. The poor performance observed under rear-side illumination in bifacial CZTS (S, Se) solar cells arises from a combination of optical, electronic, and structural limitations. A key issue is that light entering from the rear does not reach the CdS junction, placing critical emphasis on the TCO/absorber interface for charge separation. However, this interface suffers from poor band alignment, leading to Schottky barrier formation that impedes carrier transport. AMPS-1D simulations have shown that barrier heights above 0.4 eV drastically reduce rear-side efficiency below 2%, underscoring the need for high work function TCOs or interfacial engineering to lower the barrier [106]. Additionally, the absorber layer in most CZTS(S, Se) devices exhibits a bilayer morphology comprising a well-crystalline upper layer and a bottom layer of fine particulates. This bottom region, which is first illuminated under rear-side illumination, typically exhibits high defect densities, compositional inhomogeneities such as secondary phase segregation, and poor electronic quality. Due to its short depletion width and low minority carrier diffusion length, carriers recombine before they are collected. Furthermore, high-temperature sulfurization or selenization, necessary for good absorber quality, often degrades TCO substrates like ITO through elemental interdiffusion (Sn-In) and the formation of insulating interfacial layers. These changes degrade TCO conductivity, affecting ohmic contact, particularly at the rear interface, compounding current losses under rear illumination.

Limitations of ITO and FTO Substrates for Bifacial Architectures: Despite the advantages of ITO as a substrate, particularly its high

conductivity, the use of ITO as a substrate poses significant threats to the efficiency of bifacial CZTS (S, Se) devices due to Indium out-diffusion and conductivity degradation under high sulfurization/selenization temperatures. While insertion of interlayers (Mo, W, $MoO_3$) can suppress such effects, it often introduces additional complexity, as optimization of such layers requires optimization of other layers. Though an increase in the thickness of these interlayers can completely prevent elemental interdiffusion, this inhibits ohmic contact and reduces efficiency. Even with FTO, improved thermal stability comes at the expense of conductivity. The deposition of bifacial devices on rigid glass substrates limits the scalability and application of bifacial devices. Additionally, the deposition of CZTS bifacial devices on FTO or ITO substrates induces the formation of secondary phases, which affect device performance. Moreover, the heterojunction qualities at the interfaces are not the same, which leads to significant differences in efficiency. These persistent issues strongly motivate the move towards flexible, double-sided conductive substrates such as Mo foil, which offer thermal stability, compatibility with double-sided processing, and the potential for truly symmetrical, high-performance bifacial architectures.

Flexible CZTS (S, Se) Bifacial Architectures: Indoor light is highly diffused and scattered, coming from all directions due to reflection off walls, ceilings, and surfaces. Bifacial solar cells capture energy from both their front and rear sides, enabling them to utilize more of this multidirectional light than traditional single-sided cells. Flexible substrates further enhance this advantage by offering mechanical flexibility, allowing the cells to conform to curved, irregular, or nonflat indoor surfaces where light angles vary widely. Unlike the traditional TCO glass substrates that limit device placement and reduce effective light capture, flexible substrates enable versatile integration and improved photon absorption from any direction. Together, bifacial architecture on such flexible substrates maximizes indoor energy harvesting by effectively using omnidirectional light, which is not possible with traditional TCO substrates. Deng et al. first reported bifacial CZTSSe on flexible substrates, typically Mo foil substrates for indoor photovoltaic applications [107]. The use of Mo foil as a substrate presents flexibility, excellent thermal stability, as well as double-sided conductivity, making it possible to achieve the same interface quality at both sides. Deng et al. showed that solution-processed CZTSSe absorbers could be deposited symmetrically on both sides of Mo foil. The device stack with double-sided deposition was (Ag/ITO/i-ZnO/CdS/CZTSSe/MoSe/Mo foil/MoSe/CZTSSe/CdS/i-ZnO//ITO/Ag) as shown in Figure 13a. XRD revealed all peaks consistent with pure CZTSSe without any impurity or secondary phases except for Mo and $MoSe_2$ (Figure 13b). SEM imaging showed similar morphology on both sides of the Mo foil with similar thicknesses (Figure 13c–g). The highest efficiency for the front side was 9.3% with a $J_{SC}$ of 33.76 mA/cm$^2$, A $V_{OC}$ of 0.436 V, and a FF of 63.2% (Figure 13i). Comparatively, the rear side reached 9% PCE, highlighting the effectiveness of the double-sided conductivity of the Mo foil. Their work demonstrated not only the feasibility of simultaneous double-sided deposition but also strong operational stability under low-intensity indoor LED illumination and mechanical resistance up to 3000 bending cycles, which is critical for real-world flexible applications (Figure 13k–m). Liu et al. [108] extended this concept using electrodeposited

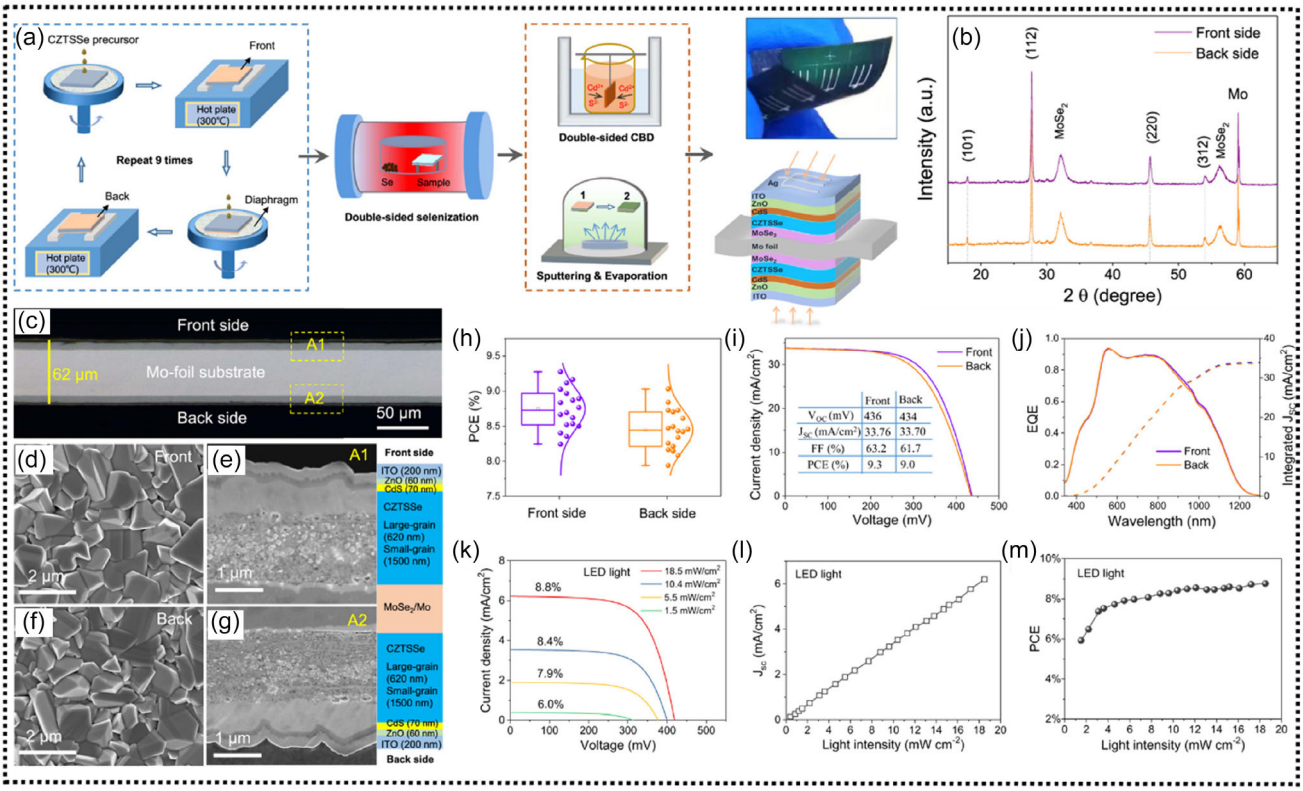


**FIGURE 13** | (a) Schematic of symmetrical CZTSSe deposition on Mo foil substrates. (b) XRD and (c–g) SEM showing uniform double-sided CZTSSe deposition (h) PCE box plots (i) J–V and (j) EQE curves of front and back-side illumination. (k–m) J–V, $J_{SC}$ dependent, curves (l) and PCE-dependent performance under varying LED light intensities. Reproduced with permission [107], Copyright 2021, Springer Nature.

precursors combined with high-temperature selenization. Note that, for traditional ITO substrates, to mitigate the interdiffusion of elements, sulfurization/selenization is kept at ≈500°C [109]. High sulfurization/selenization temperatures aid good kesterite material. Owing to the much higher thermal stability of Mo foil, they were able to selenize the precursors at an elevated temperature. Their bifacial CZTSe devices reached efficiencies of 6.43% (front) and 6.20% (rear), and after 3000 bending cycles, they retained ≈90% of the initial performance, confirming strong adhesion between the absorber and substrate. Like Deng's work, they demonstrated the practical utility of Mo foil's double-sided conductivity, achieving parallel front–rear operation that enhanced total power generation under multidirectional light. However, both works reported persistent low $V_{OC}$ values, with Liu explicitly attributing the loss to interfacial recombination at the CdS/CZTSe junction, as revealed by temperature-dependent J–V analysis. This pinpoints junction engineering as a critical next step for further efficiency gains in flexible bifacial kesterite devices. Together, the studies by Deng et al. and Liu et al. underscore the unique advantages of Mo foil as a flexible and bifacial compatible substrate for kesterite devices. A detailed comparison of the record efficiencies of CZTS (Se, S) solar cells in monofacial and bifacial devices is presented in Table 4, including strategies & configurations.

#### 2.3.2 | Challenges in CZTS (S, Se) Bifacial Devices

Bifacial CZTS (S, Se) solar cells have shown considerable promise due to their potential for light harvesting, making them suitable for flexible, indoor, and low-light applications. Despite this, several challenges persist. Interface engineering remains a key hurdle, as secondary phases such as $SnS_2$, $SnO_2$ can form at the absorber/back-contact interface, increasing series resistance and limiting device performance. Furthermore, high-temperature processing required for high-quality kesterite layers can also induce interdiffusion and degradation of $TCO_S$, affecting ohmic behavior and device stability. Back-contact optimization continues to be critical; achieving stable quasi-ohmic contacts while suppressing Sn–In or other interfacial diffusion is essential for maintaining bifacial performance. Light absorption under weak or multidirectional illumination is another challenge, particularly for indoor applications, where reduced photon flux can limit $J_{SC}$ and $V_{OC}$. For flexible substrates, mechanical stress and bending stability must also be addressed to retain long-term bifacial performance.

#### 2.3.3 | Future Aspects of CZTS (S, Se) Bifacial Devices

Optimizing the CdS/CZTS (S, Se) interface remains paramount, with emerging strategies such as buffer layer engineering and doping showing promise. Though this has been utilized in

**TABLE 4** | Summary of the significant monofacial and bifacial CZTS (S, Se) chalcogenide efficiencies on various substrate types.

| Type | Substrate type | Absorber | Strategy | Eff (%) | $J_{SC}$ (mA/cm$^2$) | FF (%) | $V_{OC}$ (V) | Group |
|---|---|---|---|---|---|---|---|---|
| Monofacial | Mo substrate (Rigid) | CZTS [85] | Cd alloying | 13.2 | 24.74 | 73.64 | 0.72 | UCAS |
| Monofacial | Mo substrate (Rigid) | CZTSe [84] | Defect passivation | 12.5 | 37.3 | 68.1 | 0.49 | UNSW |
| Monofacial | | CZTSSe [78] | – | 15.8 | 38.1 | 74.7 | 0.55 | IoP/CAS |
| Bifacial | ITO-coated glass (rigid) | CZTS [91] | Sulfurizing atmosphere control | Front: 5.8 | 16.6 | 62.6 | 0.55 | UToledo |
| | | | | Rear: 0.70 | 2.79 | 53.7 | 0.46 | |
| Bifacial | FTO-coated glass (rigid) | CZTSe [97] | In-Sn diffusion suppression | Front: 5.72 | 35.0 | 42.0 | 0.38 | DGIST |
| | | | | Rear: 0.51 | 4.7 | 36.4 | 0.30 | |
| Bifacial | Mo foil (flexible) | CZTSe [108] | Symmetrical deposition | Front: 6.43 | 32.6 | 51.7 | 0.38 | HENU |
| | | | | Rear: 6.20 | 33.3 | 49.8 | 0.37 | |
| Bifacial | FTO-coated glass (rigid) | CZTSSe [102] | Interface engineering using $MoO_3$ | Front: 9.49 | 34.5 | 58.8 | 0.46 | GXU |
| | | | | Rear: 1.04 | 6.8 | 40.0 | 0.36 | |
| Bifacial | Mo foil (flexible) | CZTSSe [107] | Symmetrical deposition | Front: 9.3 | 33.7 | 63.2 | 0.43 | FZU |
| | | | | Rear: 9.0 | 33.7 | 61.7 | 0.43 | |

monofacial configurations, it can be extended to bifacial configurations. Recently, Ma et al. doped CdS with $Al^{3+}$ in monofacial CZTSSe improving the device efficiency from ≈6.6% to ≈9% [110]. The performance improvement was attributed to improved heterojunction quality at the CdS/CZTSSe junction allowing for better electron extraction due to favorable band alignment and reduced carrier recombination. This approach could mitigate interfacial recombination losses, enhancing both front and rear-side efficiencies. Beyond interfacial improvements, precise control of absorber composition and elemental diffusion remains critical. Advanced deposition techniques, thermally stable substrates, and controlled doping strategies are essential to further enhance crystallinity, carrier lifetimes, and bifacial performance. Doping with elements such as Ag, Na, or K [111, 112] demonstrably improves absorber crystallinity which could lower the required sulfurization/selenization temperatures, and thereby mitigates TCO degradation and preserves conductivity. Mechanically robust substrates, coupled with scalable deposition and interface engineering will be essential for translating bifacial kesterite technology from laboratory demonstrations to practical applications, including indoor, low-light, and flexible photovoltaics, bridging the gap between monofacial and bifacial devices. The tunable bandgap of CZTS (S, Se) absorbers makes them highly suitable for tandem devices. Wide-bandgap CZTS (≈1.5 eV) is ideal as a top cell, efficiently absorbing high-energy photons while allowing lower-energy photons to transmit to the bottom cell. Narrow bandgap CZTSe (≈1.0 eV) can serve as an effective bottom cell, capturing the transmitted photons and maximizing overall current. This tunability enables current matching in 2-terminal (2T) tandems and independent optimization in 4-terminal (4T) tandems. Incorporation of CZTS (S, Se) in tandem architecture provides an exciting avenue to overcome the intrinsic efficiency limitations of single-junction devices. Advancing beyond conventional tandem approaches, bifacial tandem CZTS solar cells hold the additional advantage of capturing albedo and diffuse light from the rear side, enabling higher energy yields under real-world operating conditions (Figure 5). This dual approach not only enhances overall efficiency but also strengthens the competitiveness of CZTS as a sustainable, earth-abundant absorber material for next-generation photovoltaics.

### 2.4 | Antimony (Sb) Chalcogenides ($Sb_2Se_3$, $Sb_2S_3$, $Sb_2(S, Se)_3$)

Antimony (Sb) chalcogenides, comprising $Sb_2Se_3$, $Sb_2S_3$, and $Sb_2(S, Se)_3$, have attracted significant attention as a promising absorber material for thin film photovoltaics due to their earth abundance, nontoxicity, and suitable bandgap (1.1–1.7 eV). Unlike isotropic 3D semiconductors such as CdTe or CIGS, Sb-chalcogenides crystallize in a 1D ribbon-like structure composed of $[Sb_4X_6]_n$ (X═S, Se) units bound by weak van der Waals forces. This results in strongly anisotropic electrical and optical properties, where carrier transport is strongly dependent on grain orientation. Sb chalcogenides typically crystallize in three orientations: hk0 and hk1 and 002 which we have described in later sections. Consequently, orientation control is central to high-efficiency device design.

Similarly, with CdTe, two device architectures have been pursued: superstrate configuration (glass/TCO/CdS/$Sb_2Se_3$, $Sb_2S_3$, $Sb_2(S, Se)_3$/metal), where the Sb-based absorber is deposited directly on CdS, and substrate configuration (glass/Mo/$Sb_2Se_3$, $Sb_2S_3$, $Sb_2(S, Se)_3$/CdS/TCO/metal grid), where it is grown directly on the back contact [113]. Despite the differences in device architectures, $Sb_2Se_3$ solar cells have achieved comparable efficiencies in both substrate and superstrate configurations, demonstrating the viability of either approach. Reported efficiencies for substrate devices exceed 10% [114–116] while the best superstrate devices reach 10.57% [117]. In contrast, $Sb_2S_3$ and $Sb_2(S, Se)_3$ exhibit a stronger dependence on configuration: $Sb_2S_3$ performs better in superstrate configuration with efficiencies surpassing 8% [118, 119] and $Sb_2(S, Se)_3$ reaching 10.75% [120].

Although Sb chalcogenides have shown steady progress, their efficiencies remain far below their Shockley–Queisser (SQ) limits [11], primarily due to a large open circuit voltage ($V_{OC}$) deficit. This deficit is defined as $\frac{E_g}{q} - V_{OC}$, (where $E_g$ is the bandgap of the absorber and q is the elementary charge) and quantifies the gap between the theoretical maximum and the measured $V_{OC}$. For $Sb_2Se_3$, the best device shows a $V_{OC}$ deficit of ≈0.5 V [117], while most $Sb_2Se_3$ cells exhibit ≈0.7 V. Even larger values are observed for $Sb_2S_3$ (≈1 V) and $Sb_2(S, Se)_3$ (≈0.9 V). These losses are significantly higher than those of CIGS (≈0.3 V), CdTe (0.6 V), and CZTSSe (0.62 V), and much greater than the SQ-predicted limits for absorbers with bandgaps between 1 and 1.7 eV [121]. This voltage loss represents a major bottleneck for Sb chalcogenides.

The origin of this deficit lies in non-ideal band alignment at heterointerfaces and the presence of deep defect states. Intrinsic defects can be categorized as vacancies ($V_{sb}$, $V_s$/$V_{se}$), interstitials ($Se_i$, $S_i$), and antisite defects ($Se_{sb}$, $S_{sb}$, $Sb_{Se}$, $Sb_S$). Among these, vacancies and interstitials typically have low formation energies, leading to the creation of midgap states. These act as traps for charge carriers, promoting nonradiative recombination and ultimately driving the large $V_{OC}$ deficit observed in Sb-based devices [122]. These persistent limitations motivate the exploration of new strategies to enhance carrier collection and reduce recombination losses. Bifacial architecture offers a unique opportunity to harvest light from both sides. Understanding how orientation, substrate choice, and interface engineering affect carrier transport in such configurations will be key to advancing future bifacial Sb research.

Bifacial Sb Chalcogenides: Ongoing research efforts in Sb chalcogenides are geared towards improving the efficiency of monofacial devices, as current efficiencies are lower than those of CIGS, CdTe, and CZTS. Thus, there is very little report on bifacial work. Lee et al. [123] modeled bifacial Ge-incorporated $Sb_2Se_3$ devices on transparent electrodes with a back buffer using SCAPS and MATLAB. They showed that band alignment at the absorber/back buffer interface is critical for efficient hole extraction: A flat or slightly positive valence band offset (VBO) facilitates hole transport, while a negative conduction band offset (CBO) repels electrons and reduces recombination. Their simulations demonstrated that higher buffer (HTL) doping improves performance by lowering hole barriers, and lower absorber doping under optimized buffer conditions further enhances efficiency. Bifacial analysis indicated that increasing absorber thickness benefits front-side efficiency but can reduce

rear-side performance, whereas thinner absorbers favor the rear side. Optimized parameters suggested a moderate absorber doping and back-buffer (HTL) configuration, yielding high modeled front and rear-side efficiencies. While this study relies on modeling, the results offer valuable guidance for understanding the impact of band alignment, doping, and absorber thickness on bifacial $Sb_2Se_3$ solar cell performance.

### 2.4.1 | Strategies for Enhancement Performance of Bifacial Sb-Based Solar Cells

Substrate-Dependent Orientation Effects on Bifacial Sb Chalcogenides: In bifacial devices, carrier transport plays an even more critical role than in conventional monofacial cells. Since photogeneration occurs from both the front and rear sides, carriers are generated at varying depths within the absorber. Efficient transport is therefore essential to ensure that these carriers reach the junction before recombining. For highly symmetric, 3D semiconductors like CdTe, crystal orientation is generally not a major concern since their properties are nearly isotropic. Even with CIGS, though with less symmetry due to its chalcopyrite tetragonal structure is still relatively isotropic in terms of optical/electrical transport. In contrast, $Sb_2Se_3$ possesses a 1D crystal structure giving rise to pronounced anisotropy in both electrical and optical properties. Charge carriers move between neighboring $[Sb_4Se_6]_n$ ribbons primarily through hopping, which can limit mobility. As a result, crystal orientation control is crucial in Sb chalcogenide solar cells. Although most studies reporting the impact of orientation on carrier transport are performed on monofacial devices, the same principles should apply to bifacial devices: Carriers generated at the rear interface must travel farther to be collected, making orientation effects even more pronounced. Sb chalcogenides crystallize in three primary orientations: hk0, hk1, and 002 (Figure 14a–h).

**hk0**: The hk0 orientations lie parallel to the c-axis (ribbon direction) and consequently, parallel to the substrate surface (Figure 14h). These orientations are thermodynamically favored and frequently dominate in thin films [125, 126]. Along the [hk0] orientations, carriers must hop between adjacent ribbons, termed as interchain or interlayer hopping [127, 128], resulting in poor transport and increased recombination. Due to this, carrier transport along the hk0 orientations is very poor, leading to significant recombination losses [129]. In bifacial devices, hk0-dominated

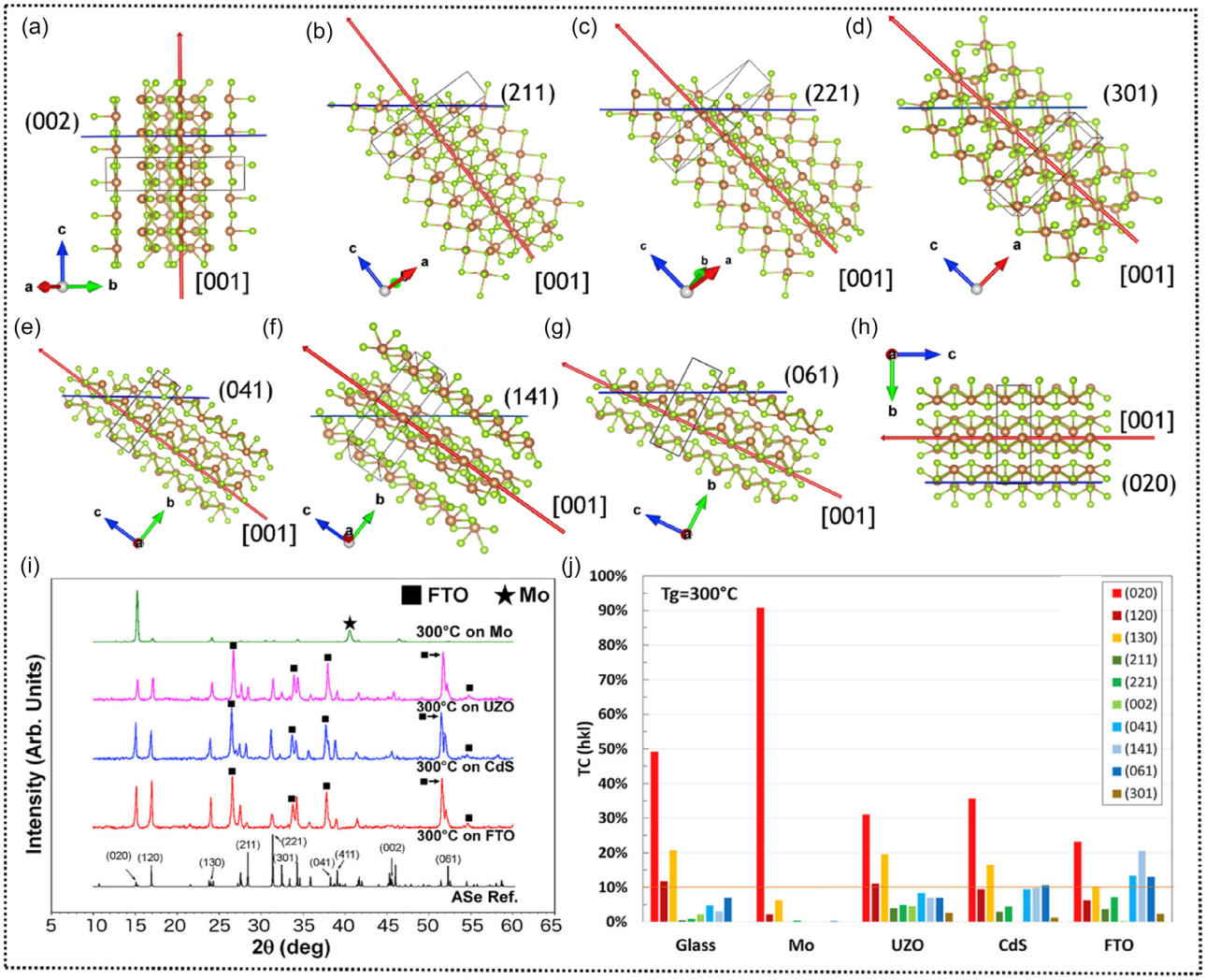


**FIGURE 14** | (a–h) Graphical representations of selected crystallographic orientations of $(Sb_4Se_6)n$ ribbons. (i) XRD patterns of $Sb_2Se_3$ on different substrates. (j) Texture coefficient values of $Sb_2Se_3$ on different substrates. Reproduced with permission [124]. Copyright 2020, Elsevier.

growth further reduces collection efficiency for carriers generated near the rear interface. Minimizing the hk0-oriented planes is therefore beneficial for bifacial solar cell performance.

**hk1:** The hk1 orientations are tilted with respect to the c-axis (ribbon direction), leading to vertical orientation of the $Sb_4X_6$ (X═S or Se) ribbons (Figure 14b–g). This facilitates more direct (1D) intraribbon movement, improving carrier mobility and reducing recombination losses [129–131].

**002**: This orientation aligns its 1D crystal chains perpendicular to the substrate, offering a direct path for efficient charge transport and improved interfacial properties (Figure 14a). The diffusion length along [002] has been measured at ≈1.7 μm compared with ≈0.29 μm along the [221] direction [130]. Longer diffusion lengths mean photo-generated carriers can travel a longer distance in the absorber material before recombining. This is particularly important in bifacial devices, as carriers can be generated from both front and rear illumination and must travel effectively regardless of where they are generated. Achieving [002] orientation is challenging due to its higher surface energy [130]; however, careful growth conditions can promote preferential alignment, which is critical for efficient bifacial performance. A detailed comparison of different crystallographic orientations and their respective effective vertical component (EVC) values is shown in Table 5.

As with CdTe, $Sb_2Se_3$ can be deposited in both substrate and superstrate configurations. For potential bifacial applications, the substrate configuration would mean depositing directly on a transparent conducting oxide (TCO) such as ITO, FTO, etc. Conversely, in superstrate consideration, the $Sb_2Se_3$ would be deposited on top of the CdS (ETL) layer as shown in Figure 15a,b.

The orientation of Sb chalcogenides strongly depends on the substrate type and its morphology. Zhou et al. [132] fabricated $Sb_2Se_3$ on ITO, FTO, and BZO. XRD and texture coefficient (TC) analysis were used to assess the preferred growth directions. Films on ITO were dominated by small-angled hk1 planes, yielding poor carrier transport, while films on FTO exhibited large-angled hk1 planes, improving transport relative to ITO. BZO substrates promoted highly oriented [002] films with optimal transport but introduced voids between grains, likely increasing recombination (Figure 16a–c). The difference in growth orientations for the $Sb_2Se_3$ film was ascribed to the different surface morphologies of ITO, FTO, and BZO. Whereas ITO exhibited a smoother morphology, FTO and BZO were rougher, thereby allowing for vertical growth of $Sb_2Se_3$. As a compromise between orientation and compactness, FTO was selected for subsequent studies. In the superstrate configuration, $Sb_2Se_3$ is deposited directly on CdS; thus, controlling the crystal growth is essential. Guo et al. [133] fabricated $Sb_2Se_3$ superstrate devices and tuned grain orientation via CSS deposition. Films dominated by (211) orientation achieved ≈4.2% efficiency, outperforming (221) oriented films (≈3.9%), due to near vertical growth of (211) planes, which improved $J_{SC}$ and $V_{OC}$. In contrast, (120)-oriented films showed poor carrier transport along the ribbons, higher series resistance, and lower efficiency (≈2.9).

**TABLE 5** | Crystallographic orientation and effective vertical component (EVC) of $Sb_2Se_3$ ribbons.

| Crystallographic orientation | Angle between ribbons and the surface normal (°) | Effective vertical component (EVC) |
|---|---|---|
| (002)[a] | 0 | 1 |
| (211) | 37.3 | 0.79 |
| (221) | 43.8 | 0.72 |
| (301) | 45.7 | 0.70 |
| (041) | 53.4 | 0.60 |
| (141) | 54.2 | 0.58 |
| (061) | 63.6 | 0.44 |
| (hk0) | 90 | 0 |

[a]Reproduced with permission [124]. Copyright 2020, Elsevier.

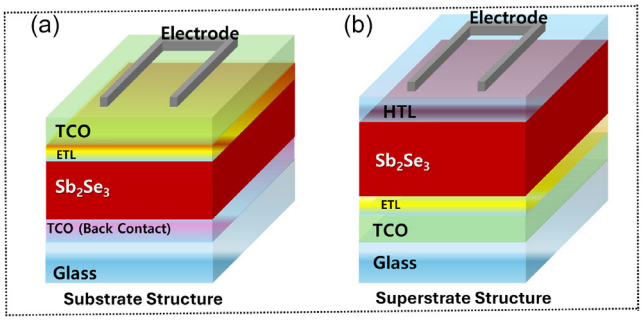


**FIGURE 15** | Bifacial (a) substrate and (b) superstrate configurations of $Sb_2Se_3$.

Pattini et al. [124] compared $Sb_2Se_3$ films grown on FTO and Mo substrates. Films on Mo were hk0-dominated, whereas those on FTO exhibited hk1 orientation with negligible hk0 planes, leading to improved performance (Figure 14i,j). Bifacial testing on FTO yielded front-side efficiency of 2.1% and rear-side efficiency of 0.8%, limited by imperfect Ohmic contact at the $Sb_2Se_3$-FTO interface. The Schottky contact at the FTO interface significantly enhances recombination while minimizing carrier collection, thereby affecting the performance of devices. Cheng et al. [134] introduced $NiO_x$ as a hole transport layer (HTL) at the interface between FTO and $Sb_2Se_3$ to address interfacial issues in $Sb_2Se_3$ bifacial devices. The device stack was FTO/$NiO_x$/$Sb_2Se_3$/CdS/i-ZnO/ITO/Al. By varying the oxygen to argon flow ratios (OAFR) during deposition (5%, 10%, 15%), they tuned both the oxidation state and defect density of $NiO_x$. X-ray photoelectron spectroscopy (XPS) showed that increasing OAFR suppressed the metallic $Ni^0$ phase while enhancing $Ni^{2+}$ and $Ni^{3+}$ signals, indicating greater oxidation as illustrated in Figure 17d–f. Electron paramagentic response (EPR) further revealed that oxygen vacancy concentration rose with OAFR, reaching its highest level at 15% (Figure 17g). While oxidation improves interface energetics, excess vacancies can introduce defect states that hinder charge transport and promote recombination. The optical transparency of $NiO_x$ was evaluated using UV-Vis spectroscopy, given its importance for bifacial illumination. $NiO_x$ 5% exhibited relatively low transmittance due to

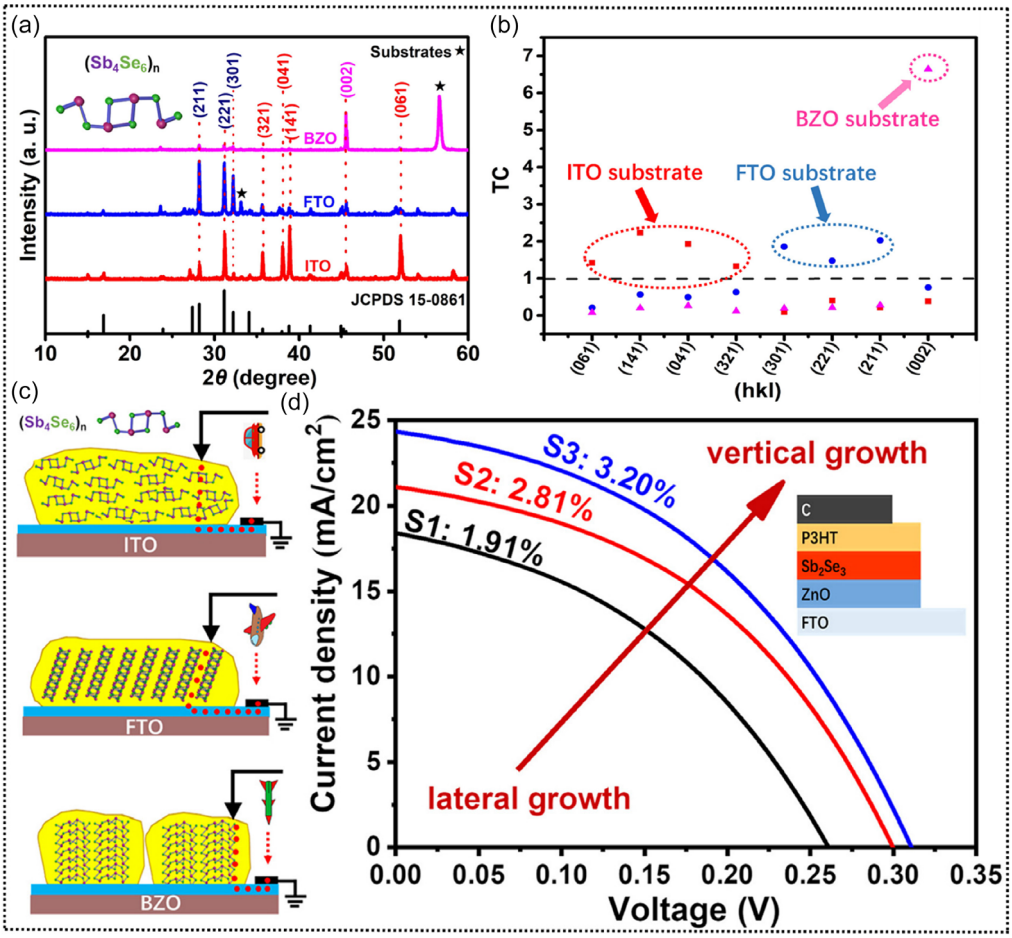


**FIGURE 16** | (a) $Sb_2Se_3$ grown on BZO, FTO, and ITO. (b) TC values on different substrates. (c) Graphical representation of growth orientation on ITO, FTO, and BZO. (d) J–V curves for devices grown on FTO. Reproduced with permission [132]. Copyright 2021, Elsevier.

strong absorption and reflection from residual $Ni^0$. At 15%, although metallic $Ni^0$ was largely eliminated, the abundance of oxygen vacancies introduced additional light scattering centers, producing the lowest transparency. The best balance was observed in $NiO_x$ 10% where sufficient oxidation was achieved with comparatively fewer vacancies, leading to the highest transmittance (Figure 17h). These material characteristics are translated directly into device performance. Under single-sided illumination, $NiO_x$ 10% devices reached efficiencies of 4.86% (FTO side) and 4.38% (Al side), while under bifacial (1 sun front + 0.2 sun rear) illumination, performance improved to 6.72 mW/cm$^2$ with a bifaciality factor ≈0.90 (Figure 17i–k). The results highlight $NiO_x$ 10% as the optimal condition, where complete oxidation and minimized vacancy formation enabled improved transparency and better FTO-$Sb_2Se_3$ interface, producing the best bifacial response.

Similarly, Qian et al. [135] reported the first demonstration of bifacial and semi-transparent $Sb_2(S, Se)_3$ solar cells (BSSCs), targeting applications in BIPV, indoor applications, space, and tandem devices. The device structure (FTO/CdS/$Sb_2(S, Se)_3$/MnS/ITO) incorporated a thin (≈350 nm) fully depleted absorber prepared by hydrothermal growth, manganese (II) sulfide (MnS) as a hole transport layer (HTL), and sputtered ITO as a transparent rear contact. The BSSCs achieved 7.41% efficiency under front (FTO-side) illumination and 6.36% under rear (ITO-side) illumination, corresponding to a bifaciality factor of 0.86 as shown in Figure 17a. Compared with opaque Au-contacted monofacial devices (9.5% front, 0.7% rear), the bifacial cells showed superior adaptability under albedo and tilted illumination, highlighting their suitability for real-world deployment (Figure 17c). Owing to their semitransparency, the devices were further integrated into a four-terminal $Sb_2(S, Se)_3$/Si tandem, achieving a preliminary 11.66% PCE. However, performance was still limited by the MnS/ITO interface, where Schottky barrier formation reduced charge extraction. Ultraviolet spectroscopy revealed a 0.44 eV offset between MnS and ITO, leading to unfavorable band bending and a barrier to hole transport. This resulted in a significant drop in $V_{OC}$ (0.541 vs 0.623 V) and FF (58.3% VS 64.5%) relative to Au-contacted devices, while capacitance profiling confirmed higher interface defect densities in BSSCs (Figure 17b). Such non-Ohmic contact at transparent back interfaces are a recurring issue in bifacial chalcogenides, including CdTe and CZTS, where replacing opaque materials like TCOs often introduces barriers and recombination losses. Various strategies such as inserting interlayers, doping, or tuning TCO work function have been employed to address similar challenges. For $Sb_2(S, Se)_3$, Qian et al.'s work underscores that while high bifaciality and semitransparency are achievable, transparent back-contact engineering remains the critical bottleneck to improving efficiency. A detailed comparison of the record efficiencies of Sb(Se, S) solar cells in monofacial & bifacial devices is presented in Table 6.

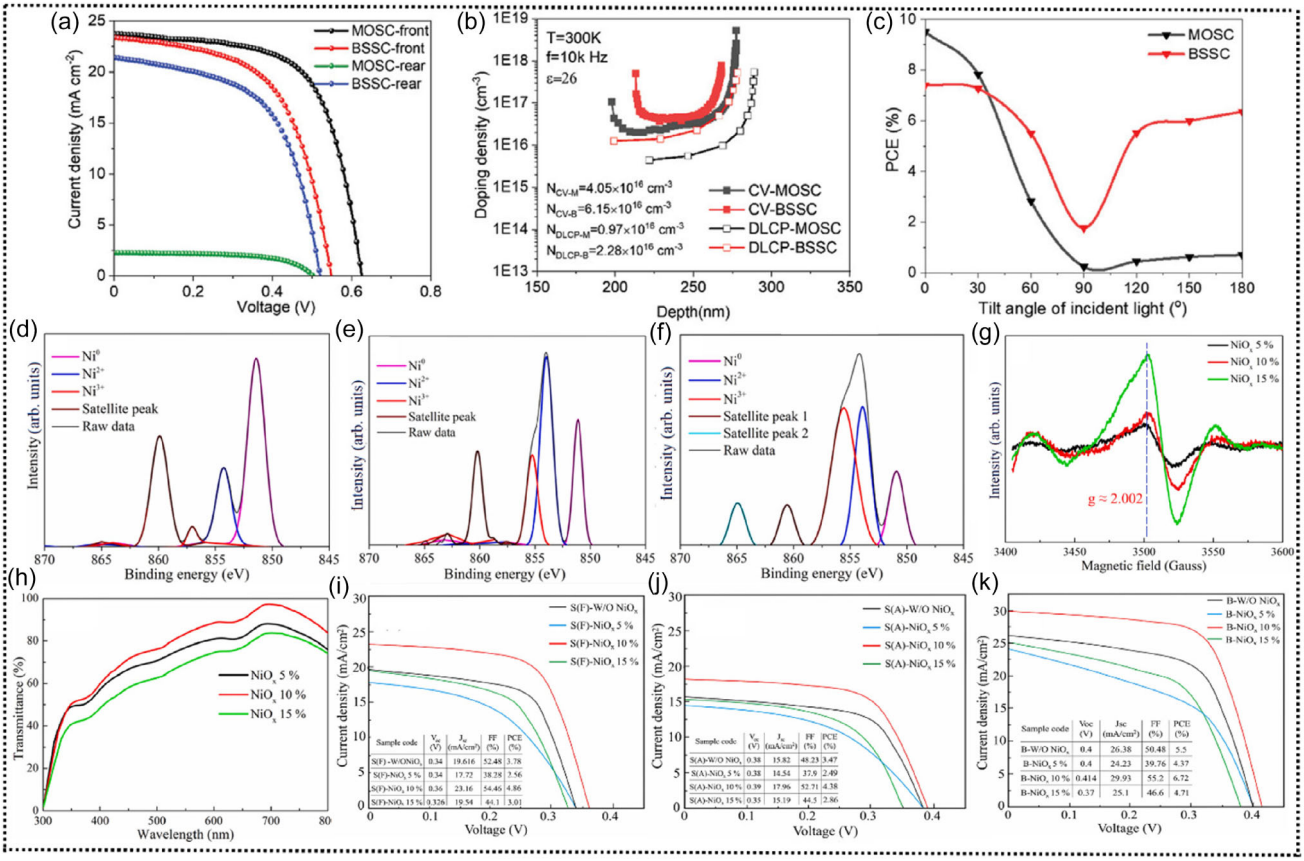


**FIGURE 17** | (a) J–V curves of champion monofacial (MOSC) and bifacial (BSSC) $Sb_2(S, Se)_3$ devices. (b) Defect concentration of champion monofacial (MOSC) and bifacial (BSSC) $Sb_2(S, Se)_3$ devices. (c) Schematic diagram for measuring Photovoltaic performance under different rotation angles. XPS spectra of $NiO_x$ (d) 5%, (e) 10%, (f) 15%, and (g) EPR response of varying $NiO_x$ OAFR. (h) Transmittance of $NiO_x$ films (i–k) front, rear, and bifacial illumination J–V curves with varying $NiO_x$ amounts. (a–c) are reproduced with permission [135], copyright 2023, John Wiley and Sons and (d–k) are reproduced with permission [134], Copyrights 2025, Elsevier.

**TABLE 6** | Summary of champion monofacial and bifacial Sb chalcogenide solar cells.

| Absorber | Architecture | Illumination | Best PCE (%) | Key device |
|---|---|---|---|---|
| $Sb_2Se_3$ | Monofacial | Front | 10.57 | Additive-assisted CBD; superstrate CdS/$Sb_2Se_3$ [117] |
| $Sb_2Se_3$ | Monofacial | Front | 10.12 | Interface/transport optimization; substrate configuration [115] |
| $Sb_2S_3$ | Monofacial | Front | 8.0 | High-quality $Sb_2Se_3$ absorber synthesis; superstrate [118] |
| $Sb_2(S, Se)_3$ | Monofacial | Front | 10.75 | Hydrothermal synthesis; superstrate [120] |
| $Sb_2Se_3$ | Bifacial | Front | 4.86 | $NiO_x$ interfacial layer, improved FTO- $Sb_2Se_3$ interface |
| | | Rear | 4.38 | Bifaciality ≈0.90 (rear/front PCE) [134] |
| $Sb_2(S, Se)_3$ | Bifacial | Front | 7.41 | MnS/ITO rear TCO, thin n-i-p enabling high transmittance |
| | | Rear | 6.36 | bifaciality ≈0.86 (rear/front PCE) [135] |

### 2.4.2 | Challenges in Sb2Se3, Sb2S3, and Sb2(S, Se)3 Bifacial Devices

Overall, these findings highlight three key points for future bifacial Sb chalcogenide research.

Grain orientation control, specifically the preferential alignment along [002] or near-vertical hk1 planes, and the suppression of hk0 growth are crucial to ensure efficient carrier transport and collection under both front and rear illumination. Substrate and interface engineering: The choice of substrate strongly affects the orientation and transport properties of $Sb_2Se_3$. Tailoring interfacial chemistry, such as modification of CdS, or selecting substrates that favor vertical ribbon alignment, and ensuring an ohmic contact, are key to suppressing recombination and improving charge extraction. Growth condition optimization: $Sb_2Se_3$ can be fabricated using different deposition techniques such as CSS, RTE, and sputtering. By carefully tuning growth parameters (temperature, atmosphere, pressure, thickness), the growth orientation can be optimized toward preferential (002) or hk1. Such control is

essential for enabling high-quality transport along the $[Sb_4Se_6]_n$ ribbons. Although supporting studies were performed on monofacial devices, the extrapolation of those orientation-dependent transport effects provides a practical framework for guiding bifacial Sb chalcogenide research, identifying orientation and substrate engineering as critical levers for improving performance.

#### 2.4.3 | Future Aspects of Sb2Se3, Sb2S3, and Sb2(S, Se)3 Bifacial Devices

Antimony-based chalcogenide solar cells, such as $Sb_2Se_3$ and $Sb_2S_3$, are increasingly being recognized as promising next-generation absorbers due to their earth-abundant composition, low toxicity, and excellent optoelectronic properties. Looking forward, one important research direction lies in bifacial device configurations, where the intrinsically anisotropic crystal orientation of Sb-based absorbers can be optimized for bidirectional light absorption. This approach can enhance photocurrent by harvesting photons from both the front and rear sides, especially when integrated with transparent conductive back contacts. Further improvements in defect passivation, control over carrier lifetime, and interface engineering with wide-bandgap transparent transport layers will be key to achieving competitive bifacial power conversion efficiencies. Such developments will not only boost maximum achievable power but also expand application potential in building-integrated photovoltaics (BIPV) and semi-transparent device platforms.

Another exciting future prospect is the integration of antimony chalcogenides into tandem solar cell architectures, both in 2-terminal (monolithic) and 4-terminal (mechanically stacked) configurations. $Sb_2Se_3$, with its wider bandgap (≈1.7 eV), is well suited as a top absorber when paired with narrow bandgap $Sb_2Se_3$ (≈1.1–1.2 eV) as the bottom cell, enabling highly efficient all-antimony tandems. In 2-terminal devices, lattice and band alignment engineering, along with optimized tunnel recombination junctions, will be critical to minimizing interfacial recombination losses. In contrast, 4-terminal architecture offers more flexibility, as each sub-cell can be independently optimized, thus bypassing current-matching constraints (Figure 5). With proper bandgap tuning through alloying or compositional grading, Sb-based tandems could realistically target efficiencies exceeding 25%, positioning them as strong competitors to established perovskite-silicon tandems while offering superior stability and sustainability.

## 3 | Conclusion and Prospect

This review emphasizes bifacial inorganic chalcogenide solar cells as a significant advancement in addressing the efficiency and stability constraints of traditional monofacial photovoltaics. These devices enhance photocurrent generation by harvesting light from both the front and rear sides, resulting in improved energy yields under diffuse and high-albedo conditions, as well as increased operational resilience. Recent advancements in $Cu(In, Ga)(S, Se)_2$, CdTe, $Cu_2ZnSn(S, Se)_4$, and $Sb_2(S, Se)_3$ thin films highlight their adjustable band gaps, significant absorption capabilities, and scalable manufacturing processes. However, these materials also face challenges, including nonradiative recombination, interfacial instabilities, and parasitic optical losses. This review also examines advances in both rigid and flexible substrate–based solar cell configurations for chalcogenide-based SCs. Particular attention is given to back contact engineering, where transparent and conductive materials are critical for enhancing rear-side response. Strategies to optimize these contacts are discussed for maximizing bifacial responses of single junction SCs. Bifacial tandem with 2T and 4T architectures represent a promising avenue, as strategic bandgap engineering and subcell pairing have the potential to exceed the Shockley–Queisser limit. To realize this potential, it is essential to implement transparent low-resistance contacts, ensure robust interface passivation, employ advanced light-management strategies, and conduct validation under realistic outdoor conditions. Overcoming these challenges is crucial for transitioning bifacial chalcogenides from laboratory demonstrations to commercially viable technologies, thereby establishing them as promising candidates for next-generation high-efficiency, cost-effective solar energy conversion.


### Acknowledgments

This research was supported by the National Research Foundation of Korea (NRF) grant funded by the Korean Government (MSIT) (nos. RS-2023-NR076874, RS-2025-02311266, and RS-2025-02315803) and by the Korea Institute for Advancement of Technology (KIAT) grant funded by the Ministry of Trade, Industry and Energy (MOTIE) (no. P0024567). This work was also supported by the DGIST R&D programs and the InnoCORE program funded by the Korean Government (MSIT) (nos. 25-PCOE-01, 25-ET-01, and 1.250021.01).

### Funding

This work is supported by National Research Foundation of Korea (NRF) (RS-2023-NR076874, RS-2025-02311266, RS-2025-02315803), Korea Institute for Advancement of Technology (KIAT) (P0024567), DGIST R&D Programs and InnoCORE (25-PCOE-01, 25-ET-01, 1.250021.01).


### Conflicts of Interest

The authors declare no conflicts of interest.

### Data Availability Statement

The data that support the findings of this study are available from the corresponding author upon reasonable request.

### References


1. Y. Liang, R. Kleijn, and E. Van der Voet, "Increase in Demand for Critical Materials under IEA Net-Zero Emission by 2050 scenario," *Applied Energy* 346 (2023): 121400.

2. B. Lin and Y. Liu, "Global Carbon Neutrality and China's Contribution: The Impact of International Carbon Market Policies on China's Photovoltaic Product Exports," *Energy Policy* 193 (2024): 114299, https://doi.org/10.1016/j.enpol.2024.114299.

3. A. Aleksandra, B. P. Sara, J. Małgorzata, B. Brian, P. Davide, and C. Miguel, "Role of Solar PV in Net-Zero Growth: An Analysis of International Manufacturers and Policies," *Progress in Photovoltaics: Research and Applications* 32, no. 9 (2024): 607–622, https://doi.org/10.1002/pip.3797.

4. K. Lee, H. D. Um, D. Choi, et al., "The Development of Transparent Photovoltaics," *Cell Reports. Physical Science* 1, no. 8 (2020): 100143.

5. D. I. Al Huneidi, F. Tahir, and S. G. Al-Ghamdi, "Energy Modeling and Photovoltaics Integration as a Mitigation Measure for Climate Change Impacts on Energy Demand," *Energy Reports* 8 (2022): 166–171, https://doi.org/10.1016/j.egyr.2022.01.105.

6. S. Fankhauser, S. M. Smith, M. Allen, et al., "The Meaning of Net Zero and How to Get It Right," *Nature Climate Change* 12, no. 1 (2022): 15–21, https://doi.org/10.1038/s41558-021-01245-w.

7. M. Wang, X. Mao, Y. Xing, et al., "Breaking down Barriers on PV Trade Will Facilitate Global Carbon Mitigation," *Nature Communications* 12, no. 1 (2021): 1–16, https://doi.org/10.1038/s41467-021-26547-7.

8. N. L. Chang, B. K. Newman, and R. J. Egan, "Future Cost Projections for Photovoltaic Module Manufacturing Using a Bottom-up Cost and Uncertainty Model," *Solar Energy Materials and Solar Cells* 237 (2022): 111529, https://doi.org/10.1016/j.solmat.2021.111529.

9. A. Hubner, A. G. Aberle, and R. Hezel, "Cost-Effective Bifacial Silicon Solar Cells With 19% Front and 18% Rear Efficiency," in *Conference Record of the Twenty Fifth IEEE Photovoltaic Specialists Conference-1996*, (IEEE, 1996), 489–492.

10. G. Kavlak, J. McNerney, and J. E. Trancik, "Evaluating the Causes of Cost Reduction in Photovoltaic Modules," *Energy Policy* 123 (2018): 700–710, https://doi.org/10.1016/j.enpol.2018.08.015.

11. B. Ehrler, E. Alarcón-Lladó, S. W. Tabernig, T. Veeken, E. C. Garnett, and A. Polman, "Photovoltaics Reaching for the Shockley-Queisser Limit," *ACS Energy Letters* 5, no. 9 (2020): 3029–3033, https://doi.org/10.1021/acsenergylett.0c01790.

12. L. Szabo, M. Moner- Girona, A. Jäger-Waldau, et al, "Impacts of Large-Scale Deployment of Vertical Bifacial Photovoltaics on European Electricity Market Dynamics," *Nature Communications* 15, no. 1 (2024): 1–16, https://doi.org/10.1038/s41467-024-50762-7.

13. Q. Jiang, Z. Song, R. C. Bramante, et al., "Highly Efficient Bifacial Single-Junction Perovskite Solar Cells," *Joule* 7, no. 7 (2023): 1543–1555, https://doi.org/10.1016/j.joule.2023.06.001.

14. J. Sun and J. J. Jasieniak, "Semi-Transparent Solar Cells," *Journal of Physics D: Applied Physics* 50, no. 9 (2017): 93001.

15. N. Alhammadi, E. Rodriguez-Ubinas, S. Alzarouni, and M. Alantali, "Building-Integrated Photovoltaics in Hot Climates: Experimental Study of CIGS and c-Si Modules in BIPV Ventilated Facades," *Energy Conversion and Management* 274 (2022): 116408.

16. E. Mirabi, F. Akrami Abarghuie, and R. Arazi, "Integration of Buildings with Third-Generation Photovoltaic Solar Cells: A Review," *Clean Energy* 5, no. 3 (2021): 505–526.

17. M. Victoria, N. Haegel, I. M. Peters, et al., "Solar Photovoltaics Is Ready to Power a Sustainable Future," *Joule* 5, no. 5 (2021): 1041–1056.

18. R. Hosseinian Ahangharnejhad, W. Becker, J. Jones, et al., "Environmental Impact per Energy Yield for Bifacial Perovskite Solar Cells Outperforms Crystalline Silicon Solar Cells," *Cell Reports. Physical Science* 1, no. 10 (2020): 100216, https://doi.org/10.1016/j.xcrp.2020.100216.

19. F. Tahir, A. A. B. Baloch, and S. G. Al-Ghamdi, "Impact of Climate Change on Solar Monofacial and Bifacial Photovoltaics (PV) Potential in Qatar," *Energy Reports* 8 (2022): 518–522, https://doi.org/10.1016/j.egyr.2022.02.197.

20. S. Ramesh, A. Tuomiranta, G. H. Yordanov, H. Badran, A. Hajjiah, B. Vermang, and J. Poortmans, "Energy Yield Framework to Simulate Thin Film CIGS Solar Cells and Analyze Limitations of the Technology," *Scientific Reports* 15, no. 1 (2025): 1–13, https://doi.org/10.1038/s41598-024-78862-w.

21. J. Keller, K. Kiselman, O. D. Gargand, et al., "High-Concentration Silver Alloying and Steep Back-Contact Gallium Grading Enabling Copper Indium Gallium Selenide Solar Cell with 23.6% Efficiency," *Nature Energy* 9, no. 4 (2024): 467–478.

22. I. Jeong, T. K. Lee, H. Van Tran, et al., "Flexible and Lightweight Perovskite/Cu(In, Ga)$Se_2$ Tandem Solar Cells," *Joule* 9, no. 3 (2025): 101794, https://doi.org/10.1016/j.joule.2024.11.011.

23. I. M. Peters and T. Buonassisi, "Energy Yield Limits for Single-Junction Solar Cells," *Joule* 2, no. 6 (2018): 1160–1170, https://doi.org/10.1016/j.joule.2018.03.009.

24. V. K. Kapur, V. K. Kapur, A. Bansal, and S. Roth, "*Roadmap for Manufacturing Cost Competitive CIGS Modules," in Conference Record of the IEEE Photovoltaic Specialists Conference*, (2012), 3343–3348.

25. N. Cavallari, F. Pattini, S. Rampino, et al., "Low Temperature Deposition of Bifacial CIGS Solar Cells on Al-Doped Zinc Oxide Back Contacts," *Applied Surface Science* 412 (2017): 52–57, https://doi.org/10.1016/j.apsusc.2017.03.242.

26. T. Nakada, Y. Hirabayashi, T. Tokado, D. Ohmori, and T. Mise, "Novel Device Structure for Cu (In,Ga)$Se_2$ Thin Film Solar Cells Using Transparent Conducting Oxide Back and Front Contacts," *Solar Energy* 77, no. 6 (2004): 739–747.

27. M. J. Shin, A. Lee, A. Cho, et al., "Semitransparent and Bifacial Ultrathin Cu (In, Ga)$Se_2$ Solar Cells via a Single-Stage Process and Light-Management Strategy," *Nano Energy* 82 (2021): 105729.

28. A. F. Violas, A. J. N. Oliveira, P. A. Fernandes, P. M. P. Salomé, and J. P. Teixeira, "CIGS Bifacial Solar Cells with Novel Rear Architectures: Simulation Point of View and the Creation of a Digital Twin," *Solar Energy Materials and Solar Cells* 272 (2024): 112899, https://doi.org/10.1016/j.solmat.2024.112899.

29. S.-C. Yang, T.-Y. Lin, M. Ochoa, et al., "Efficiency Boost of Bifacial Cu(In, Ga)$Se_2$ Thin-Film Solar Cells for Flexible and Tandem Applications with Silver-Assisted Low-Temperature Process," *Nature Energy* 8, no. 1 (2023): 40–51, https://doi.org/10.1038/S41560-022-01157-9.

30. S.-C. Yang, T. Y. Lin, M. Ochoa, et al., "Efficiency Boost of Bifacial Cu (In, Ga) $Se_2$ Thin-Film Solar Cells for Flexible and Tandem Applications with Silver-Assisted Low-Temperature Process," *Nature Energy* 8, no. 1 (2023): 40–51.

31. K. Kim and W. N. Shafarman, "Alternative Device Structures for CIGS-Based Solar Cells with Semi-Transparent Absorbers," *Nano Energy* 30 (2016): 488–493, https://doi.org/10.1016/j.nanoen.2016.10.038.

32. A. Ali, D. H. Jeon, V. Q. Hoang, et al., "Exploring the Influence of TCO Thickness and Ag Addition on Performance of CIGS Thin Film Solar Cells for Bifacial and Tandem Configurations" in *Electrochemical Society Meeting Abstracts prime2024* (The Electrochemical Society, Inc, 2024), 1755.

33. T. Nakada, "Microstructural and Diffusion Properties of CIGS Thin Film Solar Cells Fabricated Using Transparent Conducting Oxide Back Contacts," *Thin Solid Films* 480-481 (2005): 419–425, https://doi.org/10.1016/j.tsf.2004.11.142.

34. J. Zhang, Z. Ma, Y. Zhang, et al., "Highly Efficient Narrow Bandgap Cu(In, Ga)$Se_2$ Solar Cells with Enhanced Open Circuit Voltage for Tandem Application," *Nature Communications* 15, no. 1 (2024): 10365, https://doi.org/10.1038/s41467-024-54818-6.

35. D. Adeleye, M. Sood, A. Valluvar Oli, et al., "Wide-Bandgap Cu(In, Ga)$S_2$ Solar Cell: Mitigation of Composition Segregation in High Ga Films for Better Efficiency" *Small* 21, no. 8 (2025): 1–14, https://doi.org/10.1002/smll.202405221.

36. M. A. Ruiz-Preciado, F. Gota, P. Fassl, et al., "Monolithic Two-Terminal Perovskite/CIS Tandem Solar Cells with Efficiency Approaching 25%," *ACS Energy Letters* 7, no. 7 (2022): 2273–2281, https://doi.org/10.1021/acsenergylett.2c00707.

37. A. Bojar, D. Micha, M. Giteau, et al., "Optical Simulations and Optimization of Perovskite/CI(G)S Tandem Solar Cells Using the Transfer Matrix Method," *Journal of Physics: Energy* 5, no. 3 (2023): 035001, https://doi.org/10.1088/2515-7655/accf34.

38. L. Zeng, L. Tang, Z. Luo, J. Gong, J. Li, and X. Xiao, "A Review of Perovskite/Copper Indium Gallium Selenide Tandem Solar Cells," *Solar RRL* 8 (2024): 2301059.

39. A. Ali, D. H. Jeon, W. Kim, et al., "Highly Efficient Bifacial Narrow Bandgap Ag-$CuInSe_2$ Solar Cells on ITO," *Advanced Energy Materials* 15, no. 23 (2025): 2500899, https://doi.org/10.1002/aenm.202500899.

40. A. Ali, D.-H. Jeon, W. Kim, et al., "Highly Efficient Bifacial Narrow Bandgap Ag-$CuInSe_2$ Solar Cells on ITO (Adv. Energy Mater. 23/2025)," *Advanced Energy Materials* 15, no. 23 (2025): 2570101, https://doi.org/10.1002/aenm.202570101.

41. D. Chen, F. Yang, M. Yang, et al., "A Stepwise Solvent-Annealing Strategy for High-Efficiency Four-Terminal Perovskite/Cu(InGa)Se2 Tandem Solar Cells," *Materials Today Energy* 49 (2025): 101816, https://doi.org/10.1016/j.mtener.2025.101816.

42. J. Keller, N. Shariati Nilsson, A. Aijaz, et al., "Using hydrogen-doped $In_2O_3$ films as a transparent back contact in (Ag,Cu)(In,Ga)$Se_2$ solar cells," *Progress in Photovoltaics: Research and Applications* 26, no. 3 (2018): 159–170, https://doi.org/10.1002/pip.2977.

43. J. Keller, L. Stolt, O. Donzel-Gargand, T. Kubart, and M. Edoff, "Wide-Gap Chalcopyrite Solar Cells with Indium Oxide–Based Transparent Back Contacts," *Solar RRL* 6, no. 8 (2022): 2200401, https://doi.org/10.1002/solr.202200401.

44. X. Guo, Z. Jia, S. Liu, et al., "Stabilizing Efficient Wide-Bandgap Perovskite in Perovskite-Organic Tandem Solar Cells," *Joule* 8, no. 9 (2024): 2554–2569, https://doi.org/10.1016/j.joule.2024.06.009.

45. J. Keller, L. Stolt, O. Donzel-Gargand, A. F. Violas, T. Kubart, and M. Edoff, "Bifacial Wide-Gap (Ag,Cu)(In,Ga)$Se_2$ Solar Cell with 13.6% Efficiency Using $In_2O_3$ :W as a Back Contact Material," *Solar RRL* 8, no. 15 (2024): 2400430, https://doi.org/10.1002/solr.202400430.

46. W. Wang, C. Zhang, B. Hu, et al., "Influence of Alkali Element Post-Deposition Treatment on the Performance of the CIGS Solar Cells on Flexible Stainless Steel Substrates," *Materials Letters* 302 (2021): 130410, https://doi.org/10.1016/j.matlet.2021.130410.

47. J. Keller, S. Mudgal, N. M. Martin, O. Donzel-Gargand, and M. Edoff, "Rubidium Fluoride Absorber Treatment for Wide-Gap and Bifacial Ag(In,Ga)$Se_2$ Solar Cells," *Solar RRL* 9, no. 16 (2025): 2500423, https://doi.org/10.1002/solr.202500423.

48. V.-Q. Hoang, D.-H. Jeon, H. K. Park, S. J. Sung, and D. H. Kim, "Advance Supply of Ag and Ga–Se for Increased Backside Ga and Enhanced Cu(In,Ga)$Se_2$ Solar Cell Efficiency," *ACS Applied Energy Materials* 6, no. 24 (2023): 12180–12189, https://doi.org/10.1021/acsaem.3c01439.

49. O. Lundberg, M. Edoff, and L. Stolt, "The Effect of Ga-Grading in CIGS Thin Film Solar Cells," *Thin Solid Films* 480-481 (2005): 520–525, https://doi.org/10.1016/j.tsf.2004.11.080.

50. S. Suresh, D. J. Rokke, A. A. Drew, E. Alruqobah, R. Agrawal, and A. R. Uhl, "Extrinsic Doping of Ink-Based Cu(In,Ga)$(S,Se)_2$ -Absorbers for Photovoltaic Applications," *Advanced Energy Materials* 12, no. 18 (2022): 2103961, https://doi.org/10.1002/aenm.202103961.

51. R. Gutzler, W. Witte, A. Kanevce, D. Hariskos, and S. Paetel, "$V_{OC}$-losses across the band gap: Insights from a high-throughput inline process for CIGS solar cells," *Progress in Photovoltaics: Research and Applications* 31, no. 10 (2023): 1023–1031, https://doi.org/10.1002/pip.3707.

52. G. T. Chavan, Y. Kim, M. Q. Khokhar, et al., "A Brief Review of Transparent Conducting Oxides (TCO): The Influence of Different Deposition Techniques on the Efficiency of Solar Cells," *Nanomaterials* 13, no. 7 (2023): 1226, https://doi.org/10.3390/nano13071226.

53. V. C. Karade, M. He, Z. Song, et al., "Opportunities and Challenges for Emerging Inorganic Chalcogenide-Silicon Tandem Solar Cells," *Energy & Environmental Science* 18 (2025): 6899–6933, https://doi.org/10.1039/d4ee04526b.

54. A. Morales-Acevedo, "Thin Film CdS/CdTe Solar Cells: Research Perspectives," *Solar Energy* 80, no. 6 (2006): 675–681, https://doi.org/10.1016/j.solener.2005.10.008.

55. B. John and S. Varadharajaperumal, "Comprehensive Review on CdTe Crystals: Growth, Properties, and Photovoltaic Application," *Physics of Metals and Metallography* 124, no. 14 (2023): 1795–1812, https://doi.org/10.1134/S0031918X2110094X.

56. D. Pokhrel, E. Bastola, K. Khanal Subedi, et al., "Copper Iodide Nanoparticles as a Hole Transport Layer to CdTe Photovoltaics: 5.5% Efficient Back-Illuminated Bifacial CdTe Solar Cells," *Solar Energy Materials and Solar Cells* 235 (2022): 111451, https://doi.org/10.1016/j.solmat.2021.111451.

57. I. M. Dharmadasa, "Review of the $CdCl_2$ Treatment Used in CdS/CdTe Thin Film Solar Cell Development and New Evidence towards Improved Understanding," *Coatings* 4, no. 2 (2014): 282–307, https://doi.org/10.3390/coatings4020282.

58. U. Manimaran, and M. Shrinivas Dangate, "A Review on Conducting Materials in CdTe Photovoltaic Cells," *ACS Omega* 10, no. 23 (2025): 23858–23872, https://doi.org/10.1021/acsomega.5c01030.

59. A. Romeo, G. Khrypunov, S. Galassini, H. Zogg, and A. N. Tiwari, "Bifacial Configurations for CdTe Solar Cells," *Solar Energy Materials and Solar Cells* 91, no. 15-16 (2007): 1388–1391, https://doi.org/10.1016/j.solmat.2007.03.010.

60. S. Marsillac, V. Y. Parikh, and A. D. Compaan, "Ultra-Thin Bifacial CdTe Solar Cell," *Solar Energy Materials and Solar Cells* 91, no. 15–16 (2007): 1398–1402, https://doi.org/10.1016/j.solmat.2007.04.025.

61. X. Zhang, X. Yang, Y. Zheng, Y. Tai, J. Zhang, and B. Li, "Study on the Bifacial Ultrathin CdTe Solar Cell With ZnTe: N/IWO Composite Transparent Back Electrode," *IEEE Journal of Photovoltaics* 15 (2025): 40–45, https://doi.org/10.1109/jphotov.2024.3483249.

62. M. M. Aliyu, M. A. Islam, N. R. Hamzah, et al., "Recent Developments of Flexible CdTe Solar Cells on Metallic Substrates: Issues and Prospects," *International Journal of Photoenergy* 2012, no. 1 (2012): 351381, https://doi.org/10.1155/2012/351381.

63. T. Song, A. Moore, and J. R. Sites, "Te Layer to Reduce the CdTe Back-Contact Barrier," *IEEE Journal of Photovoltaics* 8, no. 1 (2018): 293–298, https://doi.org/10.1109/jphotov.2017.2768965.

64. D. Kuciauskas, C. L. Perkins, M. Nardone, C. Lee, R. Mallick, and G. Xiong, "Band Bending at CdTe Solar Cell Contacts: Correlating Electro-Optical and X-Ray Photoelectron Spectroscopy Analyses of Thin Film Solar Cells," *Solar RRL* 7, no. 10 (2023): 2300073, https://doi.org/10.1002/solr.202300073.

65. M. A. Scarpulla, B. McCandless, A. B. Phillips, et al., "CdTe-Based Thin Film Photovoltaics: Recent Advances, Current Challenges and Future Prospects," *Solar Energy Materials and Solar Cells* 255 (2023): 112289, https://doi.org/10.1016/j.solmat.2023.112289.

66. G. K. Liyanage, A. B. Phillips, F. K. Alfadhili, R. J. Ellingson, and M. J. Heben, "The Role of Back Buffer Layers and Absorber Properties for >25% Efficient CdTe Solar Cells," *Acs Applied Energy Materials* 2, no. 8 (2019): 5419–5426, https://doi.org/10.1021/acsaem.9b00367.

67. K. K. Subedi, A. B. Phillips, N. Shrestha, et al., "Enabling Bifacial Thin Film Devices by Developing a Back Surface Field Using $CuxAlO_y$," *Nano Energy* 83 (2021): 105827, https://doi.org/10.1016/j.nanoen.2021.105827.

68. D. Pokhrel, X. Mathew, K. Khanal Subedi, et al., "Bifacial CdTe Solar Cells with Copper Chromium Oxide Back-Buffer Layer," *Solar RRL* 6, no. 11 (2022): 2200501, https://doi.org/10.1002/solr.202200501.

69. C. P. Muzzillo, M. O. Reese, C. Lee, and G. Xiong, "Cracked Film Lithography with $CuGaO_x$ Buffers for Bifacial CdTe Photovoltaics," *Small* 19, no. 28 (2023): 2301939, https://doi.org/10.1002/smll.202301939.

70. B. E. Sartor, T. Zhang, C. P. Muzzillo, et al., "Hierarchical Transparent Back Contacts for Bifacial CdTe PV," *ACS Energy Letters* 9, no. 4 (2024): 1617–1623, https://doi.org/10.1021/acsenergylett.4c00156.

71. S. Rojsatien, A. Mannodi-Kanakkithodi, T. Walker, et al., "Distribution of Copper States, Phases, and Defects across the Depth of a Cu-Doped CdTe Solar Cell," *Chemistry of Materials* 35, no. 23 (2023): 9935–9944, https://doi.org/10.1021/acs.chemmater.3c01688.

72. E. Artegiani, J. D. Major, H. Shiel, V. Dhanak, C. Ferrari, and A. Romeo, "How the Amount of Copper Influences the Formation and Stability of Defects in CdTe Solar Cells," *Solar Energy Materials and Solar Cells* 204 (2020): 110228, https://doi.org/10.1016/j.solmat.2019.110228.

73. J. Perrenoud, L. Kranz, C. Gretener, et al., "A Comprehensive Picture of Cu Doping in CdTe Solar Cells," *Journal of Applied Physics* 114, no. 17 (2013): 174505, https://doi.org/10.1063/1.4828484/378837.

74. A. Danielson, C. Reich, R. Pandey, et al., "Electro-Optical Characterization of Arsenic-Doped CdSeTe and CdTe Solar Cell Absorbers Doped in-Situ during Close Space Sublimation," *Solar Energy Materials and Solar Cells* 251 (2023): 112110, https://doi.org/10.1016/j.solmat.2022.112110.

75. L. Kranz, C. Gretener, J. Perrenoud, et al., "Doping of Polycrystalline CdTe for High-Efficiency Solar Cells on Flexible Metal Foil," *Nature Communications* 4, no. 1 (2013): 1–7, https://doi.org/10.1038/ncomms3306.

76. C. Gretener, J. Perrenoud, L. Kranz, et al., "CdTe/CdS Thin Film Solar Cells Grown in Substrate Configuration," *Progress in Photovoltaics: Research and Applications* 21, no. 8 (2013): 1580–1586, https://doi.org/10.1002/pip.2233.

77. R. R. Khanal, A. B. Phillips, Z. Song, et al., "Substrate Configuration, Bifacial CdTe Solar Cells Grown Directly on Transparent Single Wall Carbon Nanotube Back Contacts," *Solar Energy Materials and Solar Cells* 157 (2016): 35–41, https://doi.org/10.1016/j.solmat.2016.05.001.

78. M A. Green, E D. Dunlop, M. Yoshita, et al., "Solar Cell Efficiency Tables (Version 66)," *Progress in Photovoltaics: Research and Applications* 33, no. 7 (2025): 795–810, https://doi.org/10.1002/pip.3919.

79. O. Almora, G. C. Bazan, C. I. Cabrera, et al., "Device Performance of Emerging Photovoltaic Materials (Version 5)," *Advanced Energy Materials* 15, no. 12 (2025): 2404386, https://doi.org/10.1002/aenm.202404386.

80. J. Li, D. Wang, X. Li, Y. Zeng, and Y. Zhang, "Cation Substitution in Earth-Abundant Kesterite Photovoltaic Materials," *Advanced Science* 5, no. 4 (2018): 1700744, https://doi.org/10.1002/advs.201700744.

81. M. Parans, P. Winnie, W.-N. Raghu, and N. Bhattacharya, "*Springer Series in Materials Science 218 Semiconductor Materials for Solar Photovoltaic Cells*," accessed July 19, 2025, http://www.springer.com/series/856.

82. U. A. Shah, A. Wang, M. Irfan Ullah, et al., "A Deep Dive into $Cu_2ZnSnS_4$ (CZTS) Solar Cells: A Review of Exploring Roadblocks, Breakthroughs, and Shaping the Future," *Small* 20, no. 30 (2024): 2310584, https://doi.org/10.1002/smll.202310584.

83. Y. Li, H. Wei, C. Cui, et al., "CZTSSe Solar Cells: Insights into Interface Engineering," *Journal of Materials Chemistry A* 11, no. 10 (2023): 4836–4849, https://doi.org/10.1039/d2ta09561k.

84. J. Li, Y. Huang, J. Huang, et al., "Defect Control for 12.5% Efficiency $Cu_2ZnSnSe_4$ Kesterite Thin-Film Solar Cells by Engineering of Local Chemical Environment," *Advanced Materials* 32, no. 52 (2020): 2005268, https://doi.org/10.1002/adma.202005268.

85. K. Yin, J. Wang, L. Lou, et al., "Gradient Bandgaps in Sulfide Kesterite Solar Cells Enable over 13% Certified Efficiency," *Nature Energy* 10, no. 2 (2025): 205–214, https://doi.org/10.1038/s41560-024-01681-w.

86. M. Kangsabanik and R. N. Gayen, "A Comprehensive Review on the Recent Strategy of Cation Substitution in CZTS(Se) Thin Films to Achieve Highly Efficient Kesterite Solar Cells," *Solar RRL* 7, no. 24 (2023): 2300670, https://doi.org/10.1002/solr.202300670.

87. J. Ge, J. Chu, J. Jiang, Y. Yan, and P. Yang, "Characteristics of in-Substituted CZTS Thin Film and Bifacial Solar Cell," *ACS Applied Materials & Interfaces* 6, no. 23 (2014): 21118–21130, https://doi.org/10.1021/am505980n.

88. A. Wang, J. Huang, C. Yan, et al., "Cd-Free High-Bandgap $Cu_2ZnSnS_4$ Solar Cell with 10.7% Certified Efficiency Enabled by Engineering Sn-Related Defects," *Advanced Functional Materials* 34, no. 45 (2024): 2407063, https://doi.org/10.1002/adfm.202407063.

89. D. Shin, B. Saparov, and D. B. Mitzi, "Defect Engineering in Multinary Earth-Abundant Chalcogenide Photovoltaic Materials," *Advanced Energy Materials* 7, no. 11 (2017): 1602366, https://doi.org/10.1002/aenm.201602366.

90. J. S. Kim, D. H. Kim, and D. K. Hwang, "Efficiency Enhancement of Bifacial $Cu_2ZnSnSe_4$ Thin-Film Solar Cells on Indium Tin Oxide Glass Substrates by Suppressing In-Sn Diffusion with Mo Interlayer," *Journal of Power Sources* 400 (2018): 9–15, https://doi.org/10.1016/j.jpowsour.2018.08.001.

91. J. Ge, Y. Yu, W. Ke, et al., "Improved Performance of Electroplated CZTS Thin-Film Solar Cells with Bifacial Configuration," *ChemSusChem* 9, no. 16 (2016): 2149–2158, https://doi.org/10.1002/cssc.201600440.

92. J. Ge, J. Chu, J. Jiang, Y. Yan, and P. Yang, "The Interfacial Reaction at ITO Back Contact in Kesterite CZTSSe Bifacial Solar Cells," *ACS Sustainable Chemistry & Engineering* 3, no. 12 (2015): 3043–3052, https://doi.org/10.1021/acssuschemeng.5b00962.

93. Y. Ji, W. Chen, D. Yan, et al., "An ITO-Free Kesterite Solar Cell," *Small* 20, no. 6 (2024): 2307242, https://doi.org/10.1002/smll.202307242.

94. F. I. Lai, J. F. Yang, W. C. Chen, Y. C. Hsu, and S. Y. Kuo, "Weatherability of $Cu_2ZnSnSe_4$ Thin Film Solar Cells on Diverse Substrates," *Solar Energy* 195 (2020): 626–635, https://doi.org/10.1016/j.solener.2019.11.089.

95. F. Jiang, C. Ozaki, Gunawan, et al., "Effect of Indium Doping on Surface Optoelectrical Properties of $Cu_2ZnSnS_4$ Photoabsorber and Interfacial/Photovoltaic Performance of Cadmium Free $In_2S_3/Cu_2ZnSnS_4$ Heterojunction Thin Film Solar Cell," *Chemistry of Materials* 28 (2016): 3283–3291, https://doi.org/10.1021/acs.chemmater.5b04984.

96. A. Way, J. Luke, A. D. Evans, et al., "Fluorine Doped Tin Oxide as an Alternative of Indium Tin Oxide for Bottom Electrode of Semi-Transparent Organic Photovoltaic Devices," *AIP Advances* 9, no. 8 (2019): 085220, https://doi.org/10.1063/1.5104333.

97. J. S. Kim, J. K. Kang, and D. K. Hwang, "High Efficiency Bifacial $Cu_2ZnSnSe_4$ Thin-Film Solar Cells on Transparent Conducting Oxide Glass Substrates," *APL Materials* 4, no. 9 (2016): 096101, https://doi.org/10.1063/1.4962145.

98. L. Sravani, S. Routray, K. P. Pradhan, and M. C. Piedrahita, "Kesterite Thin-Film Solar Cell: Role of Grain Boundaries and Defects in Copper–Zinc–Tin–Sulfide and Copper–Zinc–Tin–Selenide," *Physica Status Solidi (a)* 218, no. 16 (2021): 2100039, https://doi.org/10.1002/pssa.202100039.

99. J. Li, J. Huang, F. Ma, et al., "Unveiling Microscopic Carrier Loss Mechanisms in 12% Efficient $Cu_2ZnSnSe_4$ Solar Cells," *Nature Energy* 7, no. 8 (2022): 754–764, https://doi.org/10.1038/s41560-022-01078-7.

100. B. Liu, J. Guo, R. Hao, et al., "Effect of Na Doping on the Performance and the Band Alignment of CZTS/CdS Thin Film Solar Cell," *Solar Energy* 201 (2020): 219–226, https://doi.org/10.1016/j.solener.2020.02.088.

101. H. B. Sawa, M. Babucci, O. Donzel-Gargand, et al., "Enhanced Performance of $Cu_2ZnSnS_4$ Based Bifacial Solar Cells with FTO and W/FTO Back Contacts through Absorber Air Annealing and Na Incorporation," *Solar Energy Materials and Solar Cells* 264 (2024): 112605, https://doi.org/10.1016/j.solmat.2023.112605.

102. F. Chen, B. Liu, W. Shao, et al., "Solution-Deposited $MoO_3$ Interface Layer for High-Performance Bifacial Kesterite Thin Film Solar Cell," *ACS Applied Energy Materials* 7, no. 9 (2024): 4050–4056, https://doi.org/10.1021/acsaem.4C00346.

103. D. Ma, M. Li, B. Yao, et al., "A High Effciency (11.06%) CZTSSe Solar Cell Achieved by Combining Ag Doping in Absorber and BxCd1-Xs/Caztsse Heterojunction Annealing," *Solar Energy Materials and Solar Cells* 276 (2024): 113037, https://doi.org/10.1016/j.solmat.2024.113037.

104. W. Wang, M. T. Winkler, O. Gunawan, et al., "Device Characteristics of CZTSSe Thin-Film Solar Cells with 12.6% Efficiency," *Advanced Energy Materials* 4, no. 7 (2014): 1301465, https://doi.org/10.1002/aenm.201301465.

105. Y. Jian, T. Xie, L. Han, et al., "Modification of back interfacial contact with $MoO_3$ layer *in situ* introduced by $Na_2S$ aqueous solution for efficient kesterite CZTSSe solar cells," *Journal of Materials Chemistry C* 11, no. 14 (2023): 4634–4644, https://doi.org/10.1039/d3tc00378g.

106. I. Bouchama and S. Ali-Saoucha, "Effect of Wide Band-Gap TCO Properties on the Bifacial CZTS Thin-Films Solar Cells Performances," *Optik (Stuttg)* 144 (2017): 370–377, https://doi.org/10.1016/j.ijleo.2017.07.009.

107. H. Deng, Q. Sun, Z. Yang, et al., "Novel Symmetrical Bifacial Flexible CZTSSe Thin Film Solar Cells for Indoor Photovoltaic Applications," *Nature Communications* 12, no. 1 (2021): 1–8, https://doi.org/10.1038/s41467-021-23343.

108. J. Liu, H. Cai, X. Wu, et al., "Interface-Suppressed High-Quality Symmetrical Bifacial Flexible CZTSe Solar Cells through a Green Electrodeposition Process," *Journal of Materials Chemistry A* 11, no. 39 (2023): 21293–21299, https://doi.org/10.1039/d3ta03411a.

109. S.-Y. Kuo, J.-F. Yang, K.-J. Lin, F.-I. Lai, and J. Shi, "Improved $Cu_2ZnSnS_4$ Solar Cell Performance by Multimetallic Stacked Nanolayers," *International Journal of Energy Research* 2024, no. 1 (2024): 2364224, https://doi.org/10.1155/2024/2364224.

110. D. Ma, B. Yao, Y. Li, et al., "Improvement of Power Conversion Efficiency of $Cu_2ZnSn(S,Se)_4$ Solar Cells by Al Doped CdS," *Physica B: Condensed Matter* 643 (2022): 414083, https://doi.org/10.1016/j.physb.2022.414083.

111. S. Tao, L. Dong, J. Han, et al., "Efficiency enhancement of CZTSe solar cells based on *in situ* K-doped precursor," *Journal of Materials Chemistry A* 11, no. 16 (2023): 9085–9096, https://doi.org/10.1039/d2ta09916k.

112. Y. E. Romanyuk, S. G. Haass, S. Giraldo, et al., "Doping and Alloying of Kesterites," *Journal of Physics: Energy* 1, no. 4 (2019): 044004, https://doi.org/10.1088/2515-7655/ab23bc.

113. Y. Wang, S. Ji, and B. Shin, "Interface Engineering of Antimony Selenide Solar Cells: A Review on the Optimization of Energy Band Alignments," *Journal of Physics: Energy* 4, no. 4 (2022): 044002, https://doi.org/10.1088/2515-7655/ac8578.

114. A. Mo, B. Yang, X. Lu, et al., "Reducing Parasitic Loss and Deep Defect Formation via Copper Doping Toward Highly Efficient $Sb_2Se_3$ Solar Cells," *Advanced Functional Materials* 35, no. 20 (2025): 2420261, https://doi.org/10.1002/adfm.202420261.

115. Z. Duan, X. Liang, Y. Feng, et al., "$Sb_2Se_3$ Thin-Film Solar Cells Exceeding 10% Power Conversion Efficiency Enabled by Injection Vapor Deposition Technology," *Advanced Materials* 34, no. 30 (2022): 2202969, https://doi.org/10.1002/adma.202202969.

116. A. Polman, M. Knight, E. C. Garnett, B. Ehrler, and W. C. Sinke, "Photovoltaic Materials: Present Efficiencies and Future Challenges," *Science* 352 (2016): aad4424, https://doi.org/10.1126/science.aad4424.

117. Y. Zhao, S. Wang, C. Li, et al., "Regulating deposition kinetics *via* a novel additive-assisted chemical bath deposition technology enables fabrication of 10.57%-efficiency $Sb_2Se_3$ solar cells," *Energy & Environmental Science* 15, no. 12 (2022): 5118–5128, https://doi.org/10.1039/d2ee02261c.

118. S. Wang, Y. Zhao, B. Che, et al., "A Novel Multi-Sulfur Source Collaborative Chemical Bath Deposition Technology Enables 8%-Efficiency $Sb_2S_3$ Planar Solar Cells," *Advanced Materials* 34, no. 41 (2022): 2206242, https://doi.org/10.1002/adma.202206242.

119. L. Zhu, R. Liu, Z. Wan, et al., "Parallel Planar Heterojunction Strategy Enables $Sb_2S_3$ Solar Cells with Efficiency Exceeding 8%," *Angewandte Chemie International Edition* 62, no. 50 (2023): e202312951, https://doi.org/10.1002/anie.202312951.

120. X. Chen, B. Che, Y. Zhao, et al., "Solvent-Assisted Hydrothermal Deposition Approach for Highly-Efficient $Sb_2(S,Se)_3$ Thin-Film Solar Cells," *Advanced Energy Materials* 13, no. 21 (2023): 2300391, https://doi.org/10.1002/aenm.202300391.

121. J. Dong, Y. Liu, Z. Wang, and Y. Zhang, "Boosting $V_{OC}$ of antimony chalcogenide solar cells: A review on interfaces and defects," *Nano Select* 2, no. 10 (2021): 1818–1848, https://doi.org/10.1002/nano.202000288.

122. Y. Liu, S. Xu, Y. Luo, et al., "A Review on Suppressing Nonradiative Recombination Losses in Antimony Chalcogenide Thin-Film Solar Cell," *Solar RRL* 8, no. 19 (2024): 2400499, https://doi.org/10.1002/solr.202400499.

123. S. Lee and M. F. McInerney, "Optimization of Bifacial Ge-Incorporated $Sb_2Se_3$ Thin-Film Solar Cells by Modeling $Cu_2O$ Back Buffer Layer," *Solar Energy Materials and Solar Cells* 257 (2023): 112399, https://doi.org/10.1016/j.solmat.2023.112399.

124. F. Pattini, S. Rampino, F. Mezzadri, et al., "Role of the Substrates in the Ribbon Orientation of $Sb_2Se_3$ Films Grown by Low-Temperature Pulsed Electron Deposition," *Solar Energy Materials and Solar Cells* 218 (2020): 110724, https://doi.org/10.1016/j.solmat.2020.110724.

125. H. Zhou, M. Feng, P. Li, X. Gong, D. Zhang, and S. Chen, "Fabrication of a preferentially [001]-oriented $Sb_2Se_3$ thin film on diverse substrates and its application in photoelectrochemical water reduction," *Sustainable Energy & Fuels* 4, no. 8 (2020): 3943–3950, https://doi.org/10.1039/d0se00646g.

126. K. Li, J. Yang, Z. Cai, et al., "Effect of Energy-Driven Molecular Precursor Decomposition on the Crystal Orientation of Antimony Selenide Film and Solar Cell Efficiency," *Small Methods* 8, no. 12 (2024): 2400227, https://doi.org/10.1002/smtd.202400227.

127. J. Liu, Z. Chen, C. Wu, et al., "Recent Advances in Antimony Selenide Photodetectors," *Advanced Materials* 36, no. 41 (2024): 2406028, https://doi.org/10.1002/adma.202406028.

128. H. Deng, Y. Zeng, M. Ishaq, et al., "Quasiepitaxy Strategy for Efficient Full-Inorganic $Sb_2S_3$ Solar Cells," *Advanced Functional Materials* 29, no. 31 (2019): 1901720, https://doi.org/10.1002/adfm.201901720.

129. N. Daem, M.-J. Charlier, G. Spronck, P. Colson, R. Cloots, and J. Dewalque, "Spin-coating processing of an oriented $Sb_2S_3$ layer for PV applications: effect of the precursors and device architecture," *EES Solar* 1, no. 2 (2025): 193–208, https://doi.org/10.1039/d4el00036f.

130. J. Otavio Mendes, A. Merenda, K. Wilson, A. Fraser Lee, E. Della Gaspera, and J. van Embden, "Substrate Morphology Directs (001) $Sb_2Se_3$ Thin Film Growth by Crystallographic Orientation Filtering," *Small* 20, no. 39 (2024): 2302721, https://doi.org/10.1002/smll.202302721.

131. Y. Zhou, L. Wang, S. Chen, et al., "Thin-Film $Sb_2Se_3$ Photovoltaics with Oriented One-Dimensional Ribbons and Benign Grain Boundaries," *Nature Photonics* 9, no. 6 (2015): 409–415, https://doi.org/10.1038/nphoton.2015.78.

132. J. Zhou, H. Chen, X. Zhang, et al., "Substrate Dependence on $(Sb_4Se_6)n$ Ribbon Orientations of Antimony Selenide Thin Films: Morphology, Carrier Transport and Photovoltaic Performance," *Journal of Alloys and Compounds* 862 (2021): 158703, https://doi.org/10.1016/j.jallcom.2021.158703.

133. L. Guo, B. Zhang, Y. Qin, et al., "Tunable Quasi-One-Dimensional Ribbon Enhanced Light Absorption in $Sb_2Se_3$ Thin-Film Solar Cells Grown by Close-Space Sublimation," *Solar RRL* 2, no. 10 (2018): 1800128, https://doi.org/10.1002/solr.201800128.

134. C. C. Cheng and Y. C. Lin, "Optimization of $NiO_x$ Thin Film Properties and Its Impact on the Performance of Bifacial $Sb_2Se_3$ Solar

Cells," *Solar Energy Materials and Solar Cells* 285 (2025): 113511, https://doi.org/10.1016/j.solmat.2025.113511.

135. C. Qian, K. Sun, J. Cong, et al., "Bifacial and Semitransparent $Sb_2(S, Se)_3$ Solar Cells for Single-Junction and Tandem Photovoltaic Applications," *Advanced Materials* 35, no. 42 (2023): 2303936, https://doi.org/10.1002/adma.202303936.